

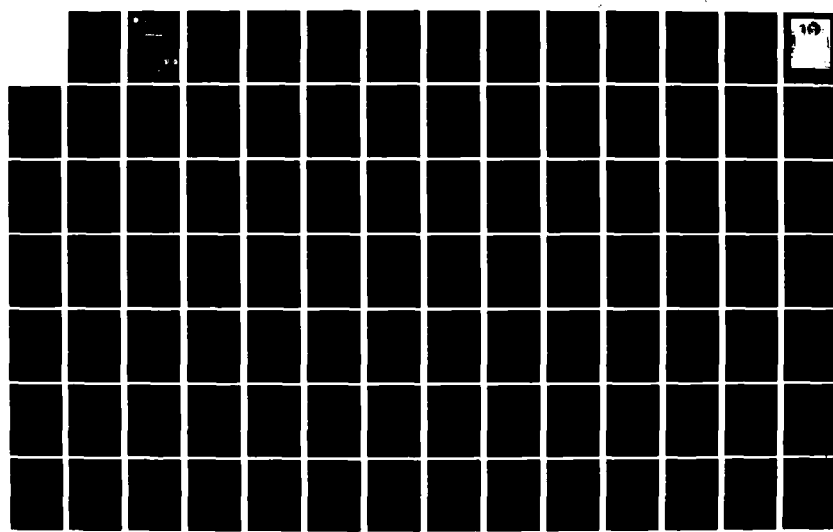
AD-A121 374      BASIC RESEARCH IN THREE-DIMENSIONAL IMAGING FROM  
TRANSIENT RADAR SCATTERI. (U) OHIO STATE UNIV COLUMBUS  
ELECTROSCIENCE LAB J D YOUNG ET AL JUL 78

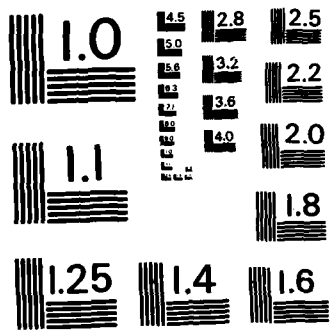
172

UNCLASSIFIED

ESL-784785-1 DASG60-77-C-0133

F/G 17/9 NL





MICROCOPY RESOLUTION TEST CHART  
NATIONAL BUREAU OF STANDARDS-1963-A

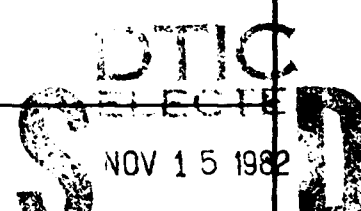
AD A121374

## NOTICES

When Government drawings, specifications, or other data are used for any purpose other than in connection with a definitely related Government procurement operation, the United States Government thereby incurs no responsibility nor any obligation whatsoever, and the fact that the Government may have formulated, furnished, or in any way supplied the said drawings, specifications, or other data, is not to be regarded by implication or otherwise as in any manner licensing the holder or any other person or corporation, or conveying any rights or permission to manufacture, use, or sell any patented invention that may in any way be related thereto.

## UNCLASSIFIED

SECURITY CLASSIFICATION OF THIS PAGE (When Data Entered)

REPORT DOCUMENTATION PAGE		READ INSTRUCTIONS BEFORE COMPLETING FORM
1. REPORT NUMBER	2. GOVT ACCESSION NO.	3. RECIPIENT'S CATALOG NUMBER
	AD-A121374	
4. TITLE (and Subtitle)  BASIC RESEARCH IN THREE-DIMENSIONAL IMAGING FROM TRANSIENT RADAR SCATTERING SIGNATURES		5. TYPE OF REPORT & PERIOD COVERED  Annual Status Report
		6. PERFORMING ORG. REPORT NUMBER  ESL 784785-1
7. AUTHOR(s)  J. D. Young                    F. B. Gross R. A. Day                    E. K. Walton		8. CONTRACT OR GRANT NUMBER(s)  Contract DASG60-77-C-0133
9. PERFORMING ORGANIZATION NAME AND ADDRESS  The Ohio State University ElectroScience Laboratory, Department of Electrical Engineering Columbus, Ohio, 43212		10. PROGRAM ELEMENT, PROJECT, TASK AREA & WORK UNIT NUMBERS  6.33.04.A.
11. CONTROLLING OFFICE NAME AND ADDRESS  Ballistic Missile Defense Systems Command Contracts Office BMDS-CRS, P.O. Box 1500, Code W31RPD, Huntsville, Alabama 35807		12. REPORT DATE  July 1978
		13. NUMBER OF PAGES  123
14. MONITORING AGENCY NAME & ADDRESS (if different from Controlling Office)		15. SECURITY CLASS. (of this report)  Unclassified
		15a. DECLASSIFICATION/DOWNGRADING SCHEDULE
16. DISTRIBUTION STATEMENT (of this Report)  <div style="border: 1px solid black; padding: 5px; text-align: center;">This document has been approved for public release and sale; its distribution is unlimited.</div>		
17. DISTRIBUTION STATEMENT (of the abstract entered in Block 20, if different from Report)		
18. SUPPLEMENTARY NOTES   NOV 15 1982 A		
19. KEY WORDS (Continue on reverse side if necessary and identify by block number)  Radar                          Image Transient                      Time Domain Scattering Cone		
20. ABSTRACT (Continue on reverse side if necessary and identify by block number)  Accomplishments during the first year of an effort concerned with imaging of cone-like targets from measured and calculated data are described. The low frequency portion of the required transient response data were measured and calculated. Approximate time domain ramp response signature waveforms were generated and their relation to target geometry examined. Three-dimensional images were generated for all targets using available data. Investigation was initiated on several aspects of imaging procedures: 1) automated iterative limiting surface imaging, 2) image con-		

**UNCLASSIFIED**

**SECURITY CLASSIFICATION OF THIS PAGE(When Data Entered)**

20.

fidence vs. target characteristics and the extent of known scattering data,  
3) ideal relationships between geometry and scattering signature features  
based on physical optics inverse scattering theory, and 4) effects on image  
quality of limited data in frequency and aspect angle.



**UNCLASSIFIED**

**SECURITY CLASSIFICATION OF THIS PAGE(When Data Entered)**

## TABLE OF CONTENTS

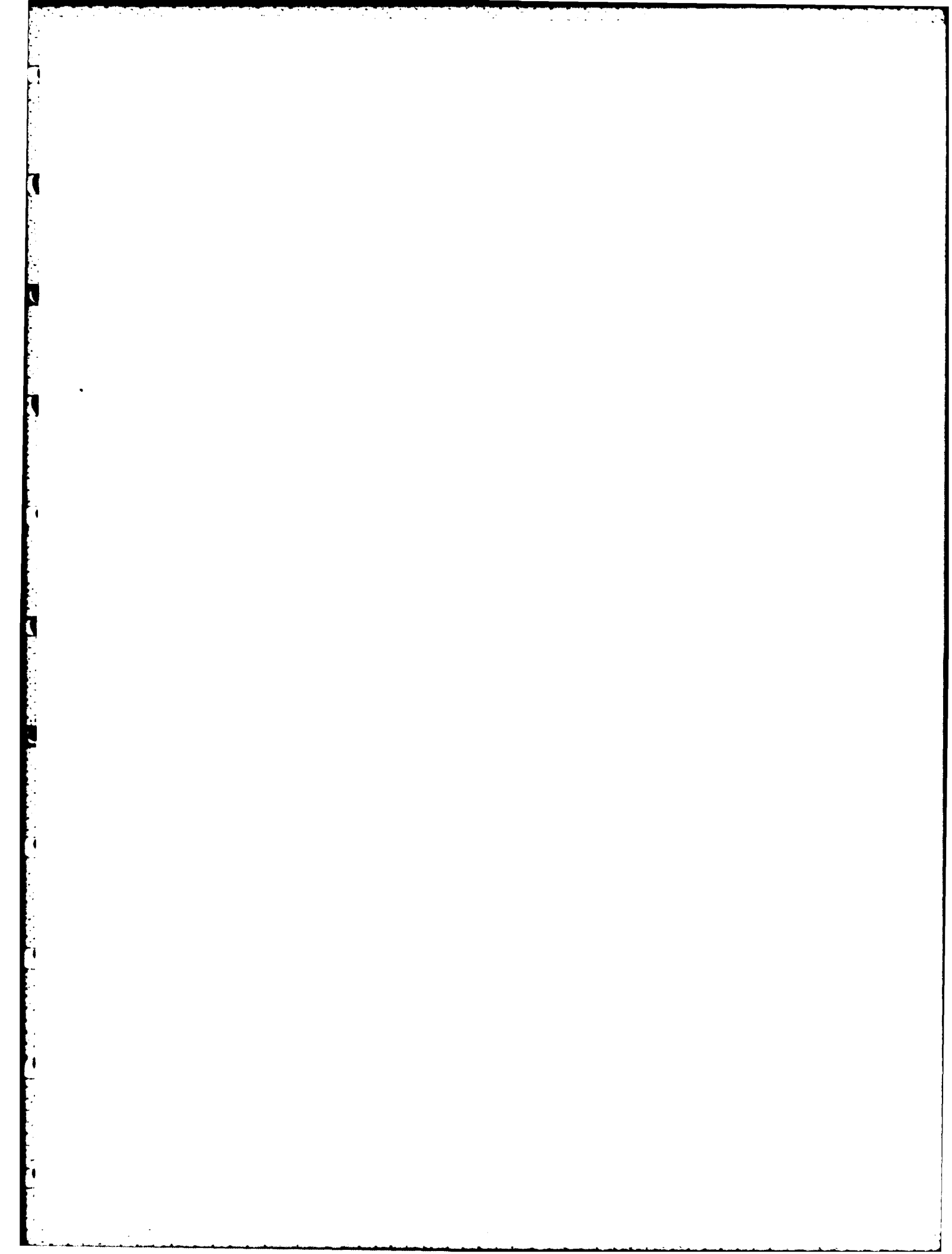
	Page
I      INTRODUCTION	1
II     TRANSIENT RESPONSE OF CONE-LIKE OBJECTS	3
A. Preliminary	3
B. Original System Checkout	3
C. Data Collection Program	7
D. Large Target Measurements	22
E. Theoretical Studies	23
III    RAMP RESPONSES AND LIMITING SURFACE IMAGES	33
A. The Ramp Response Waveform	33
B. Ramp Response Processing	34
C. Ramp Responses for Cone-like Targets	34
D. Description of Limiting Surface Imaging Process	40
E. Limiting Surface Parameters for Conical Shapes	45
F. Imaging Dependence on Limiting Surface Parameters	48
G. A Possible Approach for the Study of Image Confidence	55
IV    HIGH FREQUENCY IMAGING USING THE BOJARSKI IDENTITY	59
A. Introduction	59
B. The Bojarski Identity	60
C. Trial Results	60
D. One Dimension	61
E. Two Dimensions	61
F. Conclusion	98
V    SUMMARY AND CONCLUSIONS	98
REFERENCES	102
Appendix A TABULATIONS OF AMPLITUDE AND PHASE DATA	104
Appendix B RAMP RESPONSE WAVEFORMS FOR TARGET SET	111



Accession For  
NTIS GRAAL  
FILE TAB  
SEARCHED

*EL-88*

*A*



## I. INTRODUCTION

This report summarizes progress during the first twelve months of an eighteen month study concerning imaging from transient radar signatures as applied to cone-like targets. A partial data set has been acquired for a group of specific shapes, images have been generated using the data, and the characteristics of the imaging process itself for two separate approaches have been investigated.

This research is an outgrowth of past studies of the transient signatures of radar targets in general, and of methods of target recognition using transient signatures [1]. Past efforts had already established several facts:

Simple relationships exist between the transient radar signature and the geometrical properties. For imaging, the primary relationship used is the profile function (or target transverse cross-sectional area vs line of sight distance) information which is contained in the ramp response signature. More recent imaging research is also making use of target resonance properties, derived from the decaying portion of the transient response, and measured as a function of incident E-field polarization, in order to obtain additional orientation and shape information [2]. Finally, other transient response-derived target resonant properties are proving useful in studies of automated target discrimination [3].

The primary problem in applying this process to free-space objects with current radar technology is the required frequency spectrum of the interrogating radar signal. The present specification is for a signal covering a 10:1 frequency band, whose wavelengths range from approximately four times to 0.4 times the target maximum dimension. Thus, for practical targets this process would presently require construction of an ultra-broadband HF or VHF radar system to acquire the signatures. This is the principle problem to be attacked in the proposed research.

Applying these same techniques to arrive at target identification processes on cone-like targets using other sources of target scattering information is the fundamental goal of this research.

Two broad classes of target scattering information are being considered.

1. Normal radar systems, with interrogating frequencies from 500 MHz to X band

In any radar identification system, it is known that the signature features on which the discrimination process is based are crucial to the speed and error performance of this system. It is postulated that transient response analysis and target imaging analysis which makes use of the high frequencies in addition to the low frequency data used previously will lead to added insight into future selection for rapid, accurate discrimination using high frequencies only.

## 2. High-power laser radar (LADAR)

A companion research effort at this Laboratory is studying non-linear effects in ordinary materials under intense laser radiation. This effect could be used to "down-convert" a transient-modulated laser signal to produce the equivalent of the radar transient response [4]. The relationship of this laser-produced transient response to the radar impulse response, and consequent imaging and target identification implications, will be studied during the last six months of the contract.

Transient response information is fundamental to all of this effort. Section II discusses a specific set of target shapes which were chosen for study, and the experimental and analytical work involved in obtaining the radar scattering data. This effort is concentrating on the backscattered radar cross-section at interrogating directions within 30° of nose-on incidence. The systems being used for data measurement are described, and analytic techniques used in the calculations are briefly discussed. The characteristics of the data obtained thus far are discussed, and an estimate of the accuracy is presented. Some of the data are also compared to other measurements.

In Section III, the time-domain ramp responses obtained from the data are discussed, and the application of the limiting-surface imaging process to the data is treated. The imaging process itself is currently being examined with a purpose of increased automation. The current state of this effort is also presented.

In Section IV, our research on inverse scattering concepts is discussed. The Bojarski-Lewis transform is reviewed. It is shown that studies of target identification with limited angular and frequency information are equivalent to analysis of windowing using the Bojarski-Lewis transform. An extensive set of results are presented to illustrate the effects of windowing on some simple two dimensional shapes.

Section V contains a summary of all effort on this contract to date, and a discussion of work to be done during the remainder of the contract period. Also presented are some possible practical applications of the research.

Complete frequency domain data and time domain waveforms obtained to date are included in Appendices A and B.

## II. TRANSIENT RESPONSE OF CONE-LIKE OBJECTS

### A. Preliminary

This part of the project involved the collection and analysis of data to be used in the imaging of the six cone-like targets shown in Figure 1. The project was divided into two main tasks. The first task was the collection of data on 5 cm long models of the six targets using the Ten Harmonic Radar system. This system measures both the phase and amplitude of the backscatter from the set of targets over a frequency ranging from 1.1 GHz to 11.0 GHz in ten harmonically related steps. With the five centimeter long cone-like targets, this frequency range included data from the Rayleigh region up to the resonance region of all of the targets.

The second part of the project was a theoretical study of the radar backscattering for the cone-like targets. The results of the theoretical study allowed the experimental data to be critically evaluated. The radar cross section has been determined for each target at each of the harmonically related frequencies and for each aspect angle and polarization. In most cases, both experimental and theoretical results are available. In some cases, however, the experimental or the theoretical results are unreliable and only one of the two methods can be used.

### B. Original System Checkout

A block diagram of the experimental ten-harmonic radar backscatter system [5,6] is shown in Figure 2. In this system a single L-band microwave source is used to harmonically generate a set of frequencies. The HP network analyzer receiver local oscillator is used to modulate the higher harmonics (balanced modulators), and also to modulate (lower sideband) the L band signal going into the reference port of the HP network analyzer receiver head. The result is that the receiver head of the HP network analyzer downconverts each of the harmonically related backscattered signals to the same IF frequency. The output of the HP network analyzer is in fact, the vector sum of the set of signals being received. (In actual practice, the transmitter does not transmit all 10 harmonics simultaneously. Limitations in the transmitter output multiplexer require that the signals be transmitted in bands of 4 or 5 frequencies at a time.) A photograph of the bistatic antennas in the anechoic chamber with an enlarged (for the photograph) sphere target on the foam pedestal is shown in Figure 3.

The processing of the data from this point reduces the contribution of the background and antenna coupling in the received signal and recovers the individual amplitude and phase of the individual harmonics. The operational procedure is to move the target slowly toward the radar antennas and to take amplitude and phase data samples under computer control.

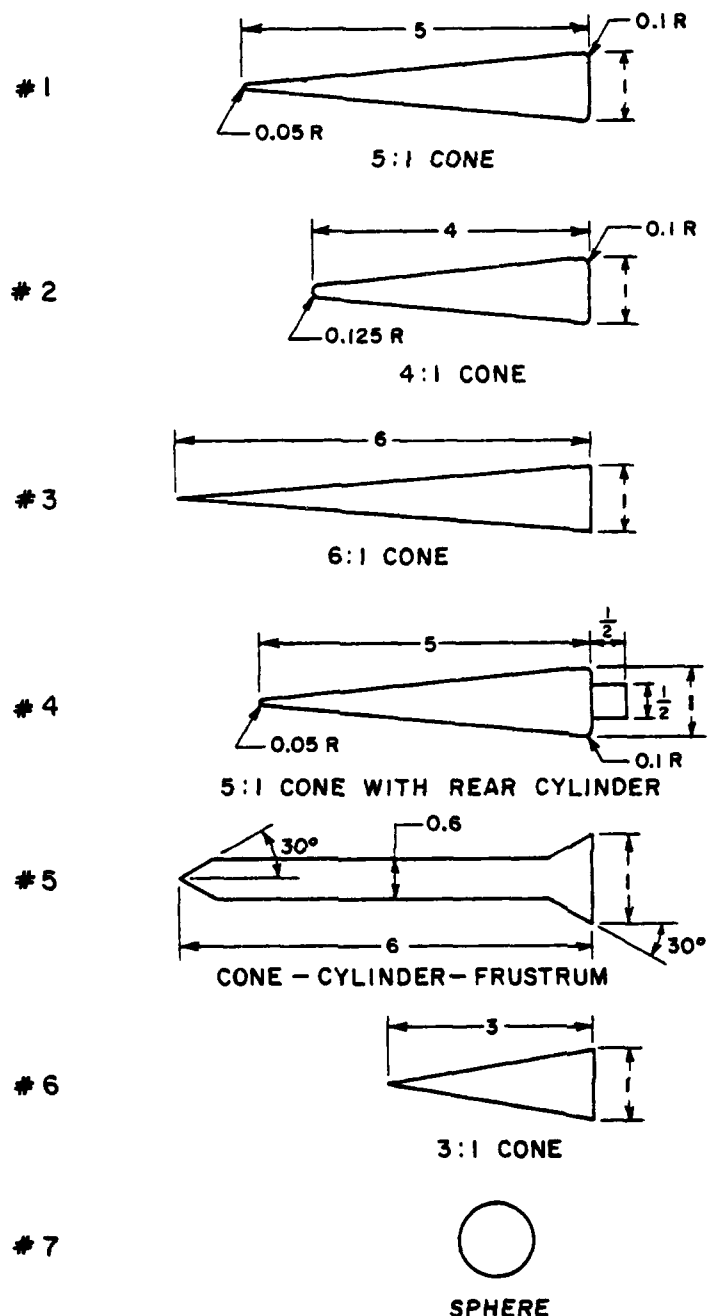
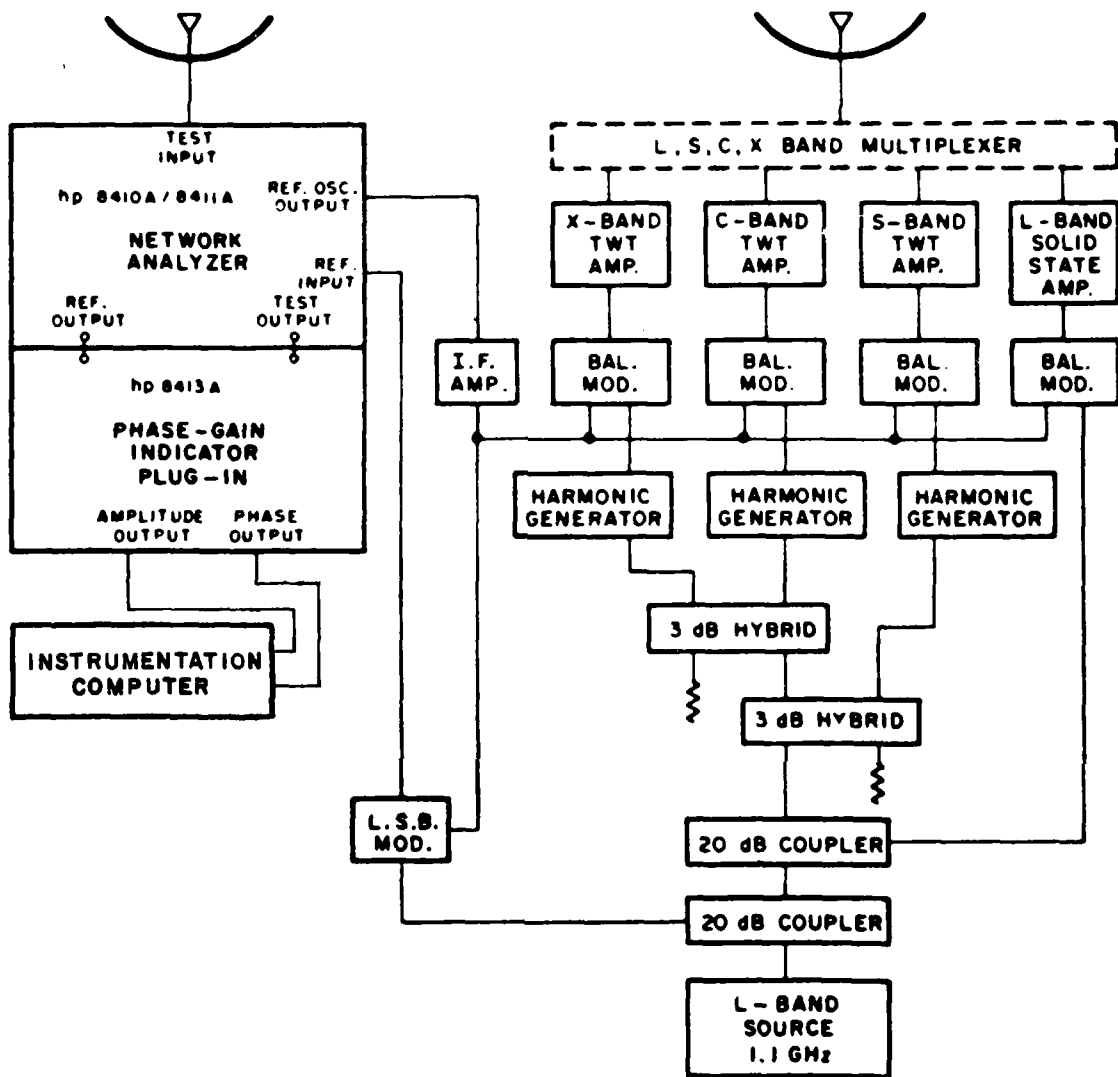


Figure 1. Outlines of targets used in this study.



## TRANSMITTER / RECEIVER

Figure 2. Block diagram of the ten harmonic radar system.



Figure 3. Photograph of antenna orientation and the target support.

Arrays of amplitude and phase versus position data for the targets of interest as well as the empty support pedestal and a calibration and test sphere are stored in the computer. The raw data are Fourier transformed to yield the amplitude and phase of the individual harmonics. Any antenna coupling or scattering from stationary objects is rejected at this point as a DC term. The target measurements then have the empty pedestal (background) data subtracted and the final result is calibrated by using the calibration sphere data. In the end, we have the amplitude of the targets expressed as absolute radar cross section (in cm.) and the phase of the backscattered return relative to the center of the calibration sphere. The check sphere data serves as an estimate of the overall accuracy of the system.

In the initial stages of this project, a number of preliminary system checks and calibration tests were performed. It was necessary to confirm overall system linearity so that the Fourier techniques would not generate spurious results. It was also necessary to confirm the accuracy of the target positioning system so that the subtractions of the empty pedestal (background) data would be valid. The sensitivity and signal to noise behavior of the network analyzer also needed to be examined. Any degradation of the data at the low end of the dynamic range of the target and background measurements would clearly cause severe errors in the results. The ten harmonic range was finally considered to be functional, and a study of the overall system accuracy was undertaken, using the data on the check sphere target. Some of the results are shown in Figure 4. In this figure, the amplitude and phase of the individual cross-sections for each harmonically related frequency are plotted using a polar format. As can be seen, the system produces data with accuracies on the order of 10%. (In this case, accuracy is defined as the magnitude of the error phasor divided by the magnitude of the known theoretical phasor.) As will be shown in the time domain section, this accuracy is sufficient for time domain analysis and imaging of the targets.

### C. Data Collection Program

Once the system was operating with confidence the collection of the experimental data was begun. As was mentioned in the previous section of this report, the actual data collection was carried out in several steps. The sequence of data collection steps is outlined below.

- (1) Configure radar system for a particular harmonic group, (i.e., 1;2 through 5;6 through 10).
- (2) Move the object 1/2 wavelength (first harmonic). Position versus amplitude and phase (256 samples) are loaded into a computer file. ("Object" in this case may be the empty pedestal (background), the calibrate sphere, the reference sphere, or the cone target of interest.)
- (3) Perform step 2 for the background, the spheres, and the cone target at aspect angles of 0,10,20, and 30 degrees.

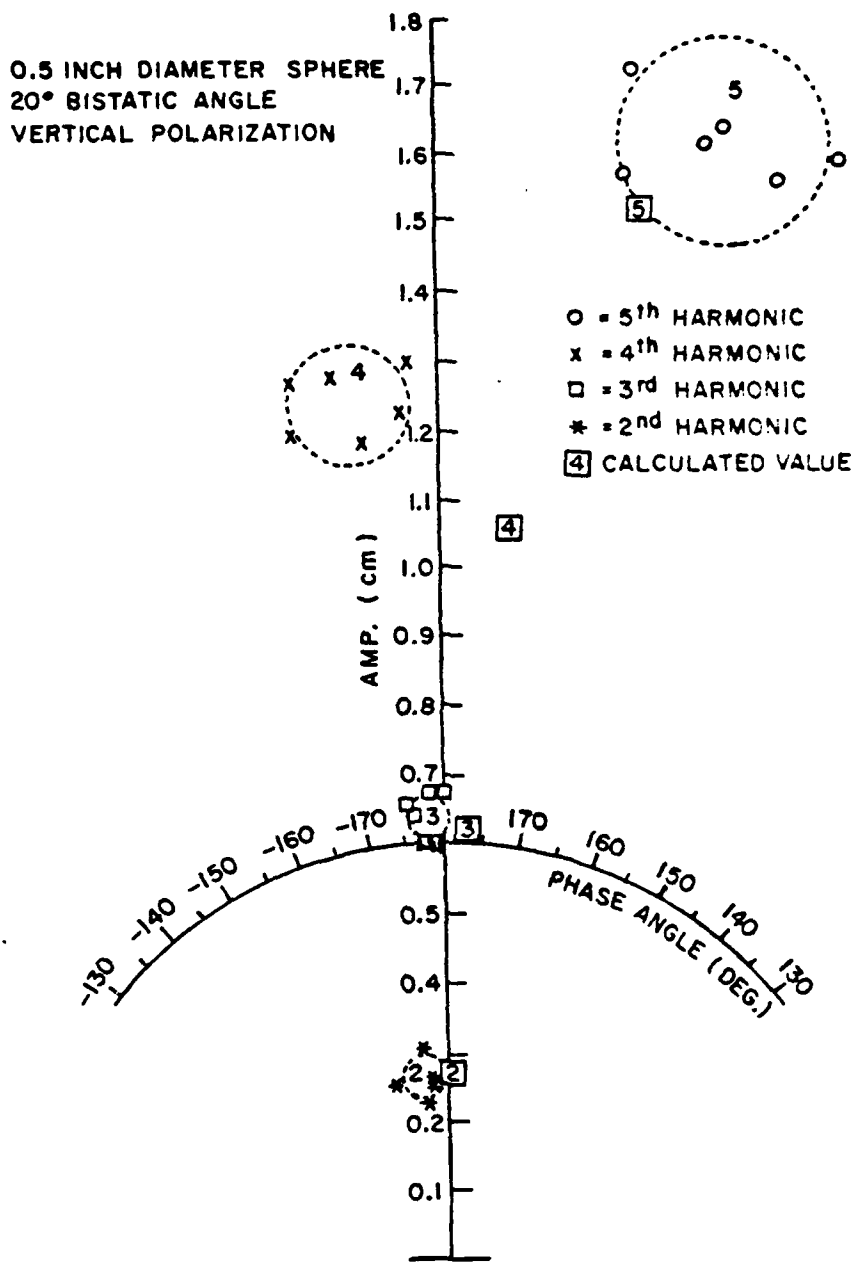


Figure 4. Polar diagram of error distribution of the data for the small sphere target.

- (4) Use Fourier transform techniques to transform the position versus amplitude and phase computer files into harmonic number (frequency) versus amplitude and phase computer files.
- (5) Subtract the background data from the sphere and target data (phasor calculation).
- (6) Use computed values of amplitude and phase from the reference sphere for the computation of absolute radar cross section of the check sphere and the cone target.
- (7) If the computed values of the cross section of the check sphere are within tolerance of the measured values, the cone target data are accepted as valid and the absolute radar cross section of the target cone (amplitude and phase) is stored into computer files.
- (8) Once all targets have been measured in this way, a new harmonic group is chosen and we proceed to step one until data for all harmonics have been measured.

The final result of these measurements is a set of computer files giving the absolute radar cross section amplitude and phase versus harmonic number (frequency) for each of the targets (including the check spheres) at each aspect angle. These results are tabulated in Appendix A of this report. Plots of part of these data are given in Figures 5-10.

The data shown in Figures 5-10 all exhibit certain similar properties. In each figure, for example, the transition from the resonance region to the Rayleigh region can be observed as a transition from an oscillating behavior (as a function of frequency) to a rapid reduction of amplitude and a phase which approaches 180 degrees. The higher frequency values of radar cross section amplitude of 1 to 3 cm ( $1$  to  $1.7 \text{ cm}^2$ ) corresponds approximately to the area of the base of the cone. It seems that the length of the cone is not an important determining factor of the radar cross section of a cone target when the aspect angle is small. We can also note that the vertical polarization data is more well behaved than the horizontal polarization data. Polarization sense is defined in this case with reference to the plane containing the lines from the bistatic antennas to the target. The behavior of the horizontal polarization is partly caused by the cone targets themselves and partly caused by the increased signal to noise problems encountered in the horizontally polarized bistatic radar antenna configuration.

A final remark in this section concerns the accuracy of the overall data. As can be seen from the figures, the spread of the data is sometimes quite large for the various aspect angles, or from harmonic number to harmonic number. These large variations are due in large part to the system errors. It is possible for the cone targets to have a small radar cross section at the same time that the check targets have larger cross

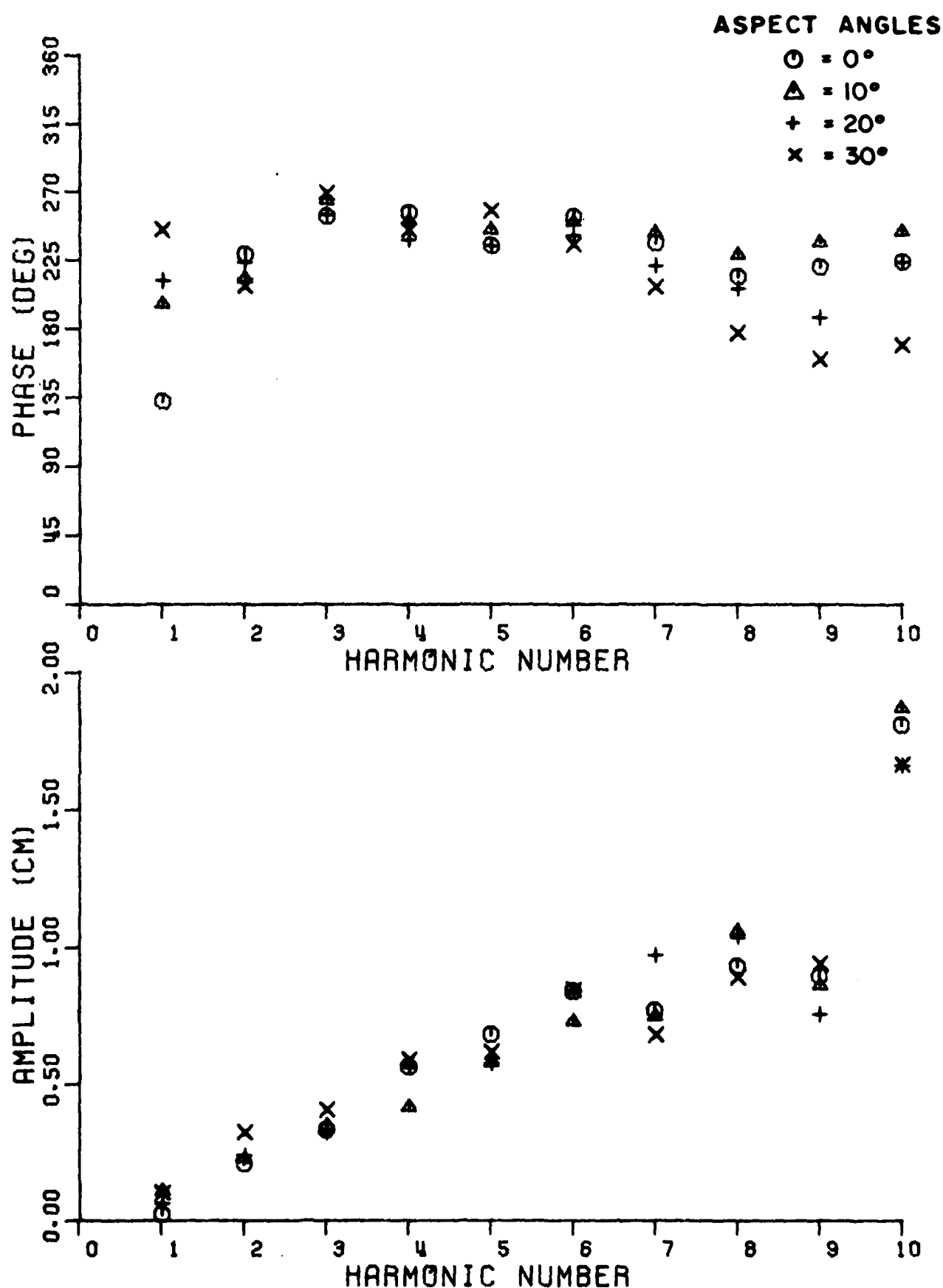


Figure 5a. Amplitude and phase data on cone #1 as a function of frequency. (vertical polarization)

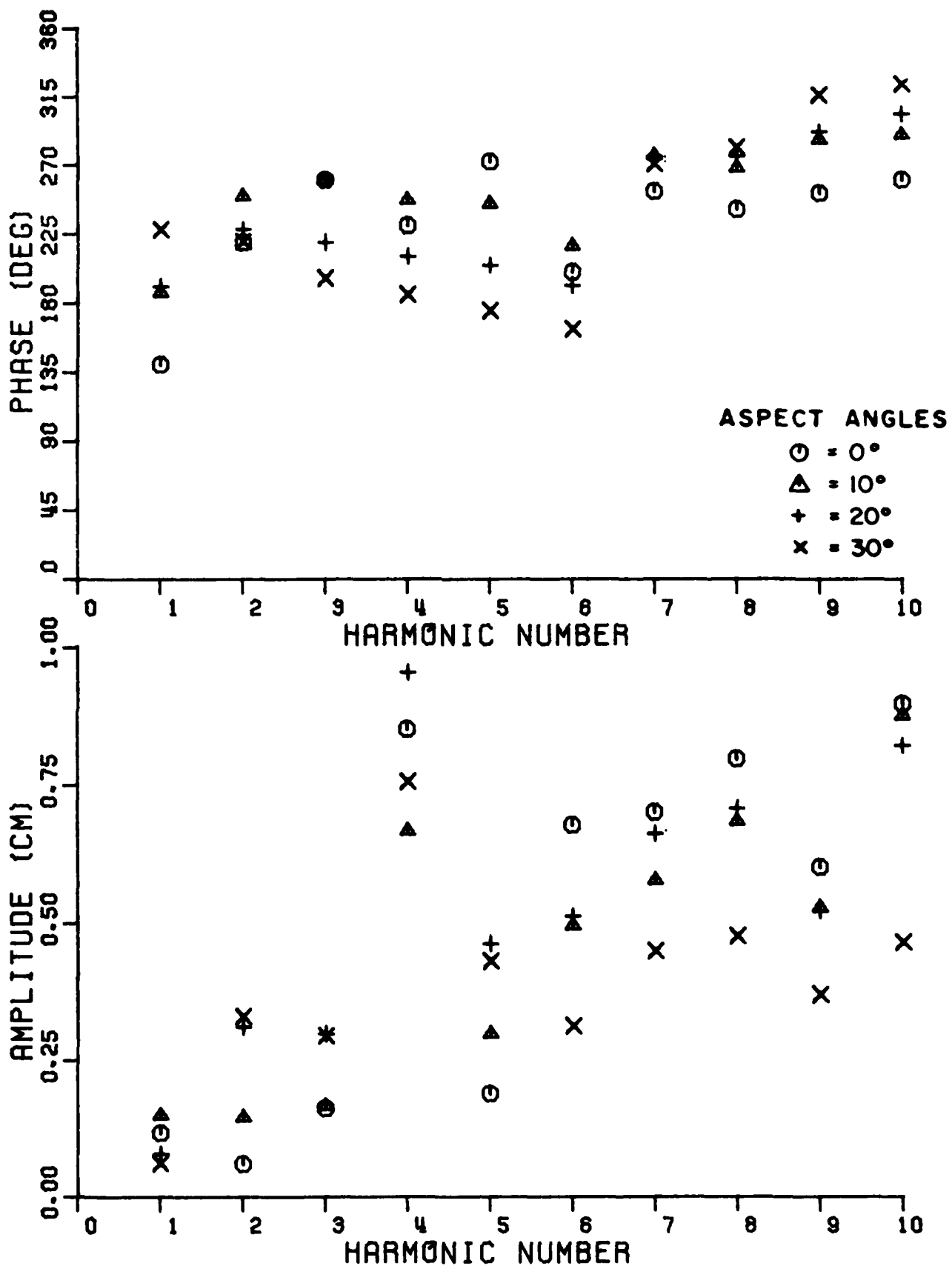


Figure 5b. Amplitude and phase data on cone #1 as a function of frequency. (horizontal polarization)

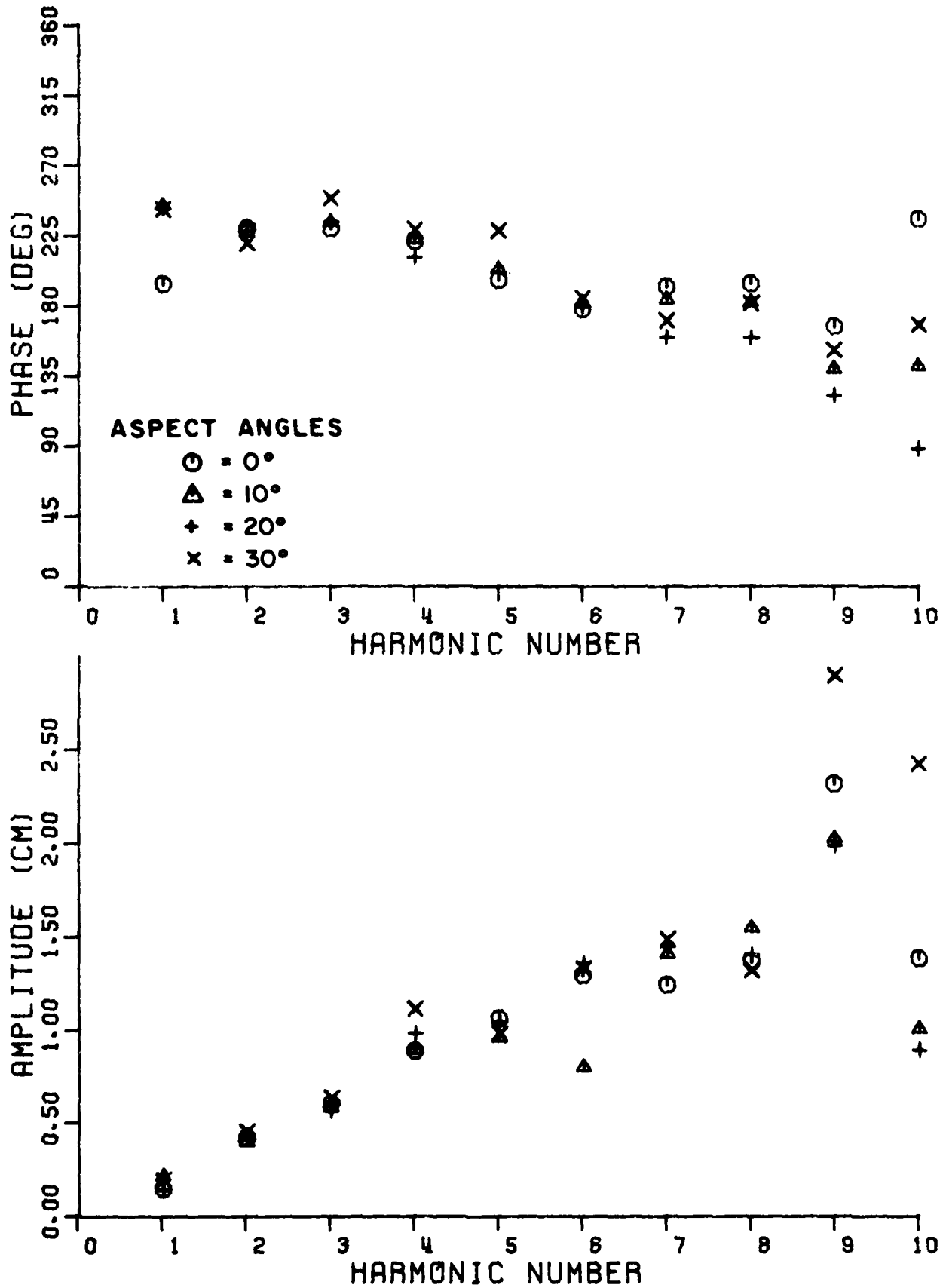


Figure 6a. Amplitude and phase data on cone #2 as a function of frequency. (vertical polarization)

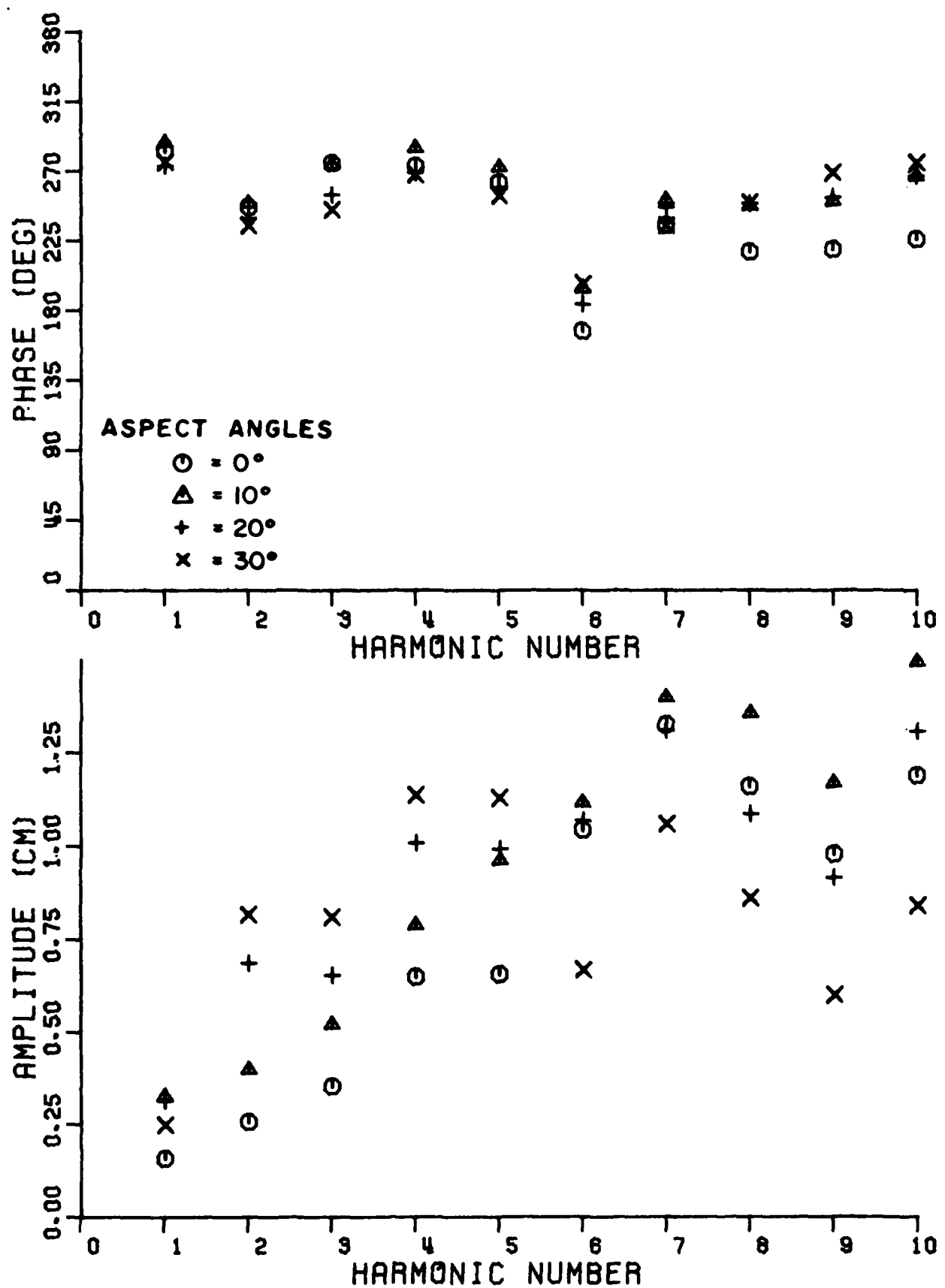


Figure 6b. Amplitude and phase data on cone #2 as a function of frequency. (horizontal polarization)

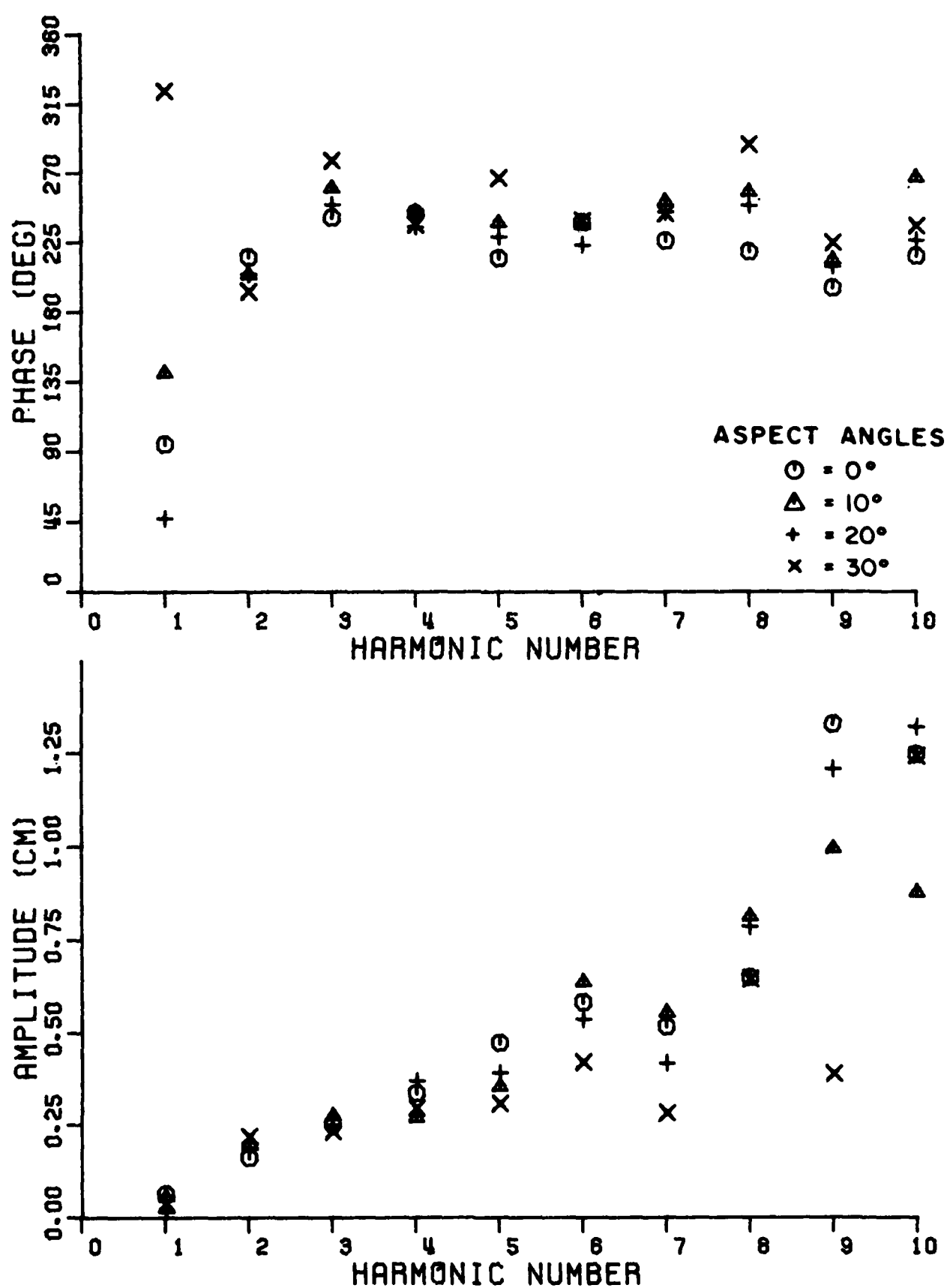


Figure 7a. Amplitude and phase data on cone #3 as a function of frequency. (vertical polarization)

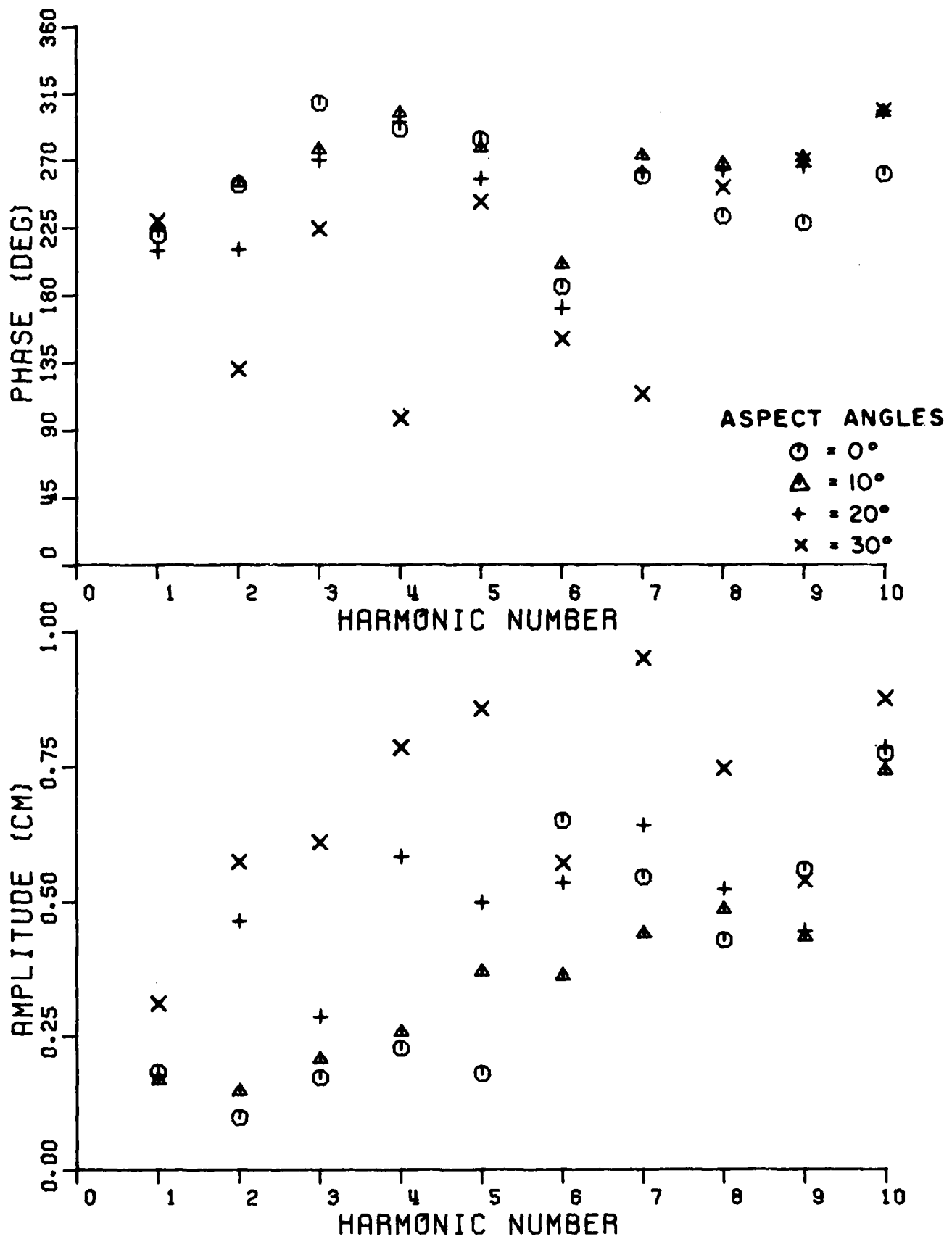


Figure 7b. Amplitude and phase data on cone #3 as a function of frequency. (horizontal polarization)

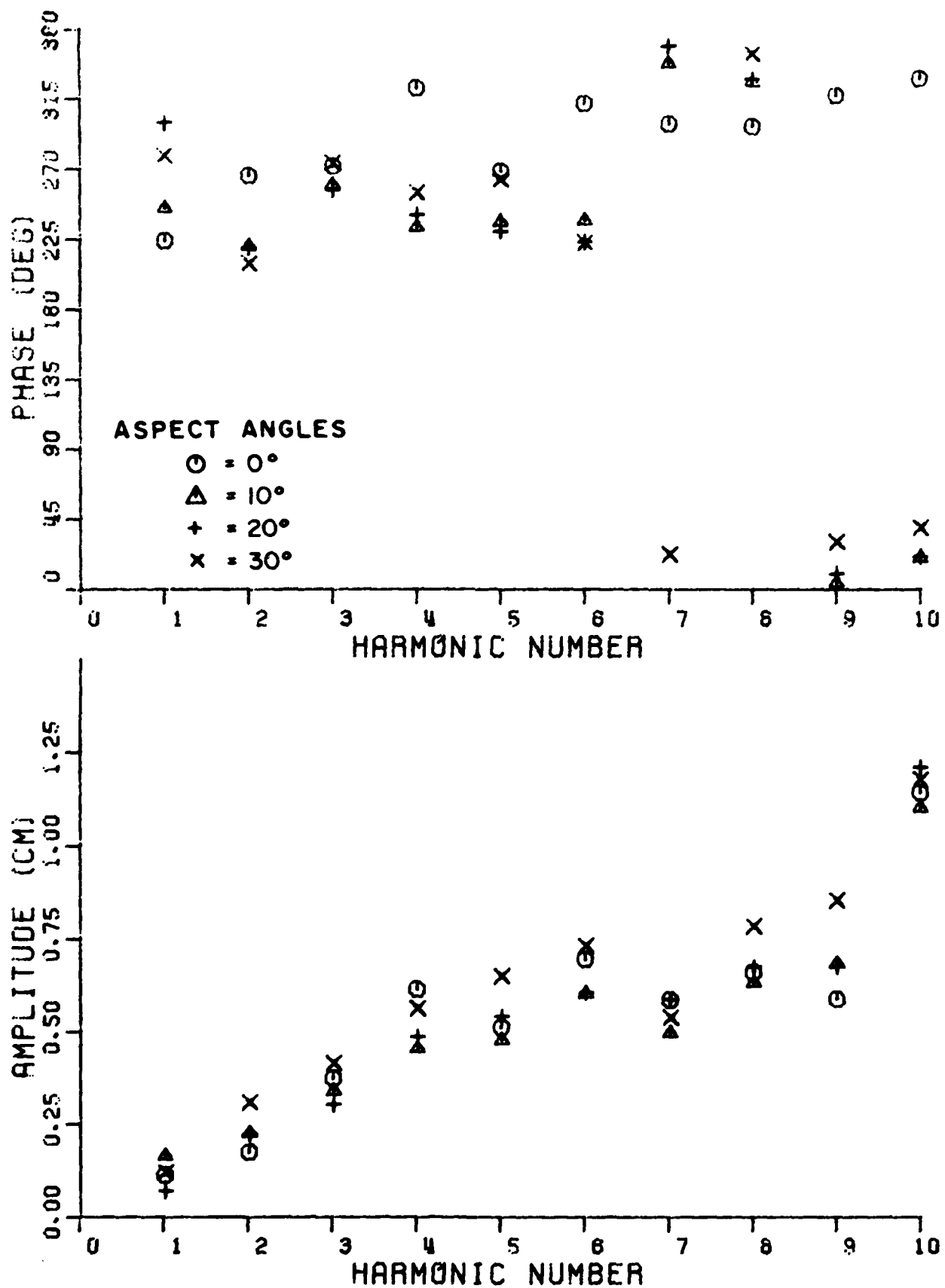


Figure 8a. Amplitude and phase data on cone #4 as a function of frequency. (vertical polarization)

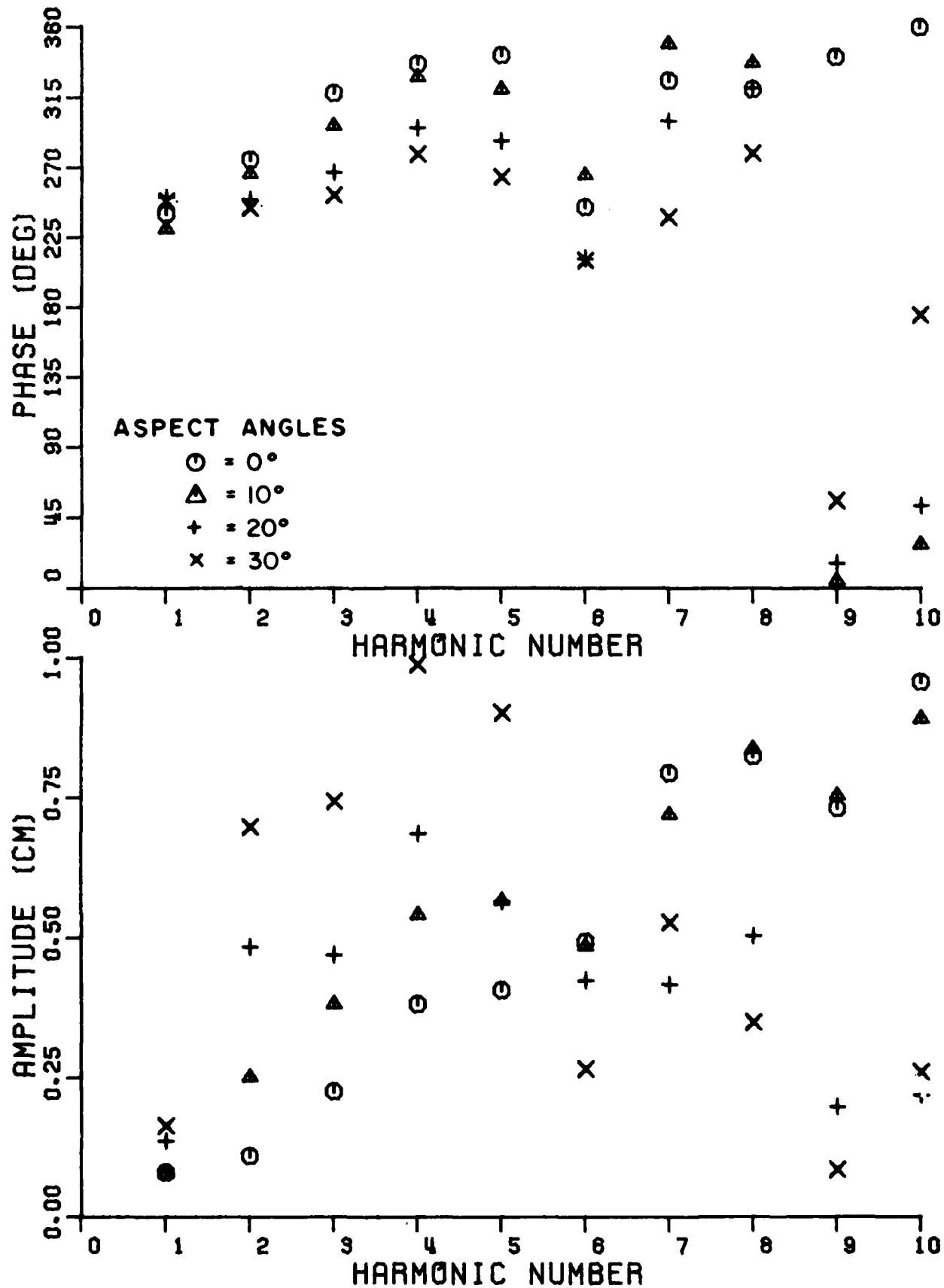


Figure 8b. Amplitude and phase data on cone #4 as a function of frequency. (horizontal polarization)

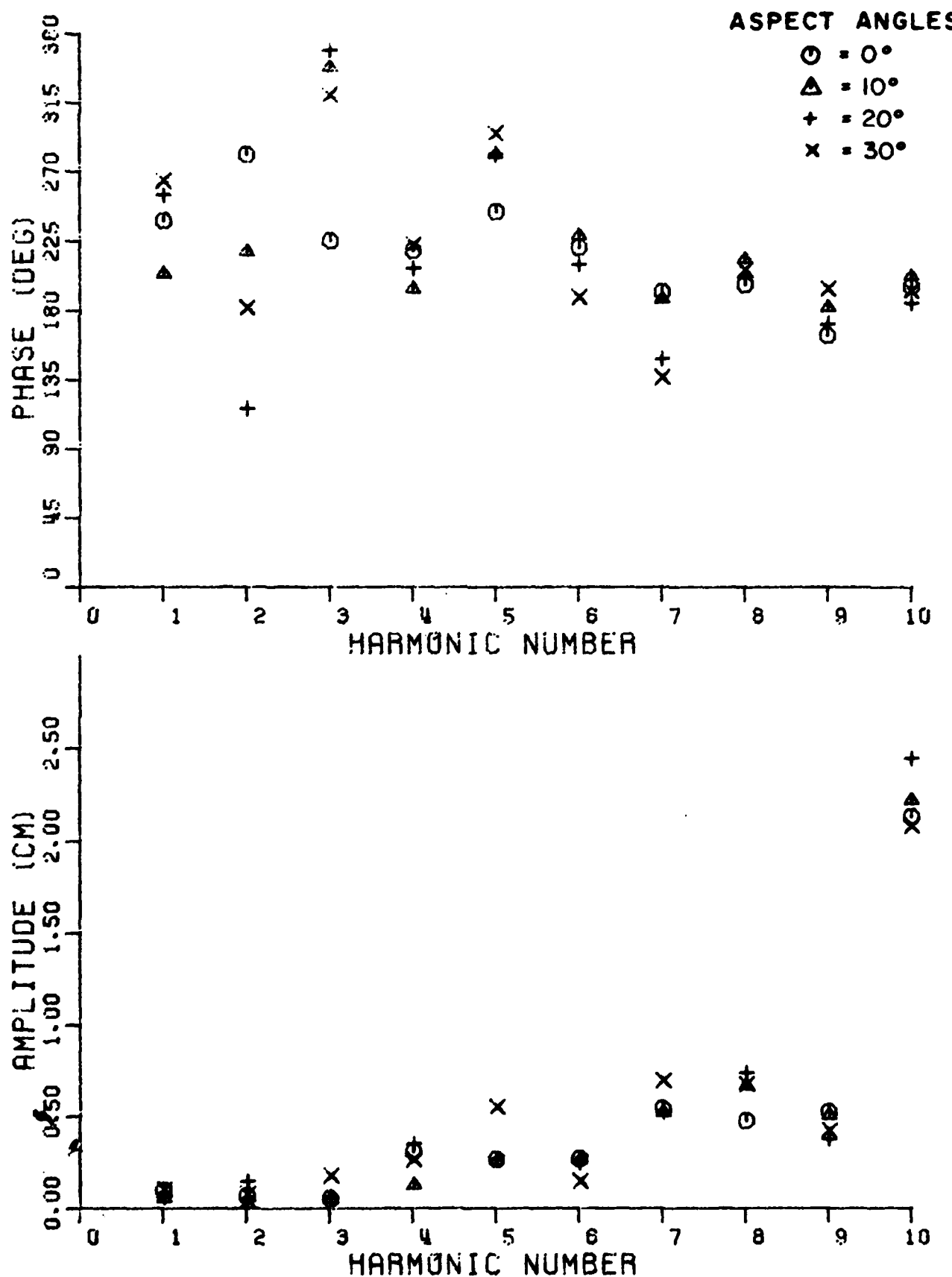


Figure 9a. Amplitude and phase data on cone #5 as a function of frequency. (vertical polarization)

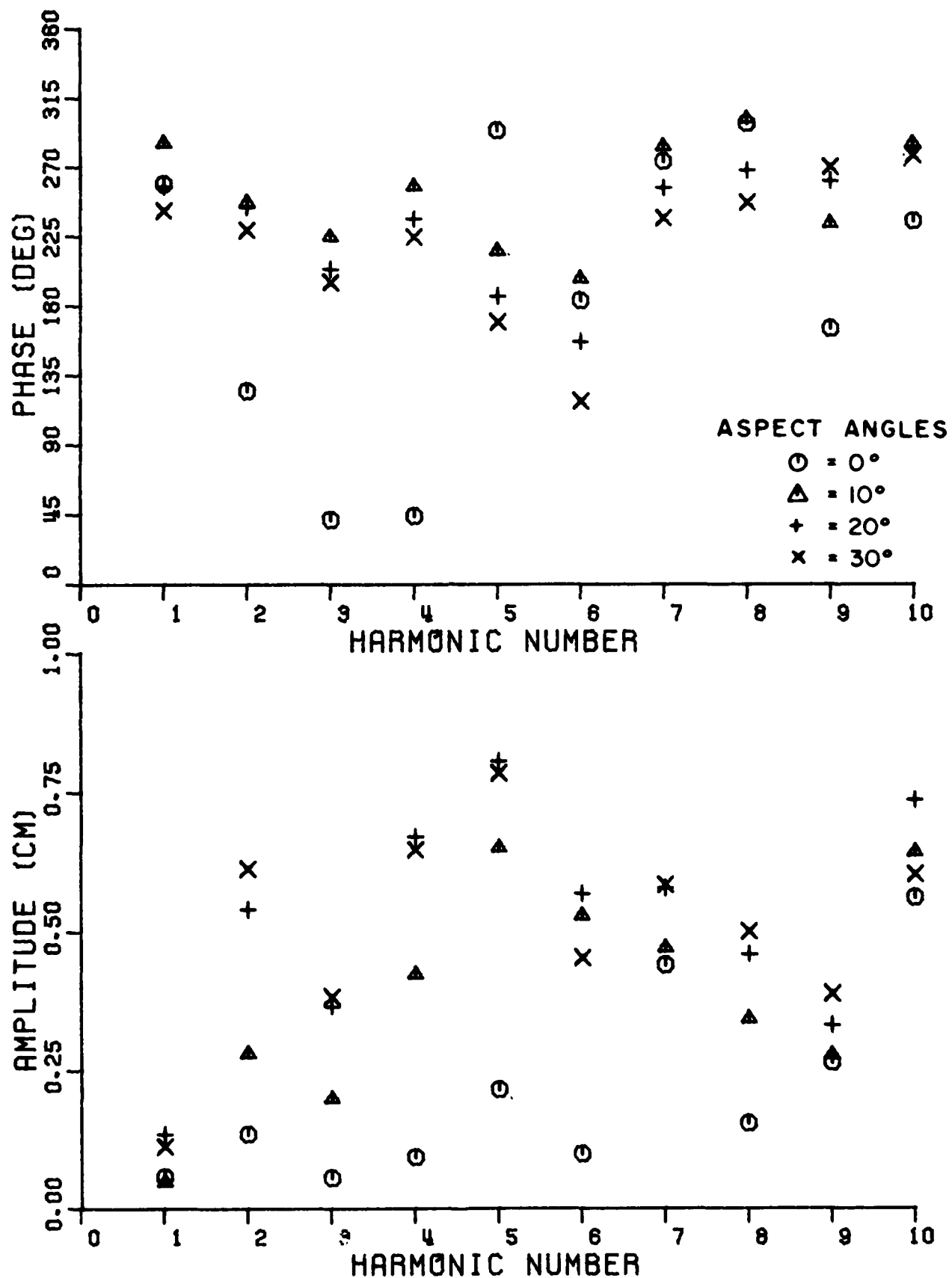


Figure 9b. Amplitude and phase data on cone #5 as a function of frequency. (horizontal polarization)

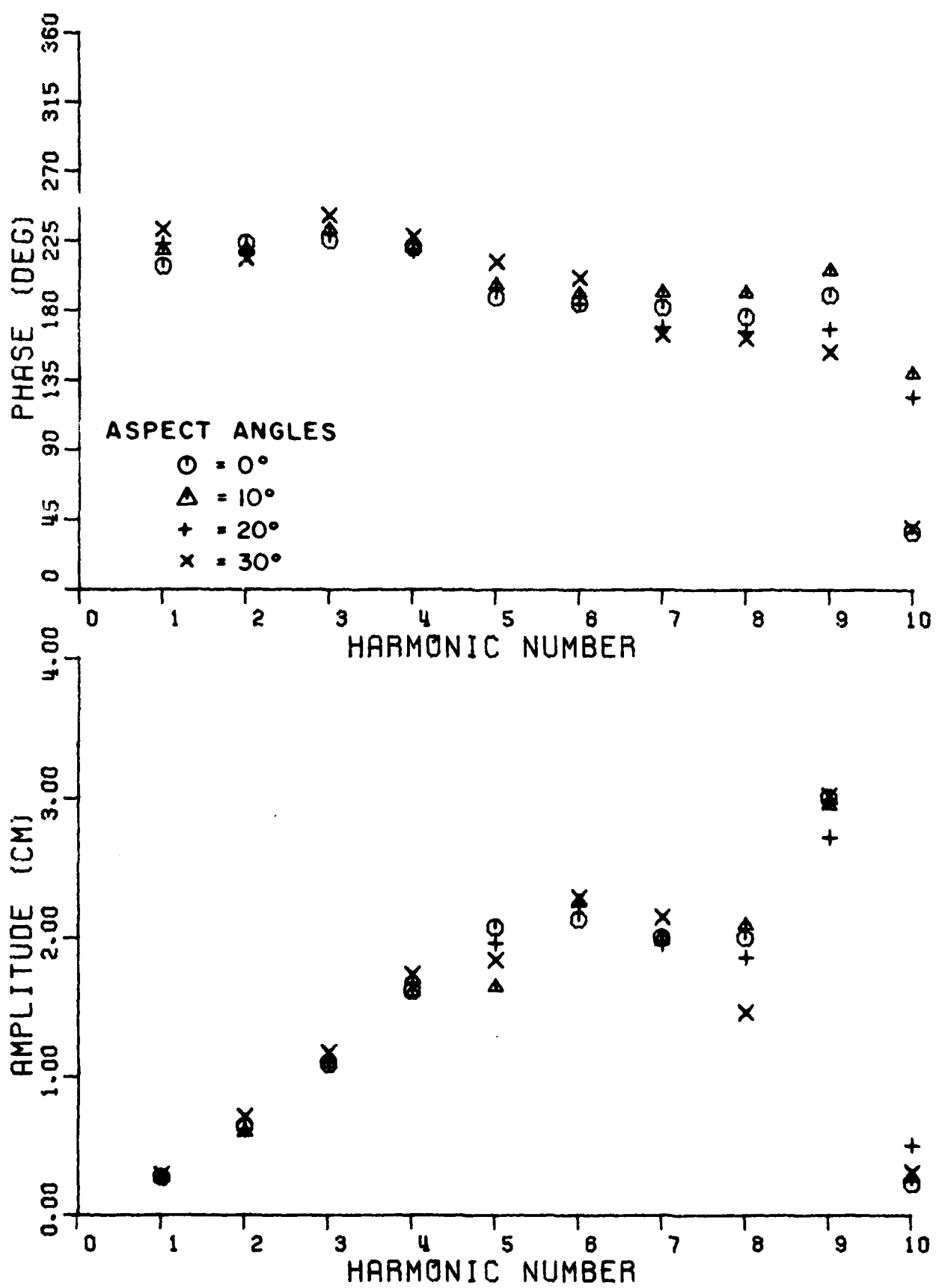


Figure 10a. Amplitude and phase data on cone #6 as a function of frequency. (vertical polarization)

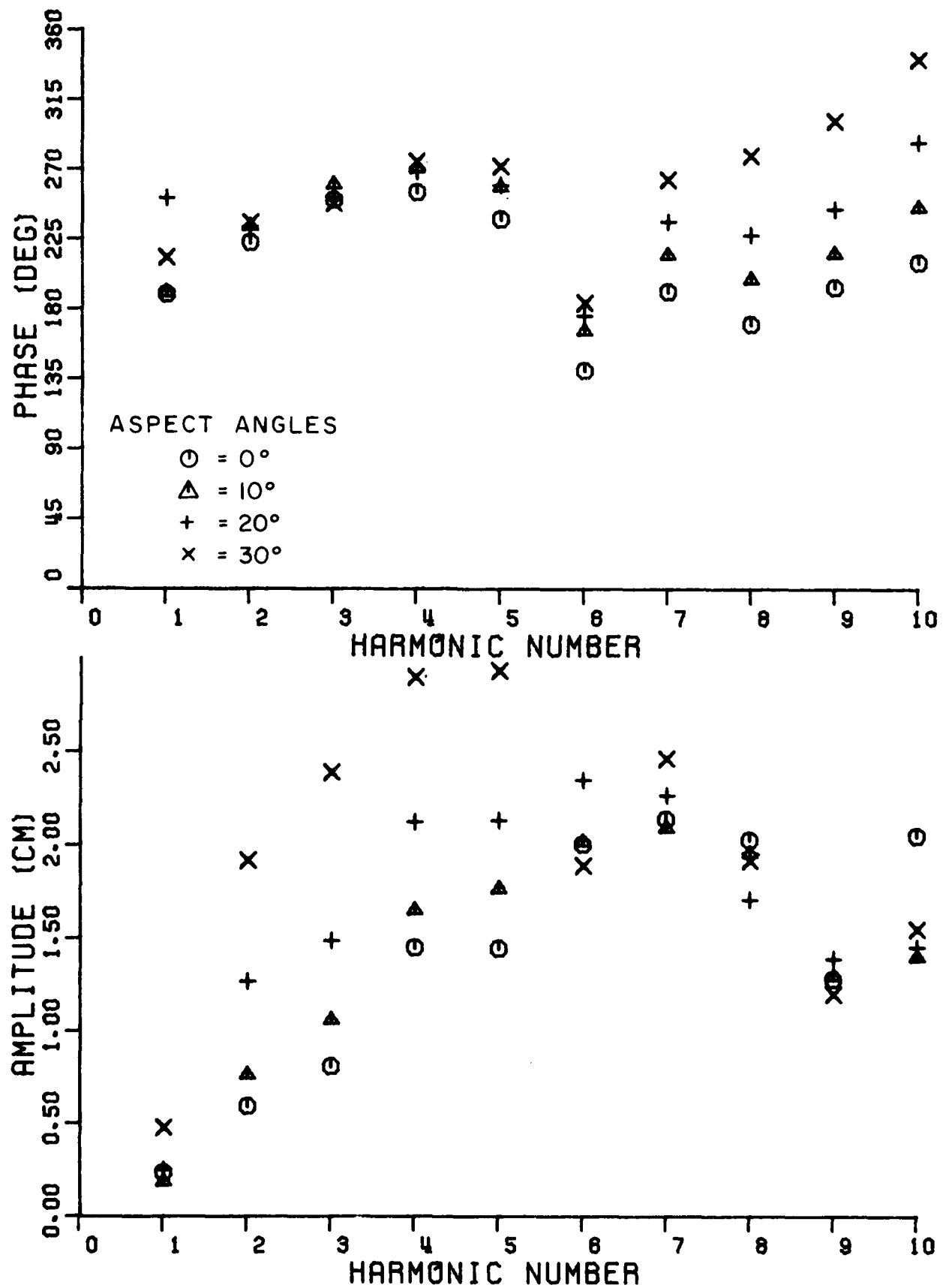


Figure 10b. Amplitude and phase data on cone #6 as a function of frequency. (horizontal polarization)

sections. This can cause the data to be accepted even though the cone data contain large errors. Our procedure has been to use the theoretical results to indicate the presence of errors and to use the computed values where accurate measurements could not be obtained. This procedure will be discussed in the section on time domain computations.

#### D. Large Target Measurements

In order to obtain data in the high frequency regime on the cone targets, a set of targets eight times larger than the original set was constructed. It was not possible to measure the cross section of these targets in the same way as the original target set, however. It is expected that the large targets are much more sensitive with respect to frequency and aspect angle than the small targets. Ten measurements over a 10 to 1 band of frequencies will not be sufficient to represent the radar behavior of the large targets.

For these reasons, it was decided to implement a swept frequency radar system. In such a system, the target would be stationary, and the signal to noise improvement introduced by the moving target data processing system would not be available. On the other hand, the targets would have radar cross sections approximately 64 times larger due to their 8 times larger dimensions. The basic concept of the swept frequency system and the steps in the measurement of the data are shown below.

- (1) Measure and store in computer files amplitude and phase readings as the frequency is stepped over a band of frequency. Readings are taken on the targets, on reference and check spheres, and on the background.
- (2) Subtract (phasor subtraction) the background data from the various target and sphere data to remove the errors due to various antenna coupling and unwanted scatter effects.
- (3) Use computed values of the reference sphere to calibrate the system in terms of absolute radar backscatter cross section (amplitude and phase).
- (4) Use data on the check sphere to confirm the overall integrity of the system and the data.

The major problem in the above set of concepts is due to constraints on the frequency repeatability of the swept frequency system. If the background is to be subtracted from the data on the various targets, then the frequency for each step in the frequency sweep must be repeatable to a high degree. The constraint is that the amplitude and phase of the background must be unchanged when the target is introduced. This can be assured if the set of data samples is taken at nearly identical frequencies for the background and for the set of targets. These qualitative comments were studied early in this contract. As part of this study, measurements

were made of the relationship between phase deviations due to frequency deviations and analog voltage variations due to frequency deviations. Typical results are;

Estimated phase accuracy requirement	= $\pm$ 5 deg.
Typical resultant frequency resolution	= $\pm$ 0.003 GHz
Resultant analog voltage accuracy	= $\pm$ 0.0088 volts/10 volts
Absolute voltage accuracy	= $\pm$ 1 part in 1100 (10 bits)

The analog voltage accuracy discussed in the above list is the voltage accuracy that would be needed if an analog voltage was used to control the frequency of the available microwave sweep frequency oscillator. This required voltage accuracy of (typically) 1 part in 1100 would require a design accuracy of perhaps 1 part in 2000 (11 bits). This stringent analog voltage stability and resolution requirement must be maintained even though the relationship between voltage and frequency is dependent on the sweep oscillator front panel dial settings. The analog system would require calibration each time the equipment was adjusted. It is these limitations which resulted in the decision to build a digital interface between the digital frequency counter and the computer. Experiments indicated that the drift in the internal oscillator in the frequency counter would not cause significant errors in the system. The output is inherently of high resolution (better than 5 decimal digits (1 part in 10,000) and requires no calibration at all. Implementation of the digital system has been completed and the system is shown in block diagram form in Figure 11. A computer flow diagram of the software that was implemented to operate the digital frequency sweep system is shown in Figure 12.

#### E. Theoretical Studies

In order to evaluate the measurements in an orderly fashion, theoretical computations of the radar cross-sections of the cone targets were necessary. The low-frequency regime is represented using a Rayleigh calculation, while the high frequency regime is represented using the Geometrical Theory of Diffraction (GTD), and the Equivalent Current Theory.

The Rayleigh results are taken from Seigel [7] and from Crispin and Siegel [8]. The Rayleigh region backscatter cross section calculation derived by Seigel is given below:

$$\sigma = 4\pi k_0^4 |f_0|^2 \quad (1)$$

where  $f_0$  is the coefficient of the leading term of the (poorly known) series expansion in powers of  $k_0$  of the exact solution. Seigel gives the final solution as

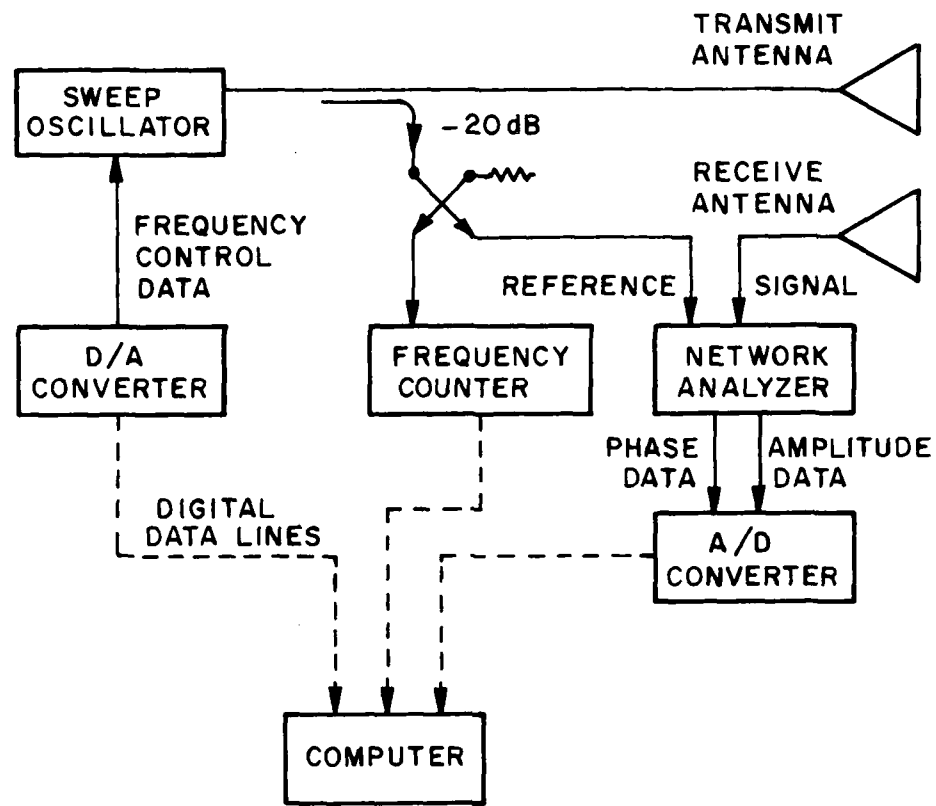


Figure 11. Block diagram of digital frequency sweep radar system.

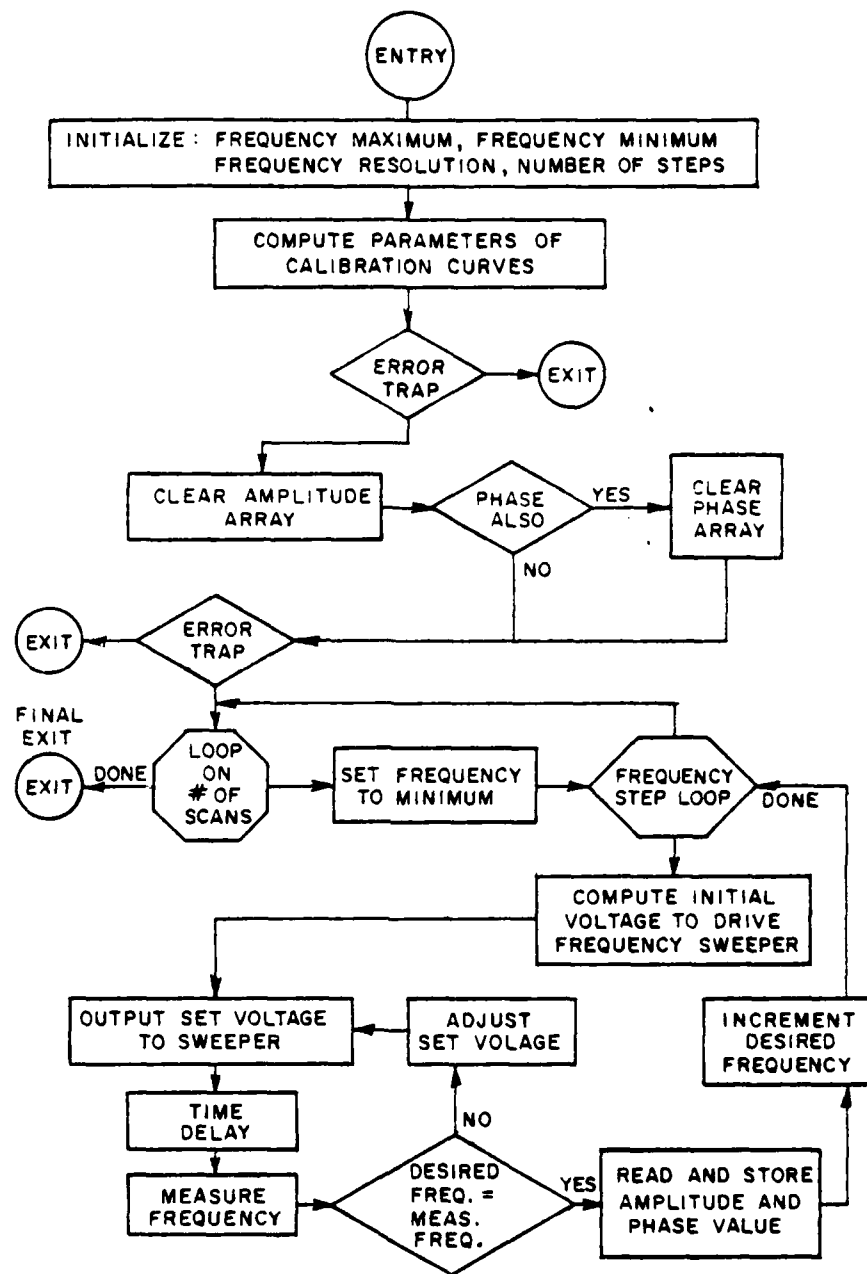


Figure 12. Computer flow diagram of digital frequency sweep radar system.

$$\sigma = \frac{4\pi}{9} k_0^4 a^4 h^2 \left[ 1 + \frac{4a \exp(-\frac{h}{4a})}{\pi h} \right]^2 \quad (2)$$

as long as

$$\sqrt{h^2 + a^2} \ll \frac{\lambda_0}{2\pi} \quad (3)$$

where

$h$  = altitude of cone

$a$  = base radius .

These results are for the magnitude of the radar cross section only, and no phase values are given. The phase of the backscattered signal was approximated in this study by taking the center of surface area (excluding the base) of the cone targets to be the scattering center. (The phase reference zero in all of this work is taken at the base of the cones.)

There are a large number of references on the Geometrical Theory of Diffraction as applied to the finite cone. Most of the references are linked to the paper by J. B. Keller [9], and this is a good starting point in spite of the number of corrections to this paper which appear later in the literature (some by the author himself). A development of the Geometrical Theory of Diffraction (GTD) is beyond the scope of this report, and is readily available in the literature. Basically, the method generates a catalog of important electromagnetic ray paths and considers the behavior of the primary rays of the radar system. The diffraction of rays from points and from wedges etc. are tabulated and combined to form a representation of the signal backscattered from the target. In the studies presented here, the cone backscatter was represented by the first order rays diffracted directly back to the radar by the edges at the base of the cone as well as the secondary rays diffracted across the base of the cone and then diffracted again back to the observer. The equation as given by J. B. Keller [9] is

$$\begin{aligned} E_{e1}(r,0) + E_{e2}(r,0) &= \\ &= \frac{a \bar{A} \sin(\frac{\pi}{n}) \exp[ik(r+2a \cot\gamma)]}{nr} \cdot \left[ (\cos \frac{\pi}{n} - \cos \frac{3\pi}{n})^{-1} \right. \\ &\quad \left. + \frac{\sin(\frac{\pi}{n}) \exp(2ika - i\frac{\pi}{4})}{2 n (\pi ka)^{1/2}} \cdot (\cos \frac{\pi}{n} - \cos \frac{3\pi}{2n})^{-2} \right] \end{aligned} \quad (4)$$

where the backscattering cross section

$$\sigma_{EM}(0) \text{ is } 4\pi r^2 |\bar{A}|^{-2} \cdot [|E_{e1}(r,0) + E_{e2}(r,0)|^2] \quad (5)$$

in these equations,

- $E_{e1}(r,0)$  is first order backscatter
- $E_{e2}(r,0)$  is second order backscatter
- $\bar{A}$  is amplitude of incident field
- $n$  is  $\frac{3}{2} + \frac{\gamma}{\pi}$
- $k$  is the wave number
- $r$  is range coordinate
- $a$  is base radius
- $\gamma$  is cone half angle

As was mentioned, these equations consider first order and second order backscatter.

A second method of computing the radar cross section of the cone targets is the equivalent current theory of Burnside and Peters [10]. The equivalent current referred to in this development is a current which radiates the same fields as the particular target. In this sense, it is not a target surface current. The diffraction mechanism considered here is similar to that of the GTD method discussed earlier since Burnside and Peters consider the same first order and second order diffraction mechanisms. The equations which describe the radar cross section and the total back-scattered fields are given below.

$$\sigma = 4\pi a^2 | -G(n,a) - \frac{j}{2} G(n, \frac{3\pi}{2}) \cdot [v_B(n, 2a, \frac{3\pi}{2}) + v_B(n, 2a, \frac{3\pi}{2} + \alpha)] |^2 \quad (6)$$

$$\text{with: } v_B(n, r, \phi) = \frac{\exp(-\frac{j\pi}{4}) \exp(-jkr)}{(2\pi kr)^{1/2}} G(n, \phi^{\pm}) \quad (7)$$

$$\text{and: } G(n, \phi^{\pm}) = [\frac{1}{n} \sin(\frac{\pi}{n})] (\cos \frac{\pi}{n} - \cos \frac{\phi}{n})^{\pm -1} \quad (8)$$

where:  $\phi^{\pm} = \psi^{\pm} - \psi_0$

$\psi$  = angle from cone surface to observer

$\psi_0$  = angle from cone surface to source

$n = 2(1 - \frac{\alpha}{2\pi})$

$\alpha$  = cone angle

$k$  = wave number

$a$  = base radius

$r$  = range to observer.

Results based on these equations will be given shortly.

Before discussing comparisons between these computed results and the experimental data, one further source of comparison data should be discussed. A large set of radar cross section data was published in 1959 by Keys and Primich for the Canadian Department of National Defense [11]. The cross-section of 84 cones was measured as a function of aspect angle at both horizontal and vertical polarization (as defined earlier in this report). The cone half angles ranged from 4 to 20 degrees and the base diameters ranged from 0.297 to 2.87 wavelengths (in 14 steps). Curves of the amplitude of the radar cross section as a function of the aspect angle are available. No phase data is available. In several of the comparisons included in this report, values from this Keys and Primich study are included. It should be remembered that the accuracy of these values is on the order of  $\pm 2$  dB.

Comparisons between these various theories and measurements and the data that was measured in this program will be discussed next. In this part of the report, the frequency domain results and comparisons will be given. Time domain comparisons will be given later in this report.

Figures 13-16 show the comparisons between the various theoretical and experimental results. In these figures, the experimental cone data are all taken from the zero degree aspect angle data sets. In fact, the theoretical results shown here were computed for monostatic backscatter at zero degree aspect angle. The major problem, then, is to reconcile the monostatic theoretical values with the measured 20 degree bistatic angles. It can be shown [8] that at high frequencies the monostatic and bistatic results are equal. Observation of our comparison between theory and measurement at lower frequencies indicate that our errors are small at low frequencies as well.

The general behavior of the set of comparisons can be discussed at this point. The most obvious observation is that there is often a region of the frequency domain data where none of these theoretical computations can be used to accurately predict the behavior of the cone target. In this region of difficulty, the Rayleigh computations fail because the

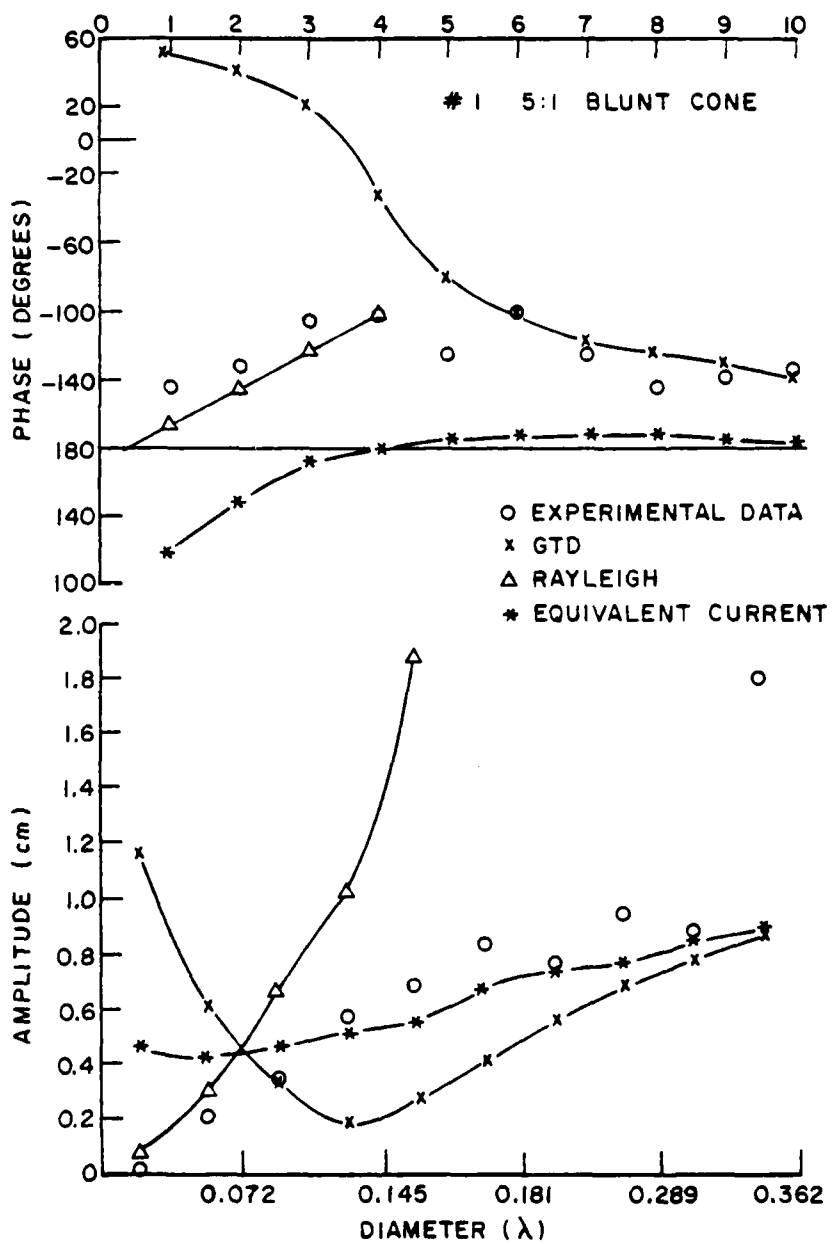


Figure 13. Comparison between theoretical and experimental results for the amplitude and phase versus frequency for target number 1.

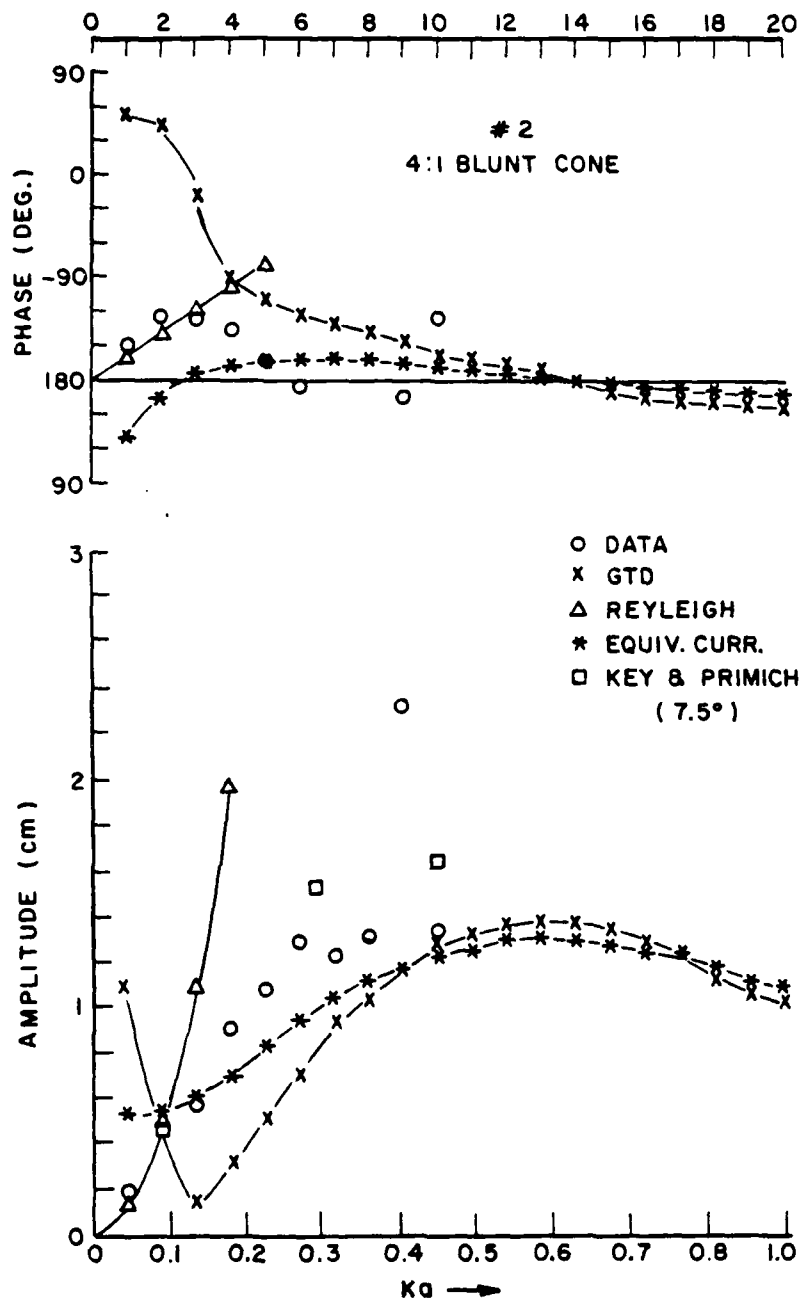


Figure 14. Comparison between theoretical and experimental results for the amplitude and phase versus frequency for target number 2.

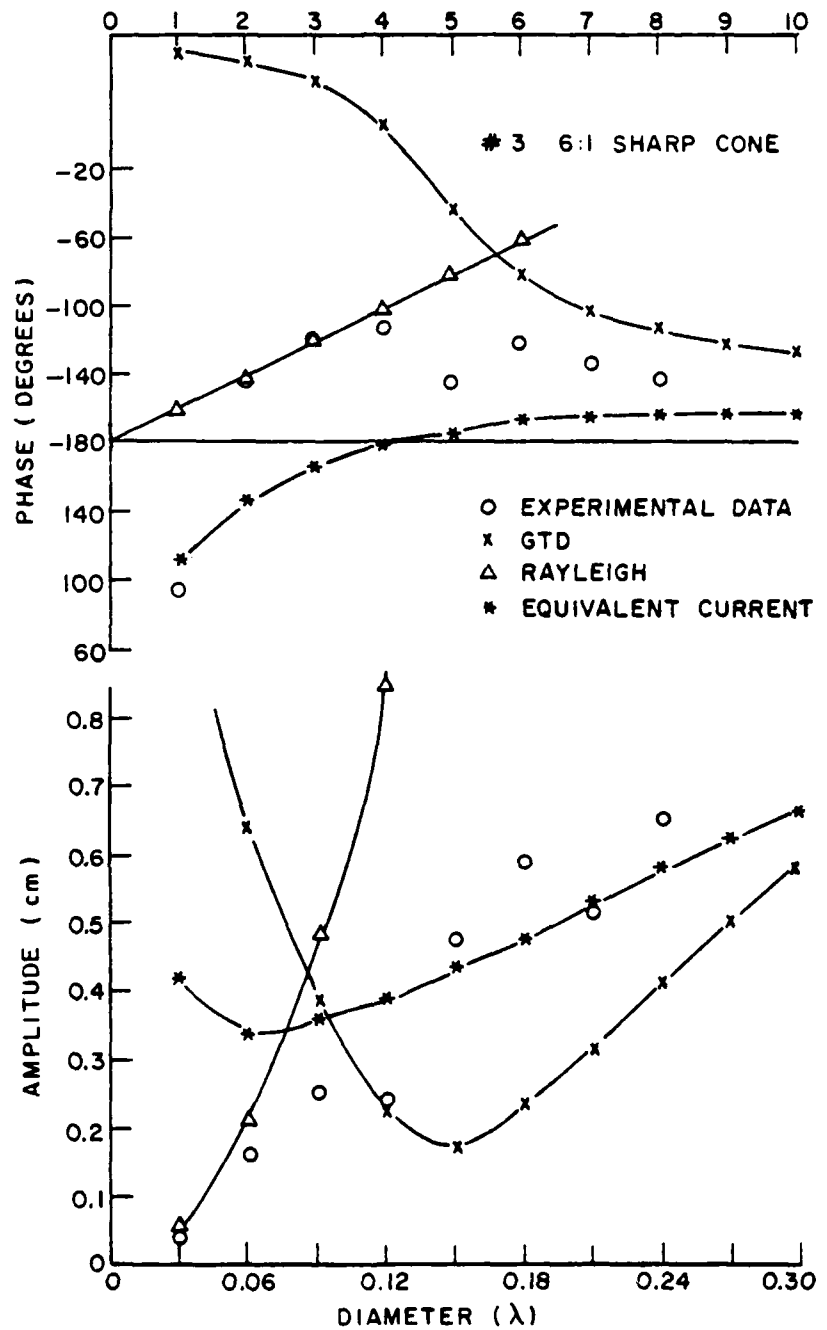


Figure 15. Comparison between theoretical and experimental results for the amplitude and phase versus frequency for target number 3.

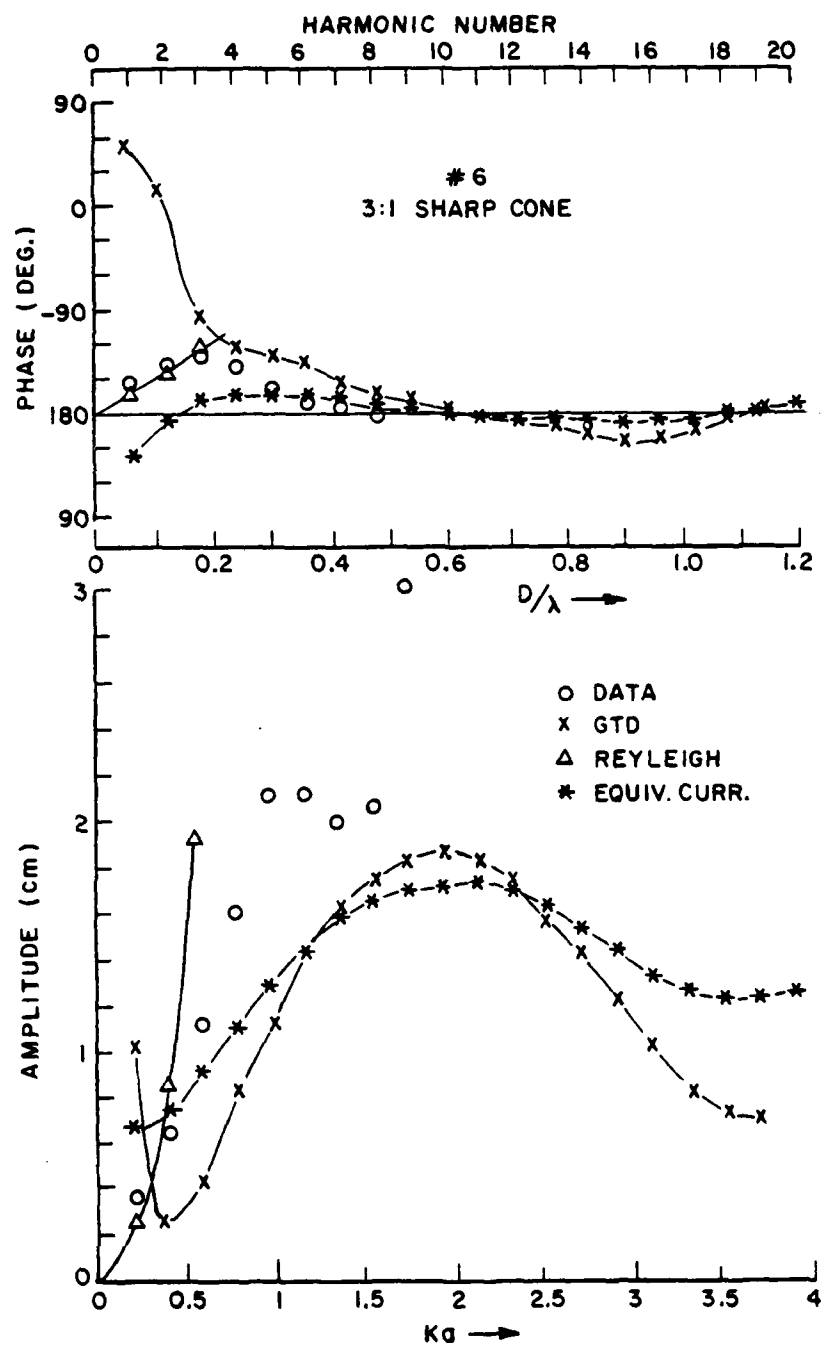


Figure 16. Comparison between theoretical and experimental results for the amplitude and phase versus frequency for target number 6.

frequency is too high, and the GTD and equivalent current theory fail because the frequency is too low. It is in this regime where confidence in the measurements is very important since there is no independently derived information on the radar cross section. Often, this region where the computations fail is where the diameter of the cone is from 1/50 to 1/4 wavelengths. In general it can be seen that the GTD and equivalent current results become fairly accurate when the base diameter of the cone is 1/3 to 1/2 wavelength or greater. This implies an extension of physical optics approximations (of which the GTD and equivalent current solutions are special types) to lower frequencies than is usually the case.

Conversion of these frequency domain data to the time domain will be discussed in the next part of this report.

### III. RAMP RESPONSES AND LIMITING SURFACE IMAGES

#### A. The Ramp Response Waveform

The ramp response signature is the basis for the limiting surface imaging technique used in this study. The relationship between a target's ramp response and its geometrical properties was suggested by Kennaugh and Moffatt in 1965 [12]. The basic result is that

$$F_R(z) = -\frac{1}{\pi} A(z) \quad (9)$$

where  $F_R(z)$  is the time domain ramp response and  $A(z)$  is the target cross sectional area versus distance along the direction of propagation of the incident field. This relationship was first exploited in a radar imaging technique by Young in 1971 [13]. A practical radar system cannot be used to measure an exact ramp response due to the bandwidth requirements. The alternative used is to measure 10 harmonically related samples of the targets spectral response. These samples are then properly weighted and combined to construct a 10-frequency Fourier series approximation of the target's ramp response signature. The expansion for the periodic ramp response  $F_R(t)$ , is

$$F_R(t) = N \sum_{n=1}^{10} \frac{A_n}{\sqrt{\pi n^2}} \cos(n\omega_0 t + \phi_n) \quad (10)$$

where  $A_n$  are the measured amplitudes of the spectral response samples,  $\phi_n$  are the measured phases, and  $\omega_0 = (2\pi)(1.08 \times 10^9)$  rad/sec. The measurement system is documented in Section II. A more complete discussion of the ramp response waveform may also be found in Reference [13].

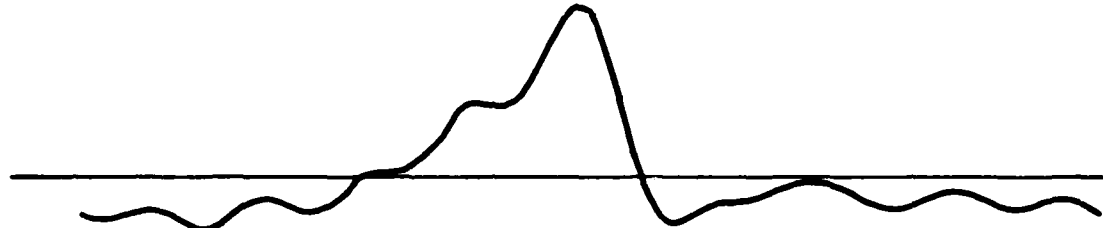
## B. Ramp Response Processing

The ramp response derived from radar cross section phase and amplitude versus frequency data must be further processed to yield useful imaging results. The modification of these waveforms is based upon known geometrical constraints. The ramp response was shown to be proportional to the cross sectional area versus distance of the target. The response should therefore be zero outside the main region of the response, i.e., the region corresponding to the target. However the response, as constructed above, does not satisfy this because it's D.C. term was not measured. Previously, the D.C. term was removed by shifting the waveform using visual estimation and the CRT display and light pen. However, in order to study error associated with the imaging process more closely, it was necessary to systemize this procedure. The ramp response for target 2, a 4:1 blunt cone, at a  $0^\circ$  look angle with vertical polarization is shown in Figure 17a. The portion of the waveform ahead of the main response is averaged. The entire waveform is then shifted by this amount as in Figure 17b. However a non-zero response still exists outside of the target region due to Gibbs phenomena ripple introduced by bandlimiting. These portions of the waveform are set to zero by truncating the curve at the points where the main response swings negative. This is shown in Figure 17c.

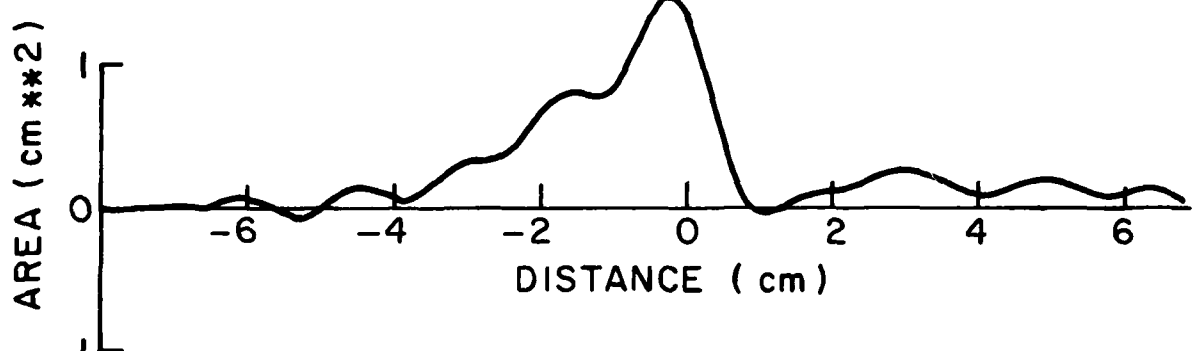
When imaging with multiple look angles a second constraint must also be satisfied. The volume of the target as seen from each look angle must be consistent. To comply with this requirement, each shifted and truncated waveform for a particular target is integrated and the resulting volumes are averaged. Each waveform is then scaled so that the volume as seen from each look angle is equal to the average volume. Figure 18 shows a set of shifted and truncated ramp responses for target 2 for  $0, 10, 20$  and  $30^\circ$  look angles before scaling. The volumes for each are indicated and range from  $1.98 \text{ cm}^3$  to  $3.25 \text{ cm}^3$ . The average is  $2.58 \text{ cm}^3$ . Figure 19 shows the waveforms after scaling. Once a set of waveforms have been thus processed they are ready for imaging.

## C. Ramp Responses for Cone-like Targets

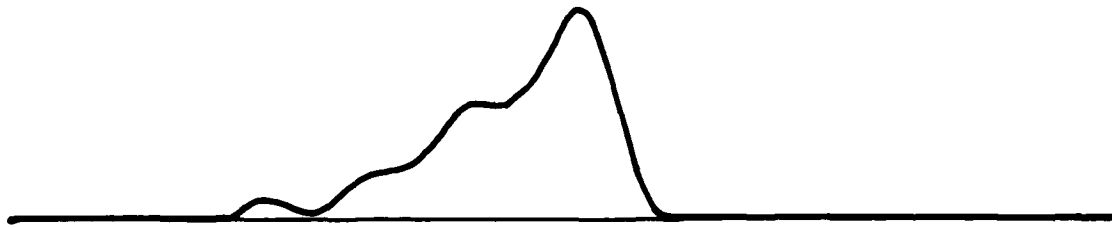
Although the goal of radar imaging is to aid in target discrimination, several valuable characteristics can be obtained directly from the ramp response signatures. Figures 20a-f are scaled, vertical polarization, nose-on ramp responses for targets 1 through 6, respectively. The actual target profile functions are included for comparison. Due to a significant phase measurement error associated with the first harmonic, it was necessary to alter this phase value before constructing several of the ramp responses. In particular, the first harmonic phases for targets 1, 3, 4 and 5 were set to  $180^\circ$ . The justification for this stems from the backscatter behavior predicted in the Rayleigh region as discussed in Section II-E. A full set of shifted, unscaled ramp responses for each target are presented in Appendix B. Vertical and horizontal polarization ramp responses are included. In addition, ramp responses are included with altered and unaltered 1st harmonic phases.



(a) UNALTERED WAVEFORM



(b) SHIFTED WAVEFORM



(c) WAVEFORM WITH TAILS TRUNCATED

Figure 17. Ramp response modification.

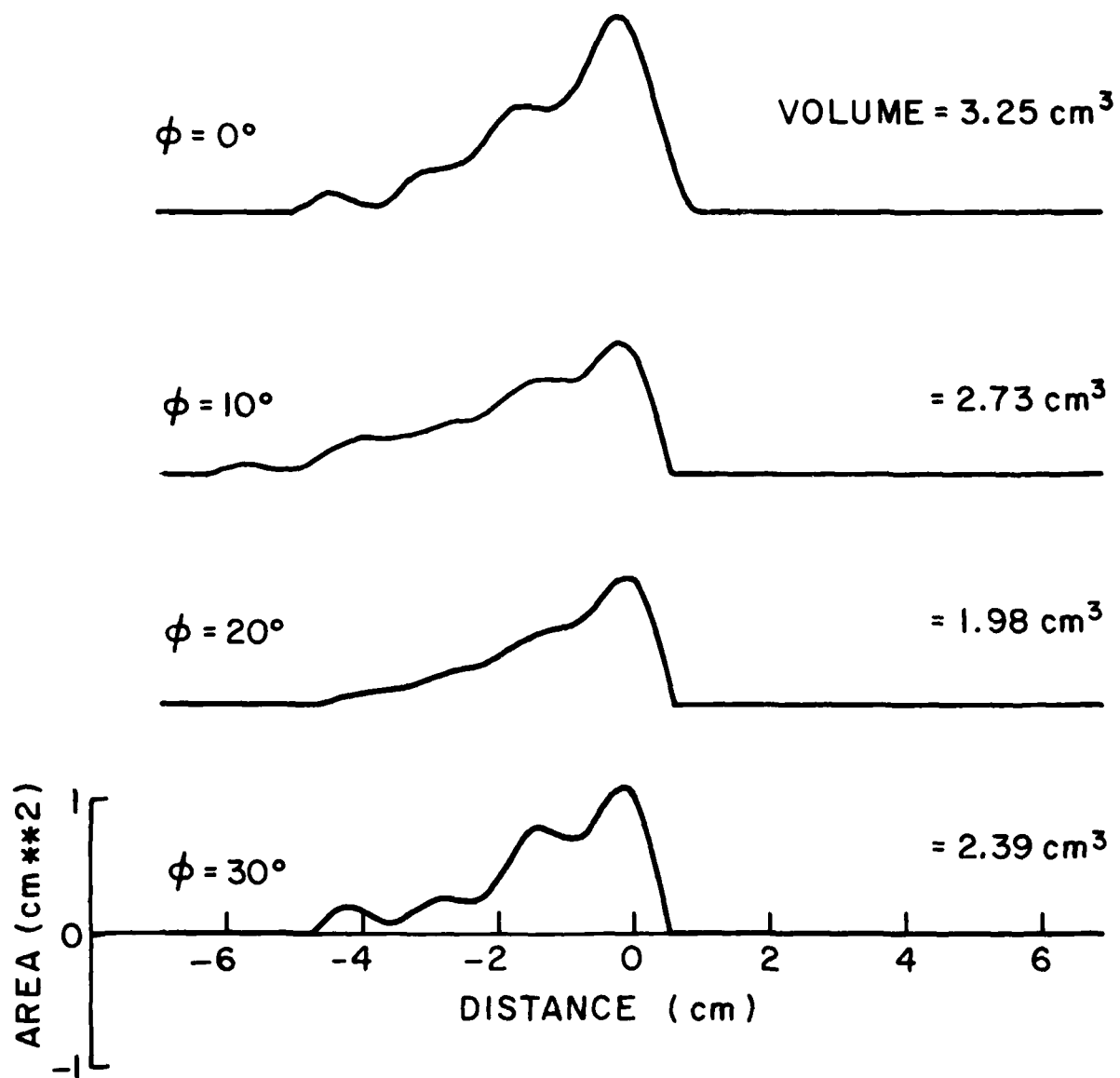


Figure 18. Unscaled profile functions for target 2.

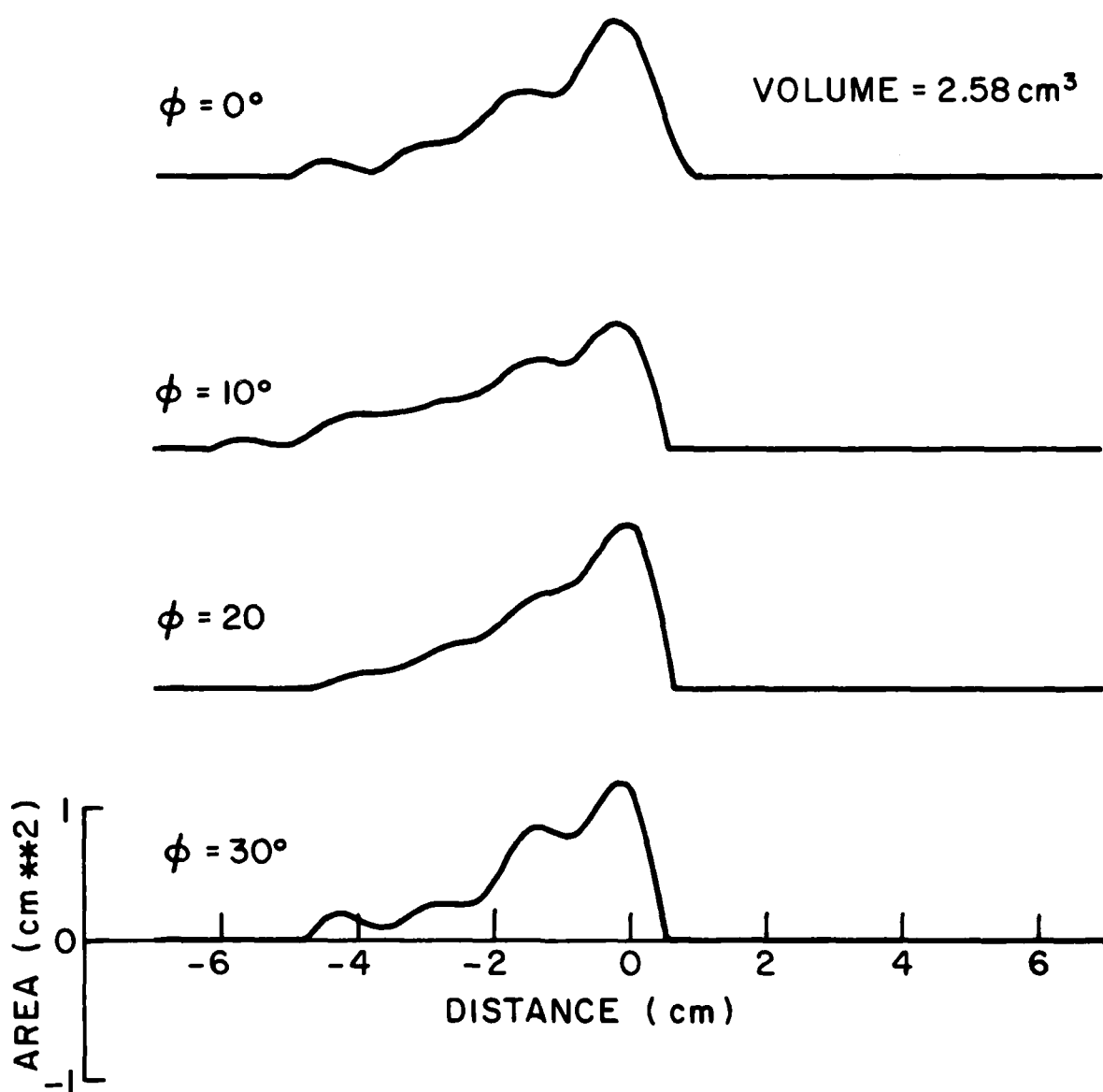


Figure 19. Scaled profile functions for target 2.

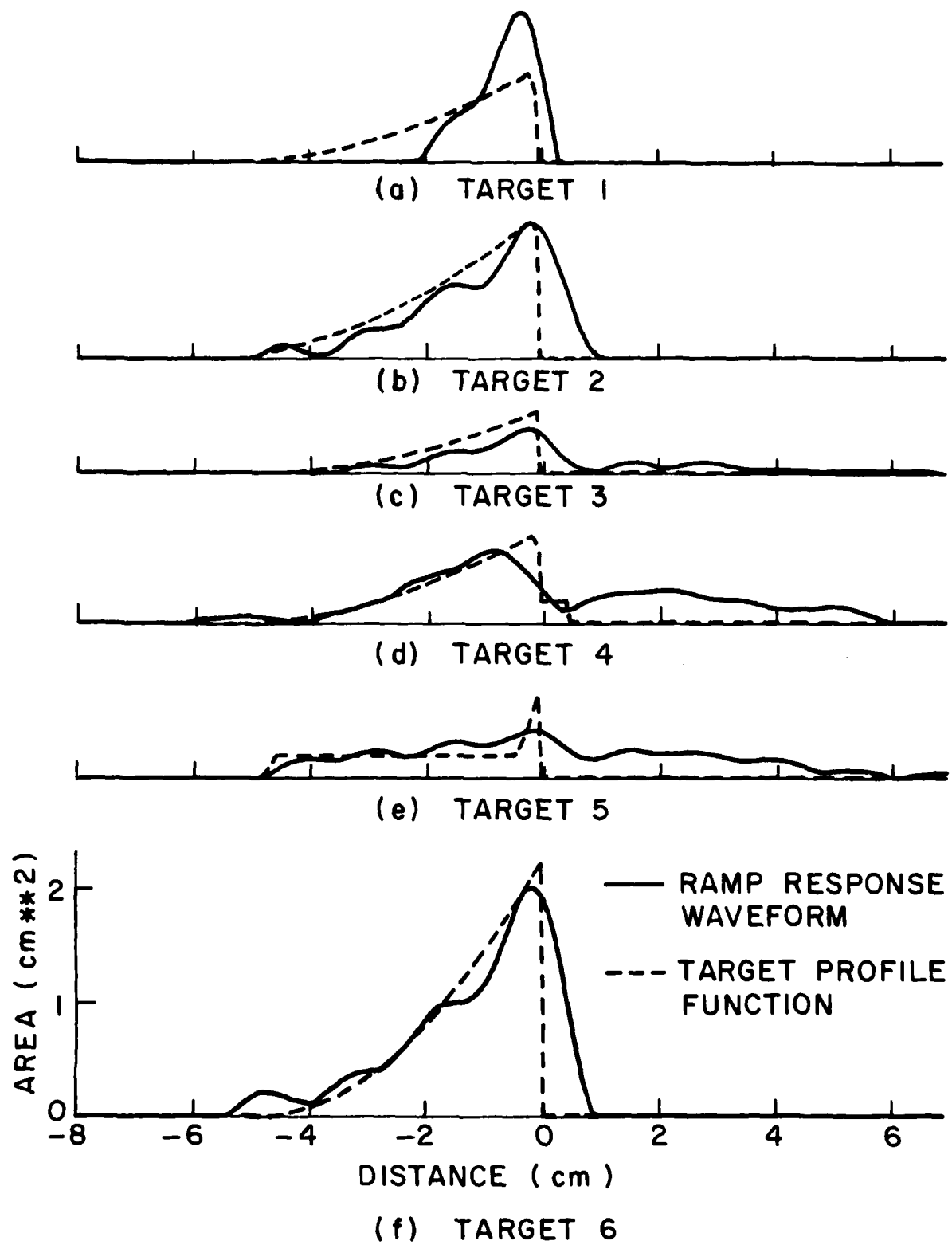


Figure 20. Vertical polarization ramp responses and profile functions from nose on incidence for all targets.

One important target characteristic which can easily be derived from the ramp response is target volume. Table III-1 contains the actual volume for each target along with the volume measured from the ramp response.

TABLE III-1  
TARGET VOLUMES

TARGET	CALCULATED VOLUME (cm <sup>3</sup> )	MEASURED VOLUME (cm <sup>3</sup> )	VOLUME ERROR
1	1.31	1.56	.16
2	2.04	2.59	.21
3	0.91	0.98	.07
4	1.41	2.56	.45
5	1.28	2.20	.42
6	3.64	4.58	.20

In each case, the measured volume is greater than the actual volume due to the slow decay of the trailing edge of the waveforms. However, for four of the targets the volume error is less than .21. These four targets, namely targets 1,2,3, and 6 could be discriminated on the basis of volume alone. The disagreement with target 5 is due to the fact that this target has the smallest radar cross section of any of the targets and is too small for satisfactory experimental results.

Most of the targets can also be discriminated from the slope of the ramp response leading edge. With the exception of target 1, the waveforms in Figures 20a-f can be ordered according to slope to agree with the slopes of the actual profile functions. The ramp responses in order of increasing leading edge slope are 5, 3, 4, 2, and 6, which agrees with the actual profile functions. Target 1 does not agree because when the waveform was processed, the length was cut off along the 0° look angle more than along the other look angles. This caused the 0° ramp response to be scaled up excessively during the scaling process. From the ramp responses for target 1 in Appendix B, it can be seen that the slope of the ramp response leading edge corresponded much more closely to the actual target before scaling.

Targets 1 and 4 are identical except for the small cylinder on the back of target 4. As can be seen from the ramp responses in Appendix B, the trailing edges of the target 4 ramp responses fall off more gradually than those of target 1. The cylinder can therefore be detected, though not in detail.

One target feature is not detectable in the ramp responses. Targets 3, 5, and 6 have sharp tips and back edges, while targets 1, 2, and 4 have blunt tips and rounded back edges. The bandlimiting of the ramp response causes rounding off of all sharp discontinuities on the targets, thus overshadowing these details.

Figure 21 shows the unscaled, horizontal and vertical polarization ramp responses for target 2. As the look angle is increased, the horizontally polarized field excites a resonant mode on the target. The result is evident in the ramp responses. This resonant mode is not predicted by physical optics, which was used in the derivation of the ramp response approximation. The relationship between the ramp response and target profile function is therefore not valid when the incident field is polarized along the major axis of a long, narrow target.

#### D. Description of Limiting Surface Imaging Process

The limiting surface imaging process uses one or more profile functions for a given target as input. The idea is to fit a surface to the set of profile functions. An ellipsoidal limiting surface is used for each look angle. The specification of a series of input parameters is required. Two of the parameters,  $\theta$  and  $\phi$  specify the look angle for a particular profile function. The remaining parameters are in general, unknown and require a priori knowledge of the target geometry or iterative manipulation to achieve the best image. These parameters describe the ellipsoidal limiting surfaces to be used. A complete set of these parameters must therefore be specified for each look angle. A straight line along which the centers of ellipses are to be aligned must be specified. This center line is described by two angles,  $\alpha$  and  $\beta$ .  $\alpha$  is the angle between the center line and the look angle axis.  $\beta$  gives the rotation of the center line about the look angle axis with the  $y$  axis as the  $\beta=0$  reference. Gamma describes the tilt of the ellipses about the center line and is also referenced to the  $y$  axis. Each of these angles are depicted in Figure 22. In addition the aspect ratio for the ellipses must also be specified.

Functionally the imaging algorithm can be described as follows. For a given point in the  $x$ - $y$  plane the program iterates through values of  $z$ . For each  $z$  value the area of an ellipse corresponding to each look angle is calculated which passes through the point and satisfies the parameters specified for that look angle. If each of the areas are found to be less than the values of the corresponding points on the corresponding profile functions, then the point is assumed to lie within the volume of the target. The points with minimum and maximum  $z$  values which are found to be interior to the target are chosen to lie on a surface contour in the  $y$ - $z$  plane. A complete contour is swept out by repeating this process while iterating over  $y$  and holding  $x$  fixed. Finally a complete set of contours describing the target surface are drawn by iterating over  $x$ . Portions of contours which should be visually obscured by preceding contours are omitted to heighten the image's 3-dimensional effect.

The correspondence between an elliptical cross section and profile function is depicted in Figure 23. The look angle is in the  $x$ - $y$  plane with  $\phi=45^\circ$ . An ellipse perpendicular to the look angle and passing through the point  $p$  is shown. The ellipse has area  $a$  which is also the value of the profile function at the corresponding point along the look angle axis. Therefore the point  $p$  lies precisely on the target's surface. A surface contour containing  $p$  is also indicated. When several

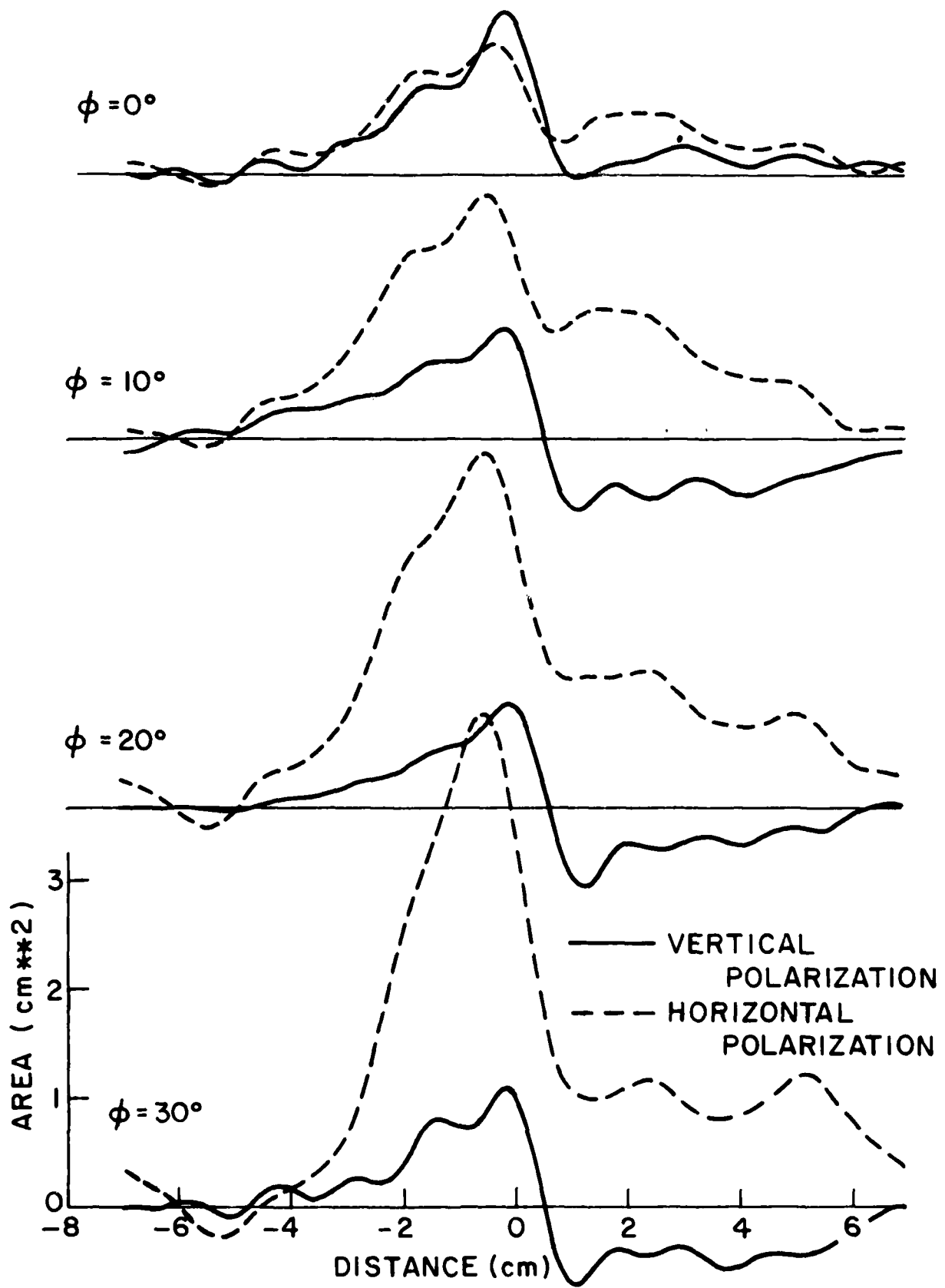


Figure 21. Horizontal and vertical polarization ramp responses for target 2.

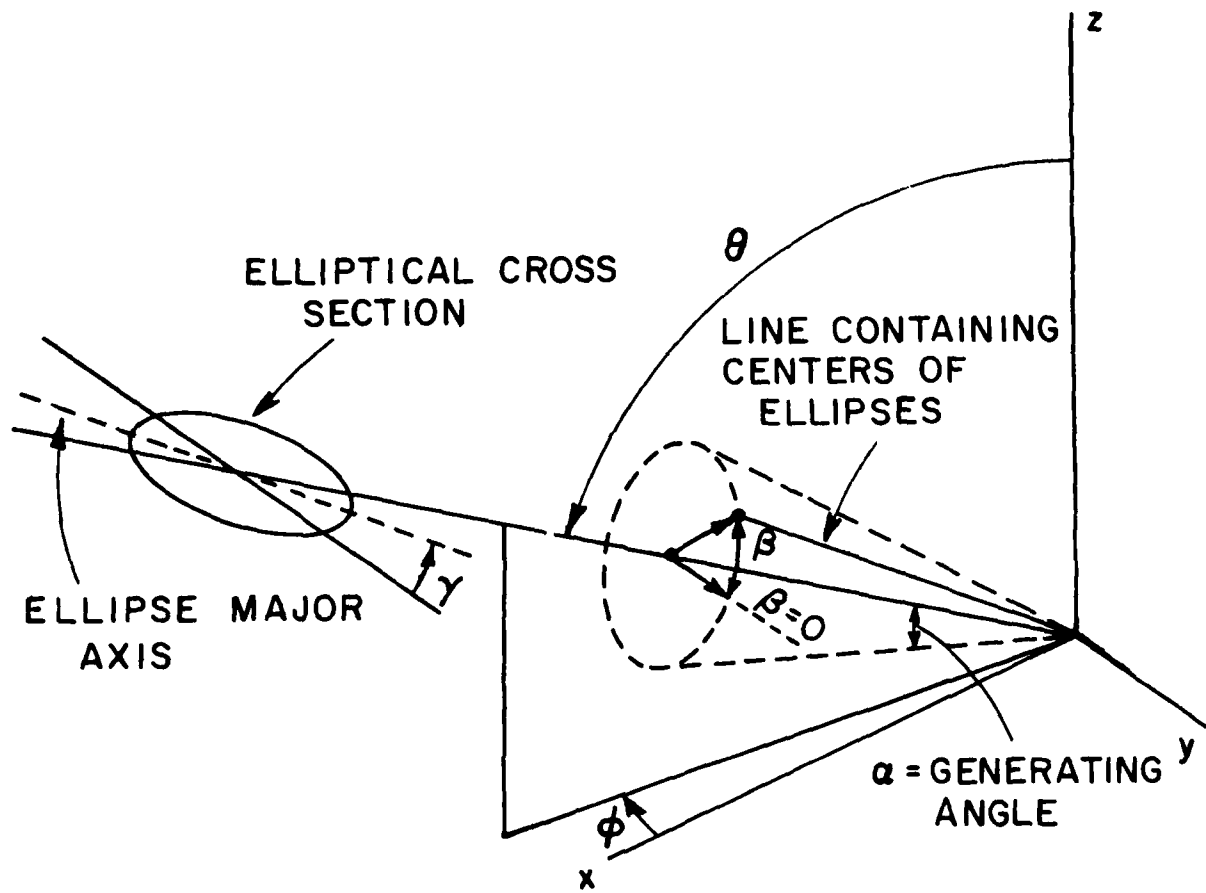


Figure 22. Specification of angles used in imaging algorithm.

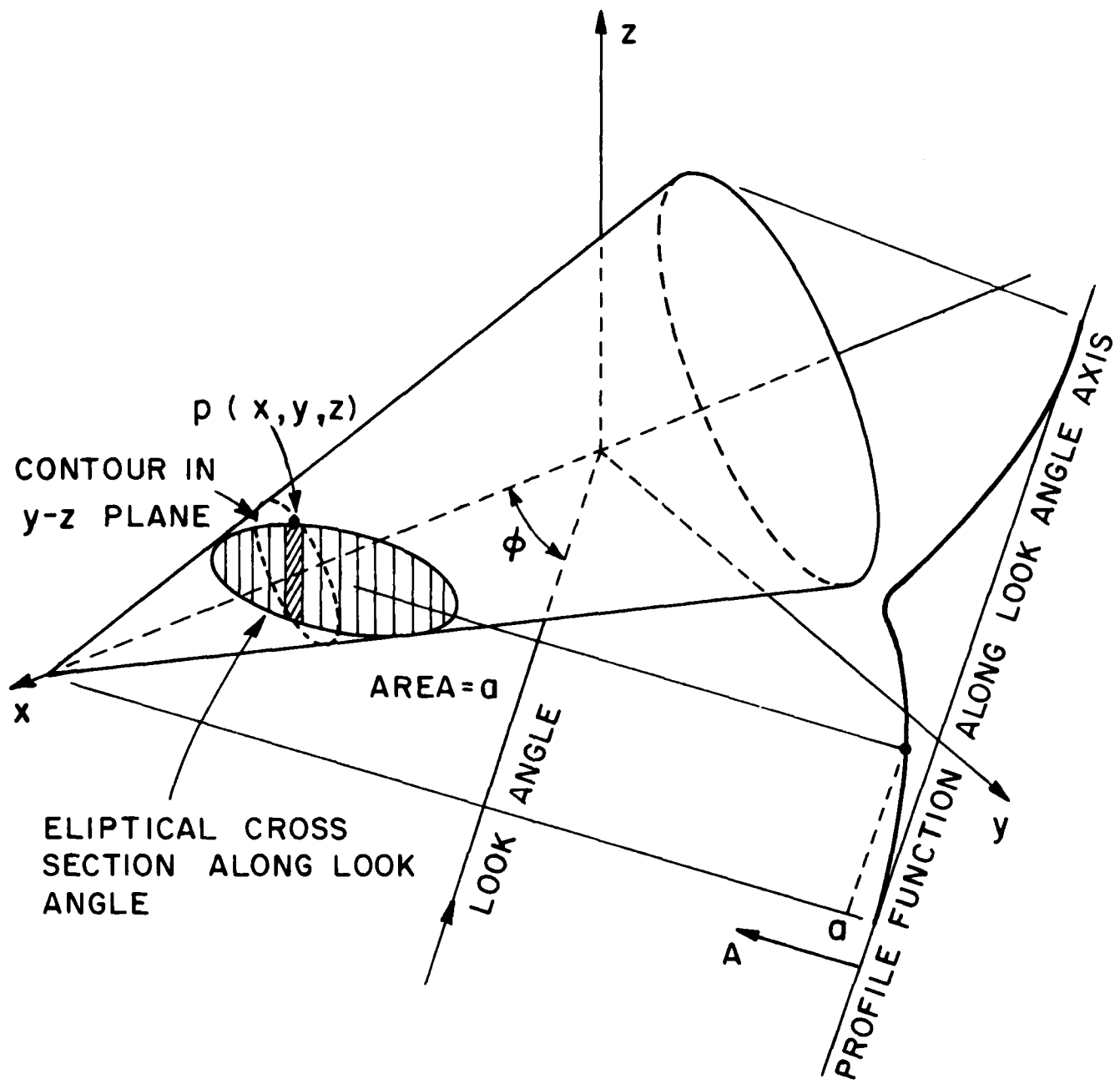


Figure 23. Illustration of imaging algorithm.

look angles are used, the final result is the same as if a separate image were calculated for each look angle and their intersection taken as the actual image.

One method of determining image quality would be a visual comparison of an image to it's corresponding target. However a more objective measure is the volume error between the input and output profile functions. Volume error is defined as:

$$\epsilon_{vol.} = \frac{\int_{-\infty}^{\infty} |A_{in}(x) - A_{out}(x)| dx}{\int_{-\infty}^{\infty} A_{in}(x) dx} \quad (11)$$

where  $A_{in}(x)$  is the ramp response or input profile function and  $A_{out}(x)$  is the output profile function for the image along a given look angle. The volume error is calculated for each look angle and the average is used as a basis for comparing image quality.

Volume error is strongly influenced by the specification of limiting surface parameters when more than one look angle is used. When these parameters are not correct the profile functions for the various look angles do not agree. The result is that portions of the target are cut off in the image and the entire image is distorted. However when only one look angle is used there are no other profile functions to agree with, and the volume error becomes virtually independent of the limiting surface parameters. Since the algorithm essentially calculates elliptical cross sections whose areas correspond to specific points on the input profile functions it would seem that there should be perfect agreement between input and output profile functions in this case. However a secondary source of volume error becomes apparent. Due to the discrete nature of the image surface and hence the image cross sections, quantization error is introduced into the output profile function. Strictly speaking, quantization error should have zero rms value. However because of the way in which the limiting surface algorithm operates, the output profile function is always less than the input ramp response. The quantization error therefore has a negative bias. Figure 24 depicts this quantization error. The input and output profile functions for an image of target 2 using a 0 degree look angle are shown. Quantization error in the output profile is evident. The volume error is 0.11. This indicates that for several look angles, even if all parameters were known and the target had elliptical cross sections throughout it's entire volume from all look angles, such as an ellipsoid, volume errors less than the order of 0.1 could not be expected.

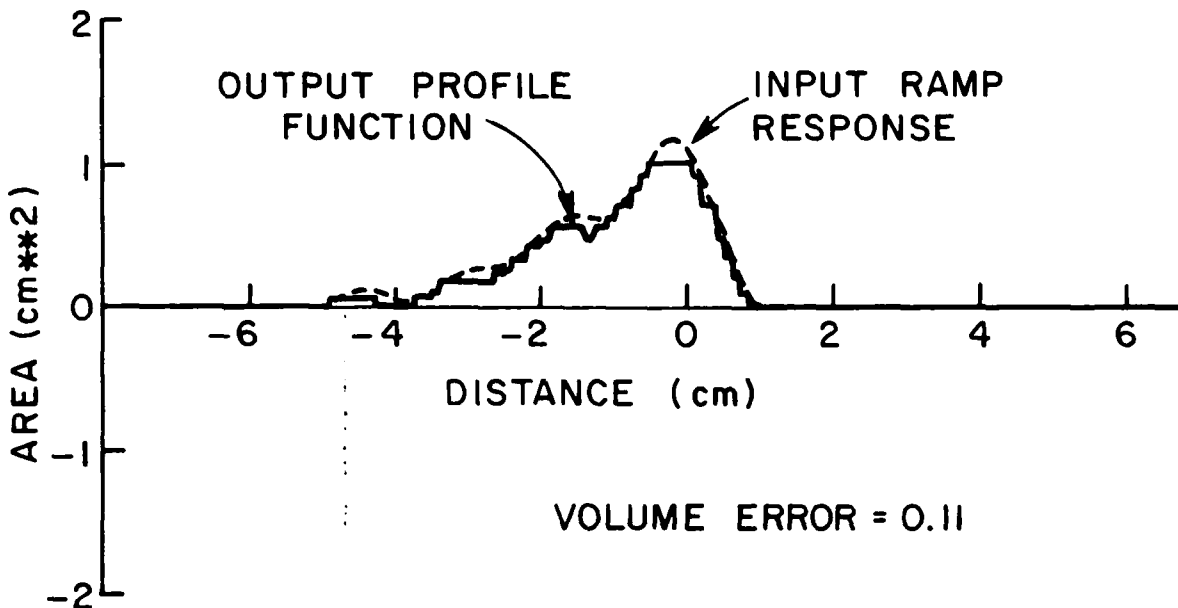


Figure 24. Example of imaging quantization error.

#### E. Limiting Surface Parameters for Conical Shapes

For general targets that are not comprised of a few simple shapes, the calculation of the limiting surface parameters discussed earlier is not possible. At best they can be only roughly approximated. However for the class of targets in this study, i.e., conical shapes, the parameters can be closely approximated. This is because the cone cross sections are ellipses along a limited range of look angles. If  $\psi$  is the generating angle of an infinite cone and  $\phi$  is the look angle from the tip of the cone with respect to the cone's axis of symmetry, then the cross section perpendicular to the look angle will be an ellipse providing  $0 < |\phi| < 90^\circ - \psi$ . For  $\theta = 0$  the cross section will be a circle. This look angle constraint is satisfied in each of our cases. However since our cones are finite, the elliptical cross sections at the back of the cones are partially truncated. The calculated parameters will agree precisely at the tip of the cone but will cause a certain amount of distortion near the base.

The eccentricity,  $e$ , of an ellipse indicates its degree of departure from circularity. Eccentricity varies between 0 for a circle and 1 for a straight line. For an elliptical conic section, eccentricity can be expressed as [14],

$$e = \frac{\cos(90-\phi)}{\cos\psi} . \quad (12)$$

However eccentricity can also be expressed in terms of the ellipse's major axis half length  $a$ , and the distance,  $c$ , from the ellipse's center to one of the foci,

$$e = \frac{c}{a} . \quad (13)$$

A third relation relating  $a$ ,  $c$ , and the ellipse's minor axis half length,  $b$ , is,

$$c^2 = a^2 - b^2 . \quad (14)$$

Combining Equations (12), (13), and (14) above we have,

$$\frac{a}{b} = \left[ 1 - \left( \frac{\cos(90-\phi)}{\cos\psi} \right)^2 \right]^{-1/2} \quad (15)$$

where  $\frac{a}{b}$  is the aspect ratio for the ellipse. For target 2,  $\psi$  is  $6^\circ$ . The aspect ratios for the various look angles are shown in Table III-2

TABLE III-2  
ELLIPTICAL CROSS-SECTION ASPECT RATIOS VS.  
LOOK ANGLE FOR TARGET 2

LOOK ANGLE $\phi$	ASPECT RATIO $a/b$
$0^\circ$	1.0
$10^\circ$	1.02
$20^\circ$	1.06
$30^\circ$	1.16

The line containing the center of the elliptical cross sections is shown in Figure 25. For the range of  $\phi$ 's and  $\psi$ 's that we are interested

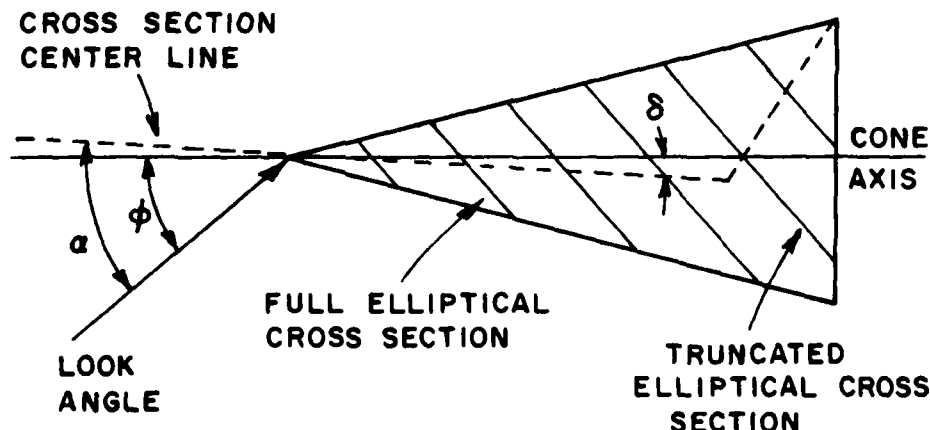


Figure 25. Location of elliptical cross sections for a cone.

in, the angle  $\delta$  between the center line and the cone's axis of symmetry is very small. Therefore  $\alpha$  is approximately the same as the look angle. Due to the orientation of the target along the  $x$  axis and the fact that the look angles all lie in the  $x$ - $y$  plane,  $\beta=180^\circ$  and  $\gamma=0^\circ$  in all cases.

Figure 26 is an image of target 2 using the 0 and 30 degree look

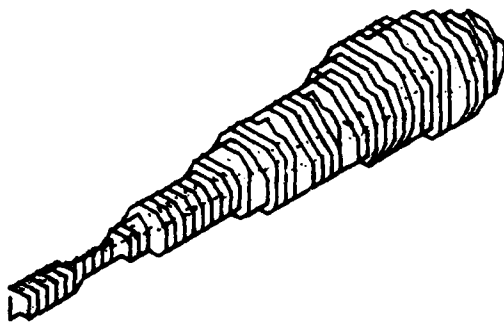


Figure 26. Image of Target 2 generated from ramp responses from  $0^\circ$  and  $30^\circ$  look angles with optimum parameters.

angle profile functions from Figure 19. The undulation in the surface is due to the ripple in the profile functions resulting from the 10 harmonic ramp response approximation. Distortion can be seen near the base of the image due to the truncated elliptical cross sections of the cone along the  $30^\circ$  look angle. Figure 27 shows the comparison of the input and

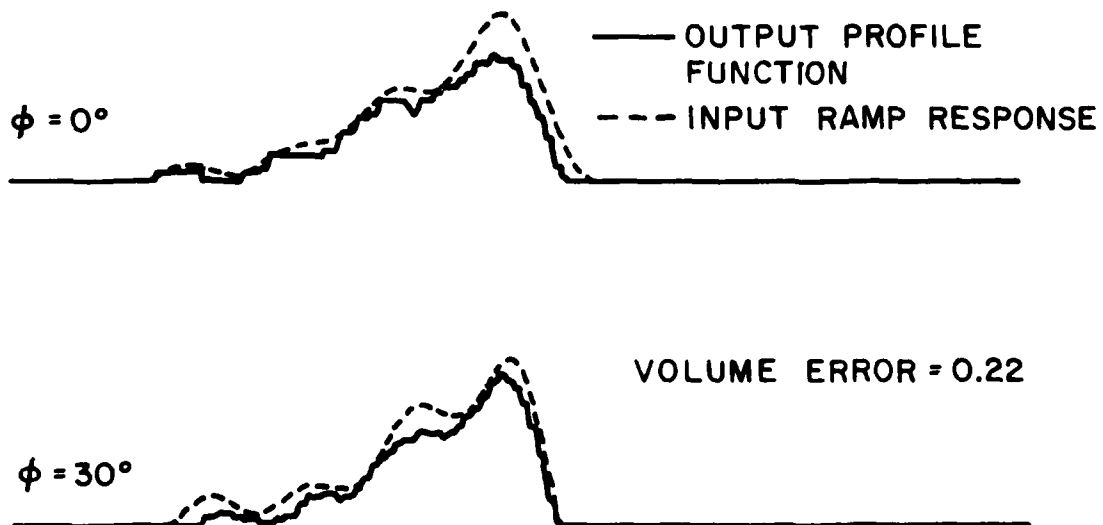


Figure 27. Input and output profile functions for image in Figure 15.

output profile functions for the image. The back end of the output profile function along the zero degree look angle is seen to be significantly cut off in comparison with the input profile function

Some images generated for the other targets are shown in Figures 28 through 32. Each of these images was generated using the  $0^\circ$  look angle (nose-on) ramp response waveform. The volume error estimate is shown along with the image. In general, all images have those features just discussed in the case of target 2.

#### F. Imaging Dependence on Limiting Surface Parameters

As was pointed out earlier, the limiting surface parameters for a given target are initially unknown. However to obtain an accurate image they must be correctly determined. One possible approach would be to try various combinations based upon reasonable guesses until a suitable image resulted. This approach is not satisfactory for unknown targets. An alternative is to study the agreement between an image and its input profile functions. The volume error is a convenient measure of this agreement. The volume error can be observed as a function of one or more limiting surface parameters. The goal will be to obtain quantitative information on the relation between volume error and the limiting surface parameters.

To investigate this relationship, images were generated using the  $0$  and  $30$  degree look angle profile functions for target 2. These are shown in Figure 19. In each case correct values of parameters for the  $0$  degree look angle limiting surface were used. Parameters for the  $30^\circ$  look angle limiting surface were iterated one at a time while setting the others at their correct values. For the  $0$  degree look angle the parameters are;  $\alpha=0$ ,  $\beta=0$ ,  $\gamma=0$  and aspect ratio =  $1.0$ . For the  $30$  degree look angle  $\alpha=30^\circ$ ,  $\beta=180^\circ$ ,  $\gamma=0^\circ$  and aspect ratio =  $1.16$ . Figure 33 shows the variation in volume error as  $\alpha$  varies from  $27$  to  $36$  degrees. The minimum error is  $0.215$  and occurs at  $\alpha=30$  degrees. Figure 34 demonstrates how volume error is introduced by incorrect values of  $\alpha$ . Outlines of images generated independently from  $0$  and  $30^\circ$  profile functions are shown. With  $\alpha=30^\circ$  the images are properly aligned. A second case is shown with  $\alpha=45^\circ$ . Since the composite image is the intersection of the two independent images it is seen that the front of the cone will be clipped off in the image. Figure 35 is the resulting image and may be compared with Figure 26. The volume error is  $0.55$ . The profile functions for the misaligned case are shown in Figure 36. Figure 37 shows the variation in volume error with aspect ratio. The aspect ratio is incremented from  $0.25$  to  $3$  with a minimum volume error of  $0.218$  occurring at  $1.125$  which is very close to the calculated value of  $1.16$ . Figure 38 is a plot of volume error versus  $\gamma$ . The curve is symmetric about  $\gamma=0^\circ$  so only the range from  $0^\circ$  to  $90^\circ$  is shown. The volume error is a minimum of  $0.215$  at  $\gamma=0^\circ$ . The volume error tends to decrease as  $\gamma$  approaches zero although the curve does not decrease monotonically. It should be noted however that the fluctuations or ripples in the curve are comparatively small, less than  $0.01$  and the entire range of volume error is much less than that seen with the other parameters.



Figure 28. Image of target 1, generated from ramp responses at  $0^\circ$  and  $30^\circ$  look angles.

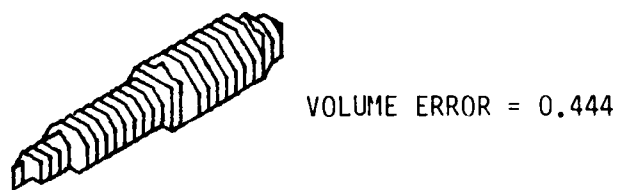


Figure 29. Image of target 3, generated from ramp responses at  $0^\circ$  and  $30^\circ$  look angles.

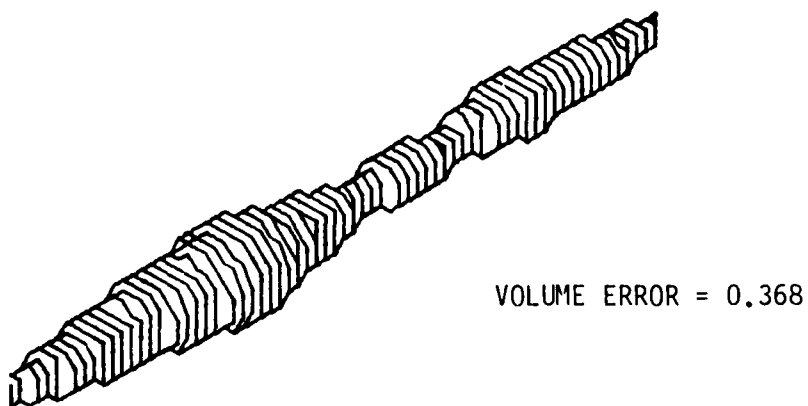


Figure 30. Image of target 4, generated from ramp responses at  $0^\circ$  and  $30^\circ$  look angles.

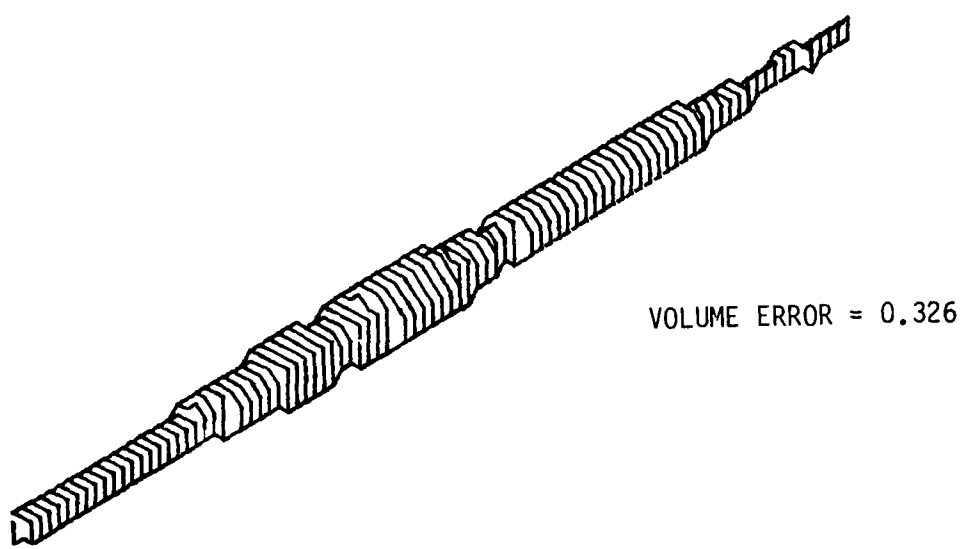


Figure 31. Image of target 5, generated from ramp responses  
0° and 30° look angles.

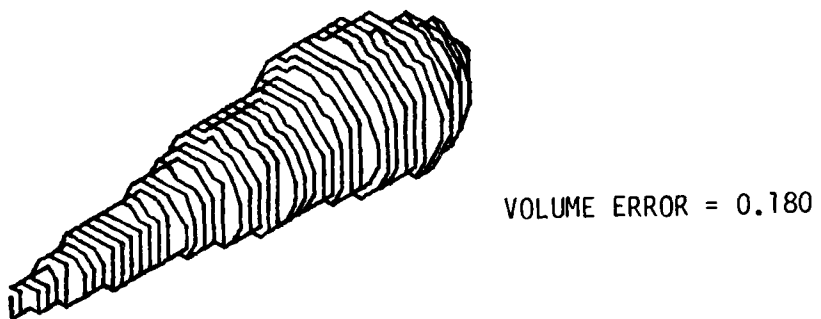


Figure 32. Image of target 6, generated from ramp responses  
0° and 30° look angles.

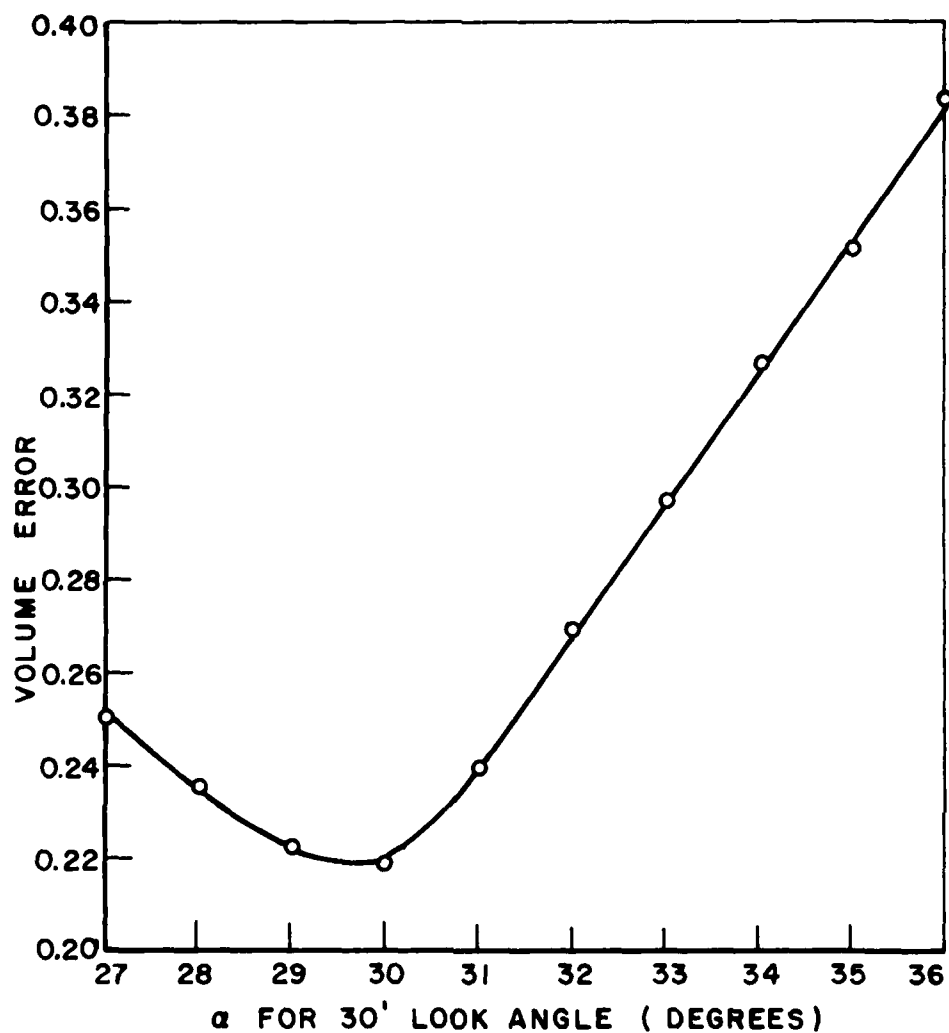
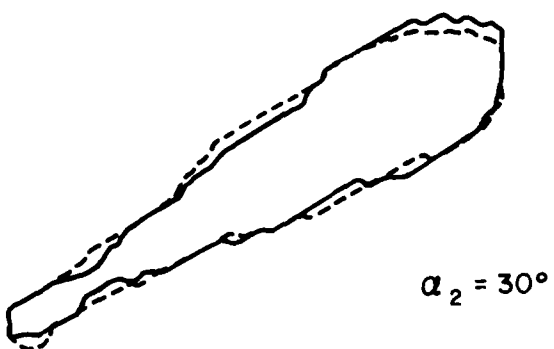


Figure 33. Average volume error versus  $\alpha$ .



— IMAGE GENERATED FROM  $0^\circ$  LOOK ANGLE  
- - - IMAGE GENERATED FROM  $30^\circ$  LOOK ANGLE

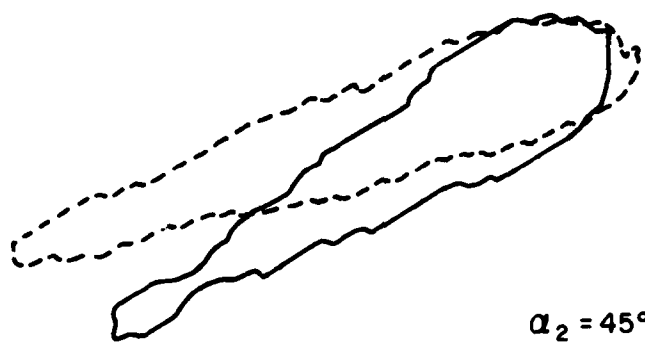


Figure 34. Example of imaging dependence on  $\alpha$ .

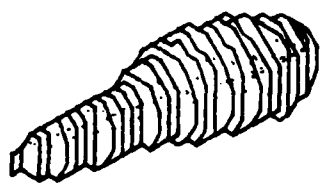


Figure 35. Image of target 2 generated from ramp responses from  $0^\circ$  and  $30^\circ$  look angles with  $\alpha=45^\circ$  along  $30^\circ$  look angle.

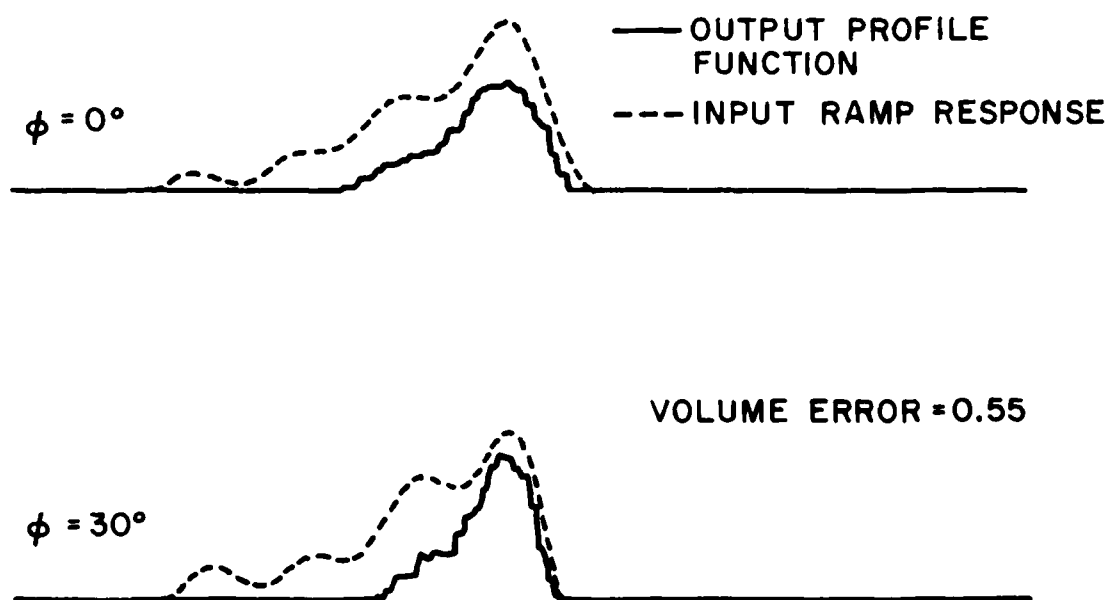


Figure 36. Input and output profile functions for image in Figure 35.

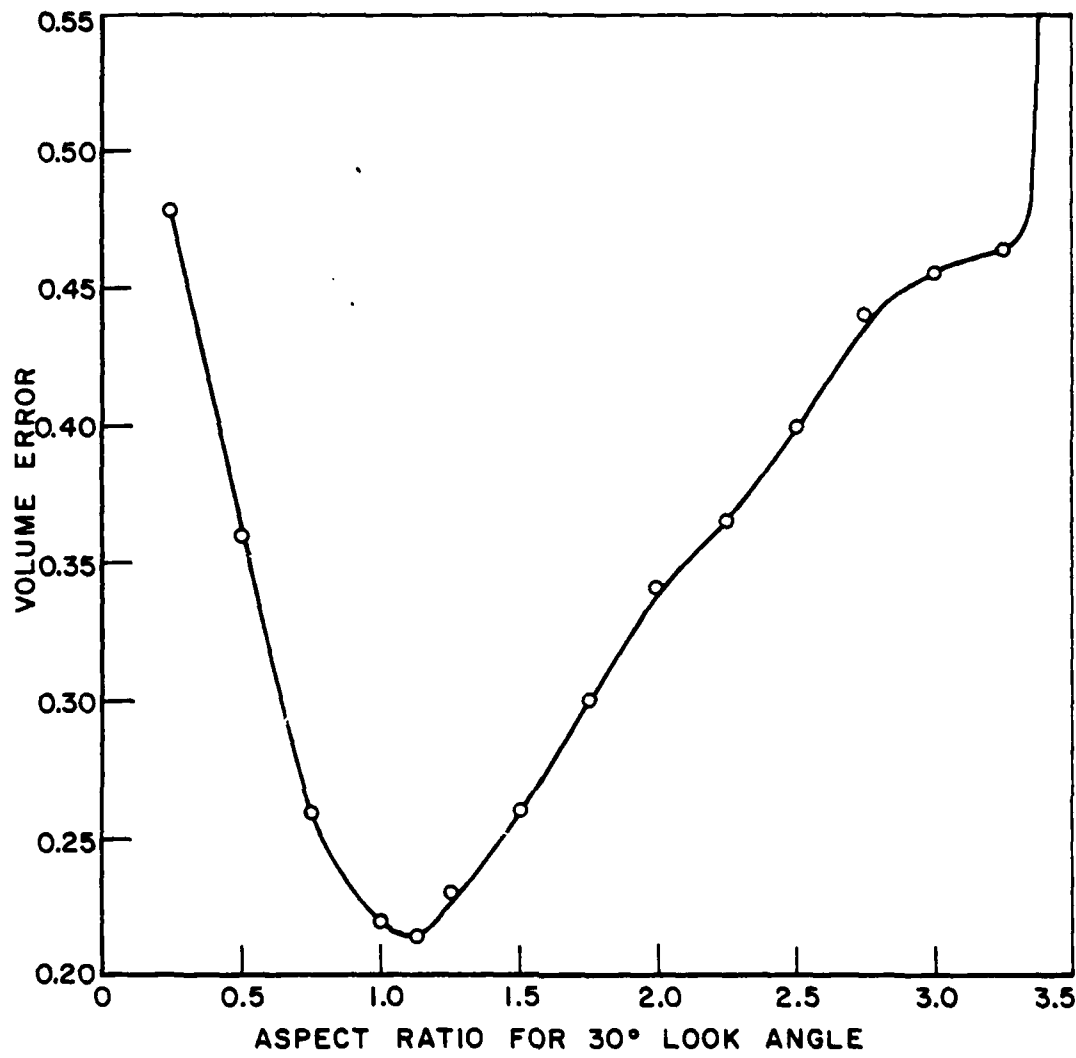


Figure 37. Volume error versus aspect ratio.

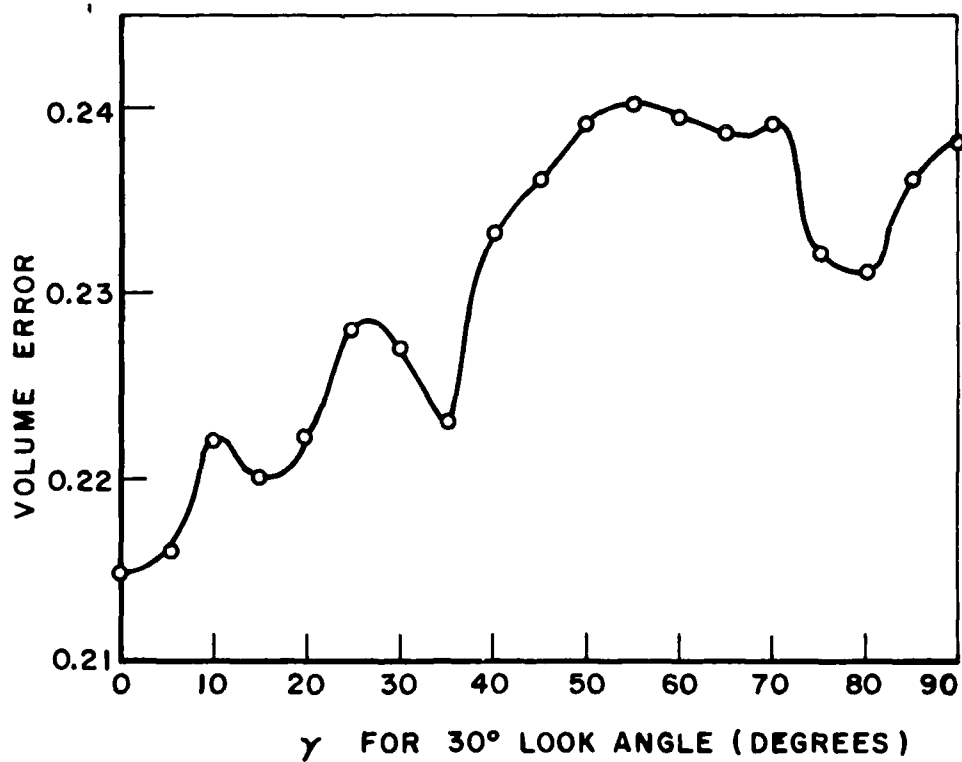


Figure 38. Volume error versus  $\gamma$ .

With each of the three parameters studied the volume error was minimized as the correct parameter value was reached. In two of the cases the volume error decreased monotonically towards the minimum point while in the third case there was a trend towards decreasing error although some ripple was present. This suggests that an automated iterative technique which seeks to minimize volume error using a standard approach like Newton's method may be appropriate for determining the unknown parameters. However, volume error dependence on the limiting surface parameters must be studied in greater depth before this is attempted. In particular volume error must be observed as several parameters stray from their optimum values. This will be the focus of the limiting surface imaging study in the near future.

#### G. A Possible Approach for the Study of Image Confidence

Image quality has been studied by comparing input profile functions to the image profile functions. However this may not be a complete measure of the correspondence between a target and it's resulting image. The question that remains is whether or not a set of profile functions uniquely define a target. To study this problem a two dimensional example will be used.

For one look angle an infinite number of objects can be found to satisfy a given profile function. This can be demonstrated by slicing an object perpendicular to a look angle. The object may be modified by displacing the slices perpendicular to the look angle in any arbitrary fashion. An example is shown in Figure 39. The profile function along the look angle remains unchanged.

The problem is constrained when a second look angle is added. It must be determined if it is possible to displace the slices along one look angle in such a way as to maintain the original profile function along a second look angle as well. The object considered will be a rectangle. The radar resolution will be assumed to be  $t$ . The slices will therefore have thickness  $t$  and only displacements of multiples of  $t$  will be allowed. A rectangle sliced along an off axis look angle is shown in Figure 40. For  $t > w \sin\phi$ , where  $w$  is the rectangle width and  $\phi$  is the look angle from the  $x$  axis, each slice will have 3 distinct regions as seen along the  $x$  axis. Assuming the back tip of the slice to be at  $x=0$ , the cross sectional area versus  $x$  for the slice is:

$$A(x) = \begin{cases} x/\tan\phi & 0 < x < t/\cos\phi \\ t/\sin\phi & t/\cos\phi < x < wtan\phi \\ \frac{t}{\sin\phi} - \frac{(x-w\tan\phi)}{\tan\phi} & wtan\phi < x < wtan\phi + \frac{t}{\cos\phi} \\ 0 & \text{otherwise} \end{cases} \quad (16)$$

$A(x)$  is plotted in Figure 41.

In order to avoid having slices scattered throughout all of space we will require that some part of each slice at least touch the original volume of the rectangle. The maximum displacement of slices perpendicular to the look angle axis determines how many slices ahead one must look for area contribution at a given point along the  $x$  axis. For example in Figure 42 it is seen that point 1 on the  $x$  axis may receive an area contribution from any slice along the look angle axis up to slice 6. The area contribution at a given point on the  $x$  axis due to a slice along the look angle axis depends on the actual amount by which the slice has been displaced. Assume slice  $j$  along the look angle axis is displaced by  $nt$ . The distance from the tip of the slice to point  $i$  along the  $x$  axis is  $jtcos\phi - nt \sin\phi - t(i-1/2)$ . This distance is then inserted into the formula for  $A(x)$  above as  $x$ .  $A(x)$  for each contributing slice must be found for a given point on the  $x$  axis. At each point, one must look ahead by a number of slices equal to the next highest integer value of  $2wtan\phi/t \cos\phi = N$ .

The general form of the area at each point will be  $a_i = \sum_{j=i}^{i+N-1} A_{ij}(x)$  where

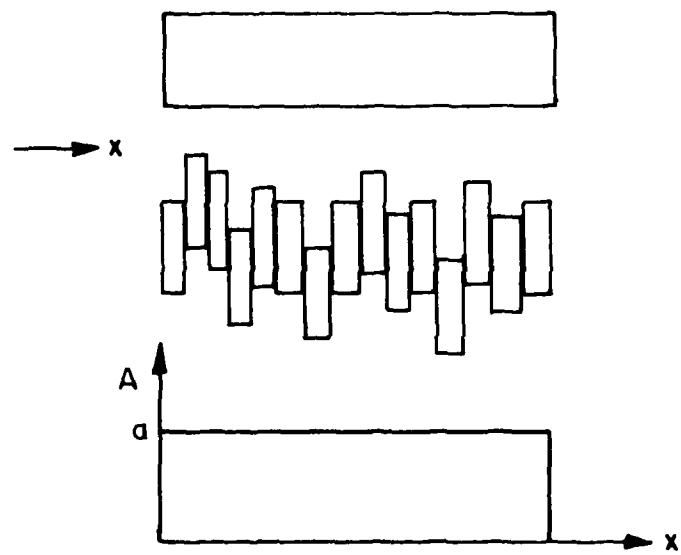


Figure 39. Profile function for a rectangular solid, before and after modification.

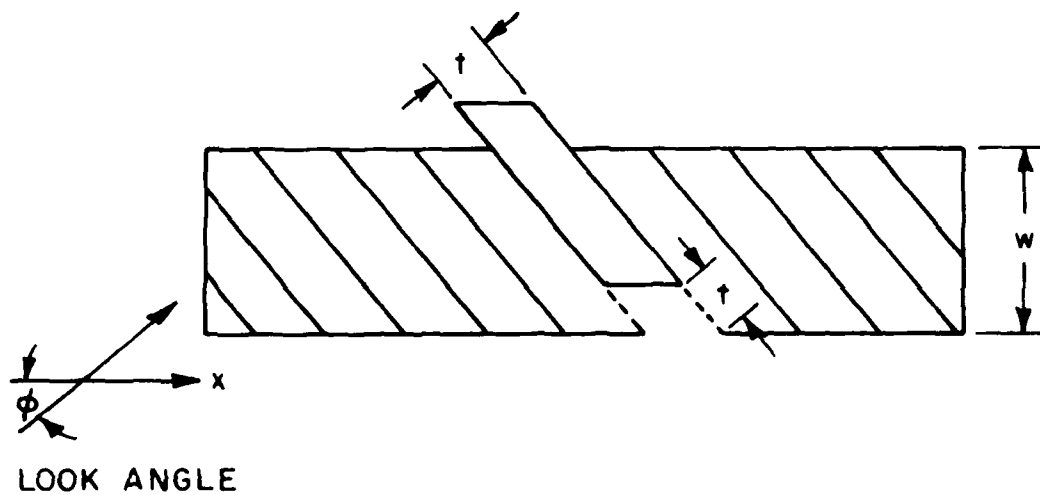


Figure 40. Rectangle sliced perpendicular to look angle with one slice displaced.

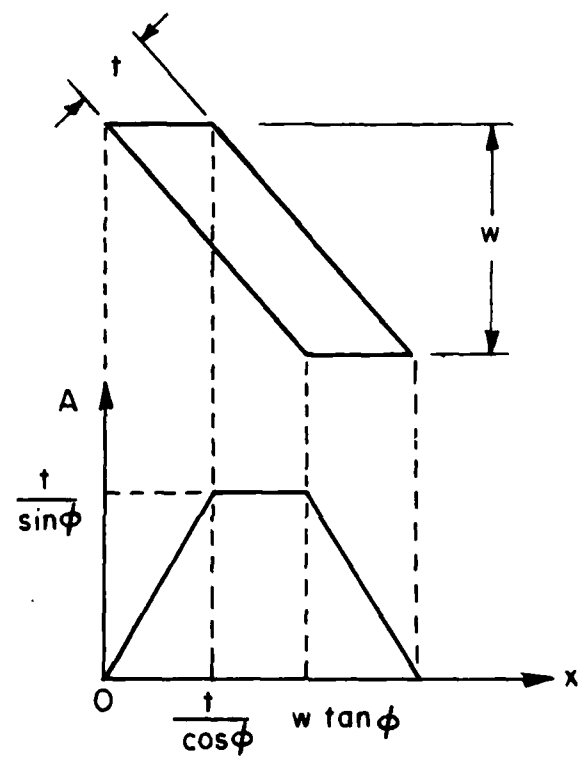


Figure 41. Cross sectional area versus distance for a slice with unit thickness.

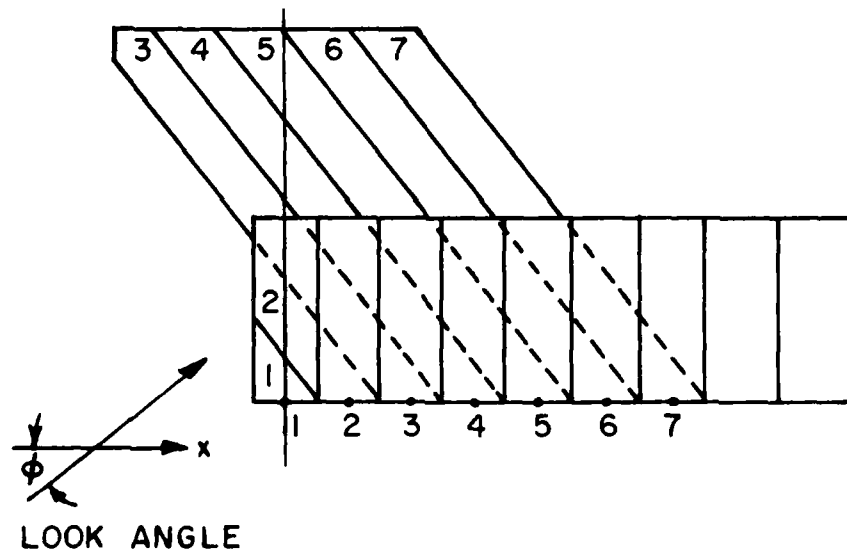


Figure 42. Area contribution at point 1 along 7 direction due to slices 1-6 along look angle direction.

$A_{ij}(x)$  is the area contribution of slice  $j$  at point  $i$  along the  $x$  axis. If the rectangle has  $m$  slices along the  $x$  axis then there will be  $m$  such equations. The problem is to solve these equations for the combinations of displacements which yield the same  $a_i$  as the original rectangle. Unfortunately, due to the form of  $A(x)$  for each slice, the relationship between the  $a_i$  and the slice displacements is non-linear and a closed form solution is not apparent. However one observation can be made. As the number of look angles increase the problem becomes more constrained and the probability of several objects satisfying the same set of profile functions decreases.

#### IV. HIGH FREQUENCY IMAGING USING THE BOJARSKI IDENTITY

##### A. Introduction

As we indicated in the proposal for our present research, we would endeavor to study techniques to produce target images based on the backscatter data. Numerous researchers have reported in this field for years with several approaches to the same basic problem; that of relating the backscatter to the phenomena that gives rise to the fields and thereby determine a satisfactory image. As is often the case each approach is based on fundamental assumptions about the shape of the body, material properties of the body and the frequency range of the interrogating signal.

In our contribution we have utilized the Bojarski identity [15] which is valid in the physical optics limit, i.e., that the currents induced on the body are  $2\pi x H$ .

In Section IV-B we will introduce the Bojarski identity.

In Sections IV-C through IV-E we will generate data for trial of the identity. First a one dimensional characteristic function with the effects of a one dimensional bandpass filter to simulate the frequency constraint of a radar system at one aspect, then two dimensional characteristic functions are generated for triangular, square and circular shapes and the corresponding spectrum is windowed in aspect and in frequency to see the resulting distortion in the characteristic function space. These results will not only give us a "feel" for the images to expect with finite backscatter data but they also demonstrate the Gibbs distortion due to the window itself and through the proper use of spectral tapering these effects can be minimized.

Next, in Section IV-F a study is made of the possibility of extending the frequency-aspect window in order to improve the images. Specific attention is given to observing the nature of the angular variations of the scatter to analytically extend the window or to determine which features are of greater significance.

Finally suggestions are made for further study and insights in image improvement are discussed.

### B. The Bojarski Identity

In a series of reports Norbert Bojarski [15,16,17,18,19] has formulated a relationship between the monostatic scattered far field cross section of perfect conductors and the geometry of the conductors. The results are based on the physical optics approximation.

If the scatterer is expressed in three dimensions by its characteristic function  $\gamma(\bar{x})$  where,

$$\gamma(\bar{x}) = \begin{cases} 1 & \text{inside the body} \\ 0 & \text{outside the body} \end{cases} \quad (17)$$

and if the scattered far field cross section  $\rho(\bar{p})$  is used to define  $\Gamma(\bar{p})$  where,

$$\Gamma(\bar{p}) = \sqrt{4\pi} \frac{\rho(\bar{p}) + \rho^*(-\bar{p})}{|\bar{p}|^2} \quad (18)$$

with  $\rho(\bar{p})$  = the field cross section

$$\bar{p} = \frac{2\omega}{c} \bar{a} = 2\bar{k} \left( \frac{\text{cycles}}{\text{meter}} \right)$$

$\bar{k}$  = wavenumber propagation vector in the direction of aspect;

then Bojarski has shown that

$$\gamma(\bar{x}) = \frac{1}{(2\pi)^3} \int_{-\infty}^{\infty} \Gamma(\bar{p}) e^{i\bar{p} \cdot \bar{x}} d^3\bar{x} \quad (19)$$

which is just a 3-dimensional inverse Fourier transform of  $\Gamma(\bar{p})$ .

### C. Trial Results

At the outset this identity suggests that we need  $\Gamma(\bar{p})$  to be measured at all frequencies and aspects to exactly reconstruct  $\gamma(\bar{x})$  and thus the target. But there are many factors that do not necessitate knowledge of the complete backscatter spectrum [20,21,22]. This is seen to be true in mathematically related fields where, e.g., intelligible communication signals can be heavily bandlimited and yet the information can be satisfactorily recovered within some tolerable level.

#### D. One Dimension

Whenever a function's spectral components are bandlimited, often termed windowing, then the inverse transform of the windowed spectrum will produce a likeness of the original function. Certain features will be preserved depending on what portion of the infinite spectrum is windowed. In the practical radar sense only a finite frequency band is used thus it is instructive to see the distortion introduced in the corresponding characteristic function. Figure 43 shows a one aspect characteristic function (where  $\gamma(x)$  represents the linear extent of the target along that aspect), its unwindowed and windowed spectrum, and the resulting image after windowing. It can be seen that impulses occur at the discontinuities. Thus the scatterer's front and back edge could still be determined. The advantages of the preserved edges are twofold; first, we must rely on this result in bandlimited radar systems and secondly, the low frequency components in real systems do not obey the physical optics approximation so we could not use them with extreme accuracy anyway. And if we can determine edges in 3-dimensions, i.e., the surface of the scatterer, then we have exactly specified the shape.

#### E. Two Dimensions

We have elected to study the application of Bojarski's identity in two dimensions because of the relative ease of display and we can infer results to the three dimensional case.

The method of display of the two dimensional function is a gray level plot. Each array of values in either  $x$  or  $p$  space is quantized into 14 levels and each level is assigned a gray density in the form of overstriking characters on the line printer. (A blank for level 1, ..., and the characters U,T,X,\$ overstruck for level 14.) Additionally the array is interpolated in the  $Y$  dimension to expand the display so that  $N \times N$  point arrays appear square visually.

#### Evaluation of triangular, square and circular characteristic functions

In this section we demonstrate the results of applying the identity to three shapes. An equilateral triangle is shown in Figure 44a. The  $y$  axis dimension is 11 spatial samples high and the  $x$  axis dimension is 21 spatial samples wide. The actual dimensions are omitted because the examples demonstrate principles and are not intended for a specific application. (Recall that the  $y$  axis values are interpolated by the gray level plotting routine thus more than 11 samples appear.) The "black" areas represent a magnitude of 1, otherwise, the magnitude is 0. Thus we see a "top" view of the characteristic function in a plane. The square characteristic function appears in Figure 44b and both dimensions are 11 spatial samples long. Finally a circular characteristic function appears in Figure 44c with a diameter of 11 spatial samples. After application of a two-dimensional FFT the magnitude of the spectra for all three shapes appears in Figures 45, 46 and 47.

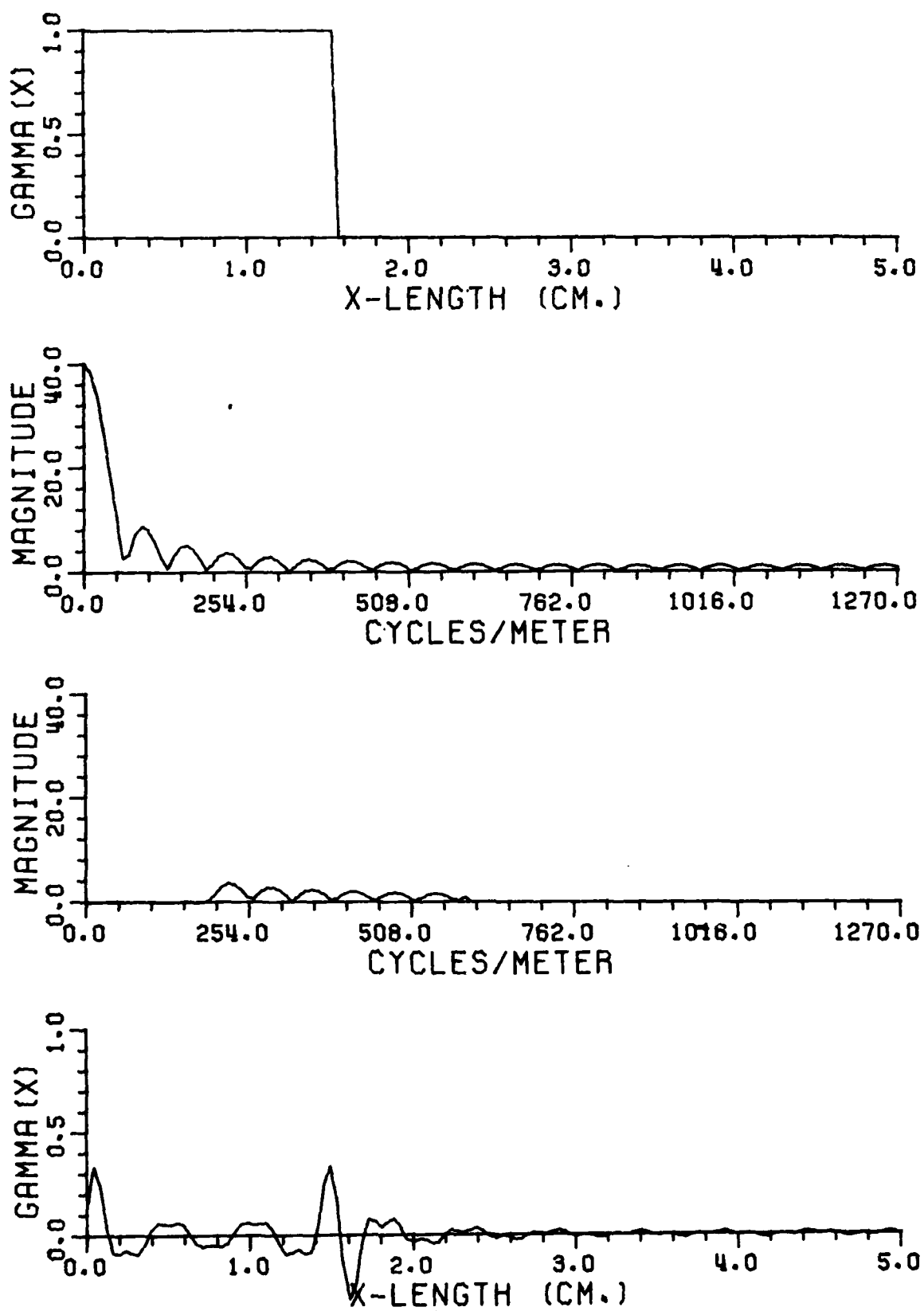


Figure 43. Display of a one dimensional characteristic function, the spectrum before and after windowing and the subsequent image.

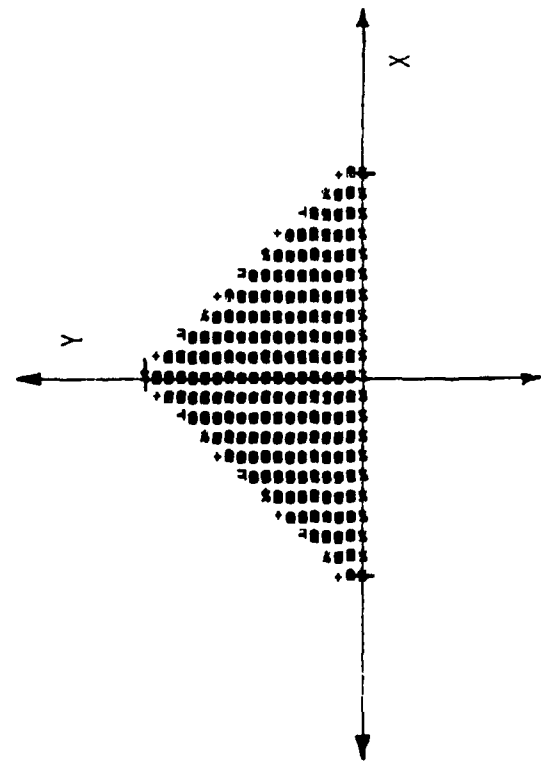


Figure 44a. Characteristic function of a triangular scatterer in two dimensions.

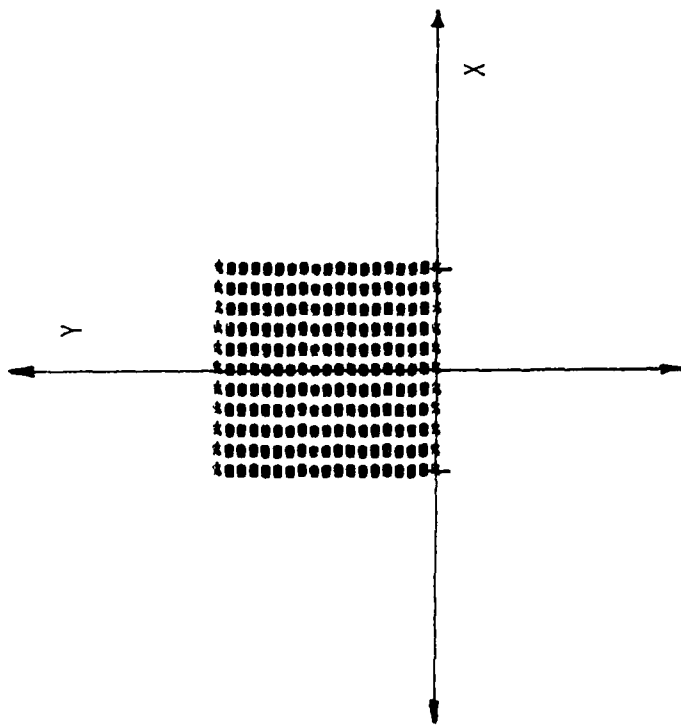


Figure 44b. Characteristic function of a square scatterer in two dimensions.

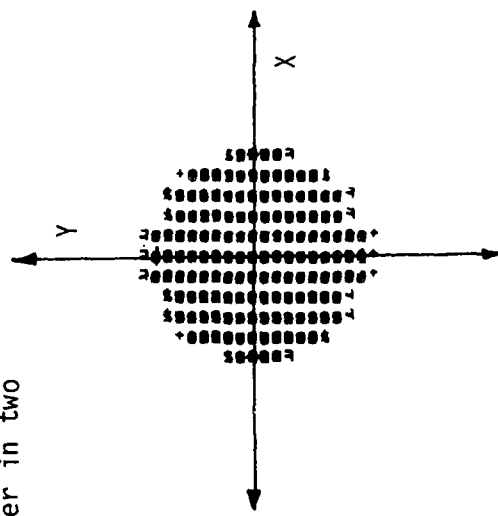


Figure 44c. Characteristic function of a circular scatterer in two dimensions.

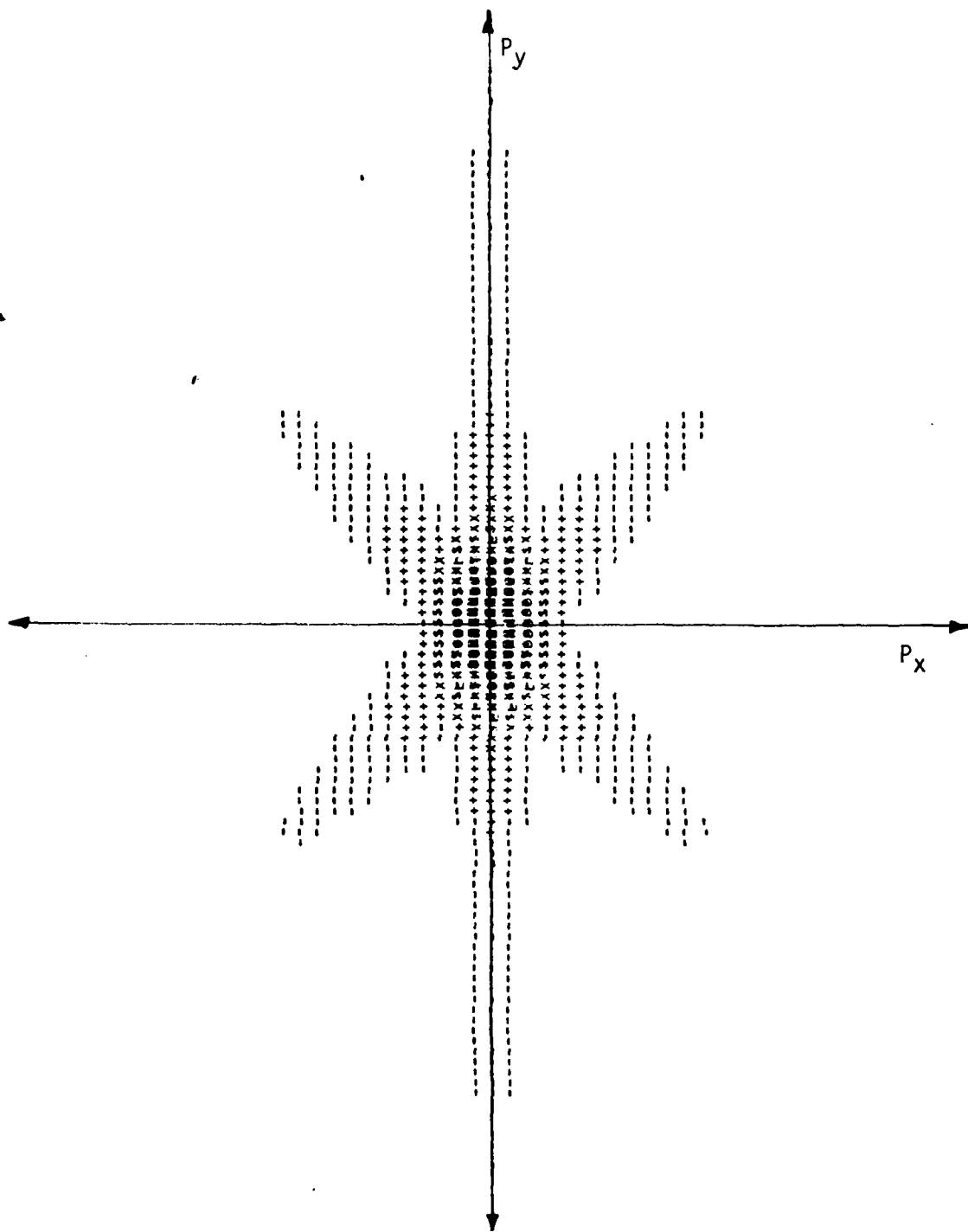


Figure 45. Two dimensional scattering from the triangular target.

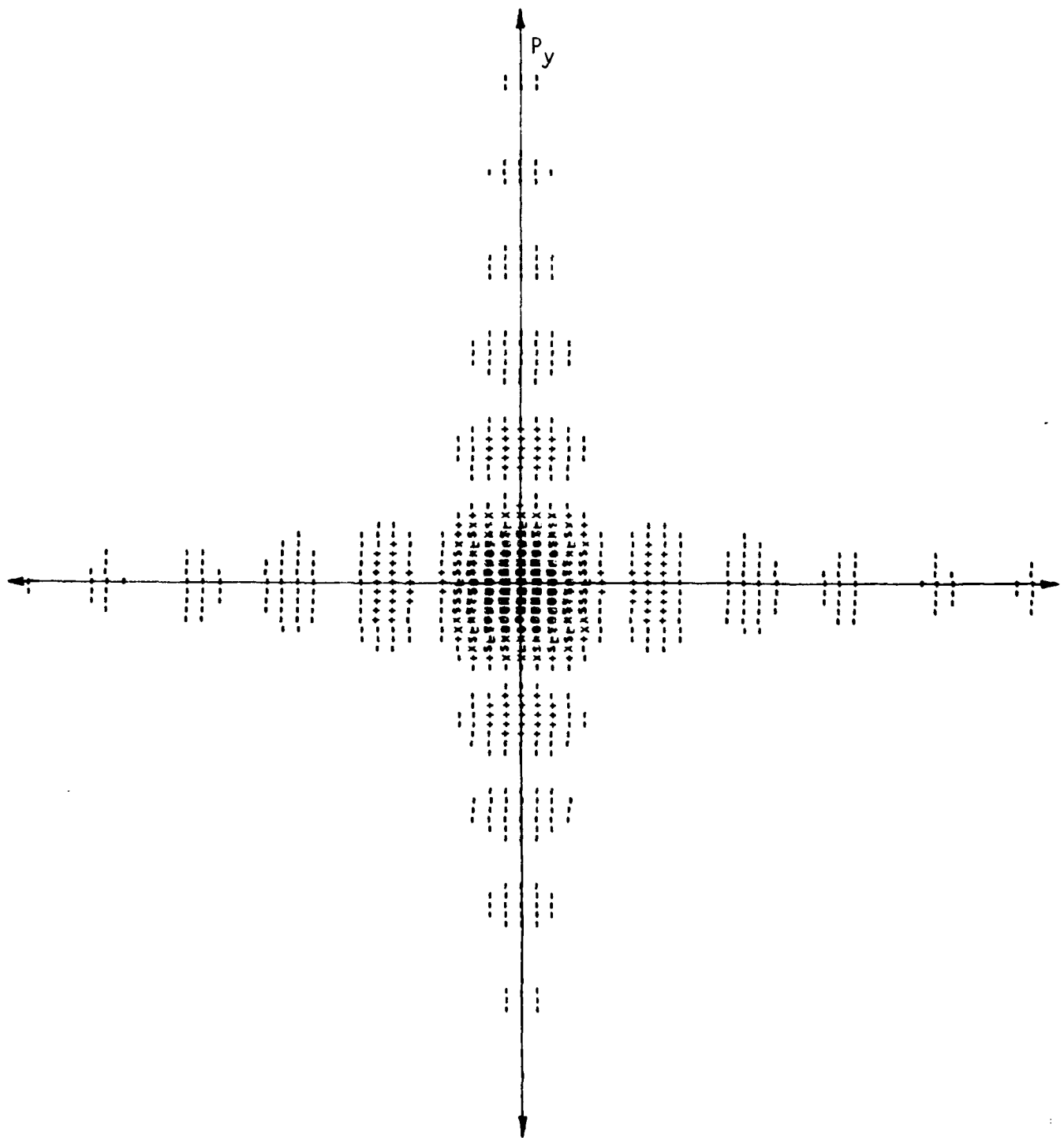


Figure 46. Two dimensional scattering from the square target.

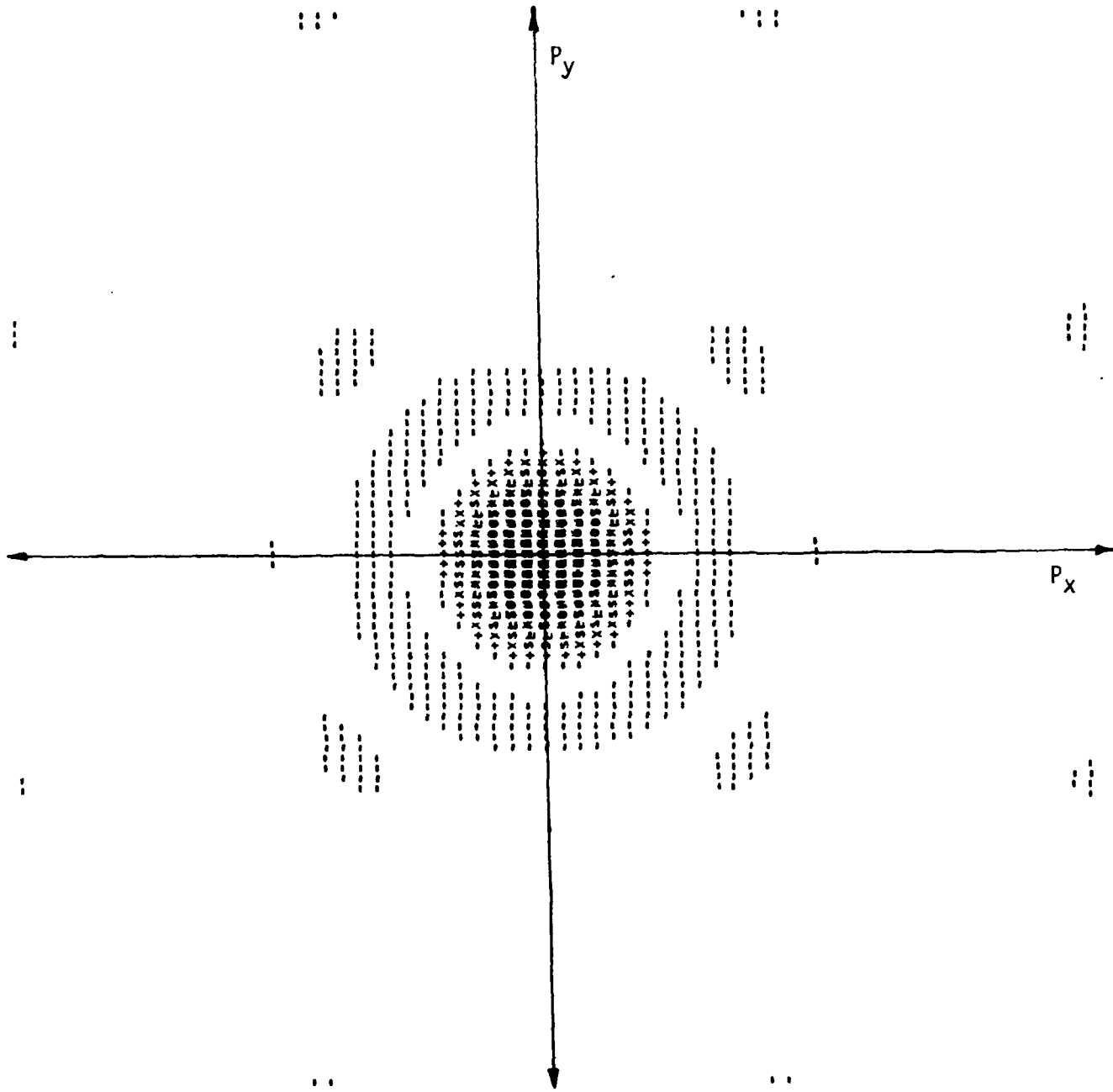


Figure 47. Two dimensional scattering from the circular target.

It is noted that the different geometries have characteristic backscatter variations. The square and triangle have large return "lobes" which are perpendicular to the straight edges. These correspond to the "speculars" in normal radar terminology. The resonances of the circle are reflected in oscillations which are radially directed and are symmetric in magnitude about the origin. Thus, the effects of degradation due to windowing will depend upon both the geometry of the scatterer and the spectral angular location of the windows. This may be reflected in two ways. One; by the law of conservation of energy, if the geometry gives rise to lobes in the spectrum then, for a given window size, varying aspect locations will produce varying amounts of energy. Thus if the window is located in the vicinity of a null less energy is available for image reconstruction than near a maximum. Secondly, lobes are perpendicular to surfaces along major dimensions and nulls are located at aspects where there are few or no corresponding perpendicular surfaces. Therefore the most significant measurements would be taken when the aspect angle of the receiver lies in the region of major lobes. This is evidenced by the test results in the next three sections.

Additionally, we know that the characteristic function in  $\bar{x}$  space is a constant (=1) within the target and has a jump discontinuity at the boundary. Thus, the gross target volume information is primarily concentrated in the low frequency backscatter and the location of surfaces (the profile) is concentrated in the higher frequencies. Therefore, if we retain only higher frequency information we may still reconstruct the surface of the scatterer for identification. This is contrary to the results of Perry's analysis [23].

In the following sections we consider the effects of finite apertures or windows on the reconstructed images.

#### Frequency windowing

Since practical radar systems operate in a band of frequencies we have simulated this by applying a frequency band window at all aspects. The basic window appears in Figure 48 and has magnitude 1 within the upper and lower cutoff and 0 in the stop band. This window is then multiplied with the scattering spectrum to simulate the measurements of a bandlimited radar. In Case I we applied a window with a lower cutoff at the 10-th sample point and the upper cutoff at the 30-th sample point. (Our spectrum is 32 points long in the positive  $P_x$  and positive  $P_y$  directions.) The resulting images, for the triangular, square and circular shapes appear in Figures 49 to 51. Since a blank represents a minimum in the gray scale plot we see that the minimum is the under shoot, due to Gibbs phenomenon, at the edge of the targets. A maximum overshoot also occurs at the edges. Therefore the boundary information is still preserved. We applied a threshold filter at a level approximately half way between the minimum and maximum values. The images are replotted in Figures 52a to 52c after the threshold is applied and we can easily distinguish each shape. Case II demonstrates similar results where we applied a filter with lower

frequency cutoff at the 15-th sample point and the upper cutoff at the 30-th sample point. The results before and after the threshold filter are seen in Figures 53 to 56c.

We have seen that the radar restriction in frequency does not eliminate the possibility of identification. In fact target images can be restored based on knowledge of the boundaries.

#### Aspect Windowing

In our application we not only are restricted in frequency but we are restricted to measurements over a finite range of aspects. Therefore we have applied a window in aspect angle, as seen in Figure 57, that is 1 within a specified angle and 0 outside and is symmetric about the origin. This rigorously corresponds to data for two aspects that are colinear and separated by  $180^\circ$ . It has been shown, however, that the transient response at a single aspect may be Fourier transformed to give approximate results in both the "forward-look" and "rear-look" regions [24]. Thus, we applied a  $60^\circ$  window in Case III where the window is  $\pm 60^\circ$  from the nose on aspect and symmetric and the resulting images before and after the threshold filter are seen in Figures 58 to 61c. In Case IV we applied a  $30^\circ$  window and the corresponding results are in Figures 62 to 65c.

For the  $60^\circ$  window the degradation is insignificant and for the  $30^\circ$  window the degradation varies for each shape. As we earlier stated it is reasonable to assume the triangular shape would suffer the greatest in resolution because the lobes perpendicular to the sides were eliminated in the  $30^\circ$  windowing whereas the spectra due to the square or circular shapes contained more information and energy within the window. This naturally tells us that image reconstruction is dependent on the angle of the window axis as well as the width of the angular window. Even though we lose contour information at angles outside the window we can infer the identity of the square and circular targets from the clearly defined edges after the threshold filter is applied. And to some extent the triangular shape is preserved.

#### Frequency and aspect windowing

A p-space window representing both frequency and angle windowing is shown in Figure 66. The result of applying both windows in cascade is seen in Figures 67 to 74c before and after threshold filtering. Case V, Figures 67 to 70c demonstrates the application of a 10-30 point frequency filter and a  $60^\circ$  window and the results are good enough to distinguish all three shapes. Case VI, Figures 71 to 74c, yields the results of a 10-30 point frequency filter and a  $30^\circ$  aspect angle window. Here the square and circular targets may be defined and all three may be distinguished but it is apparent that the most significant degradation results from the application of a narrow aspect window. This leads to the discussion of possibly extending the aspect angle window so as to yield better results.

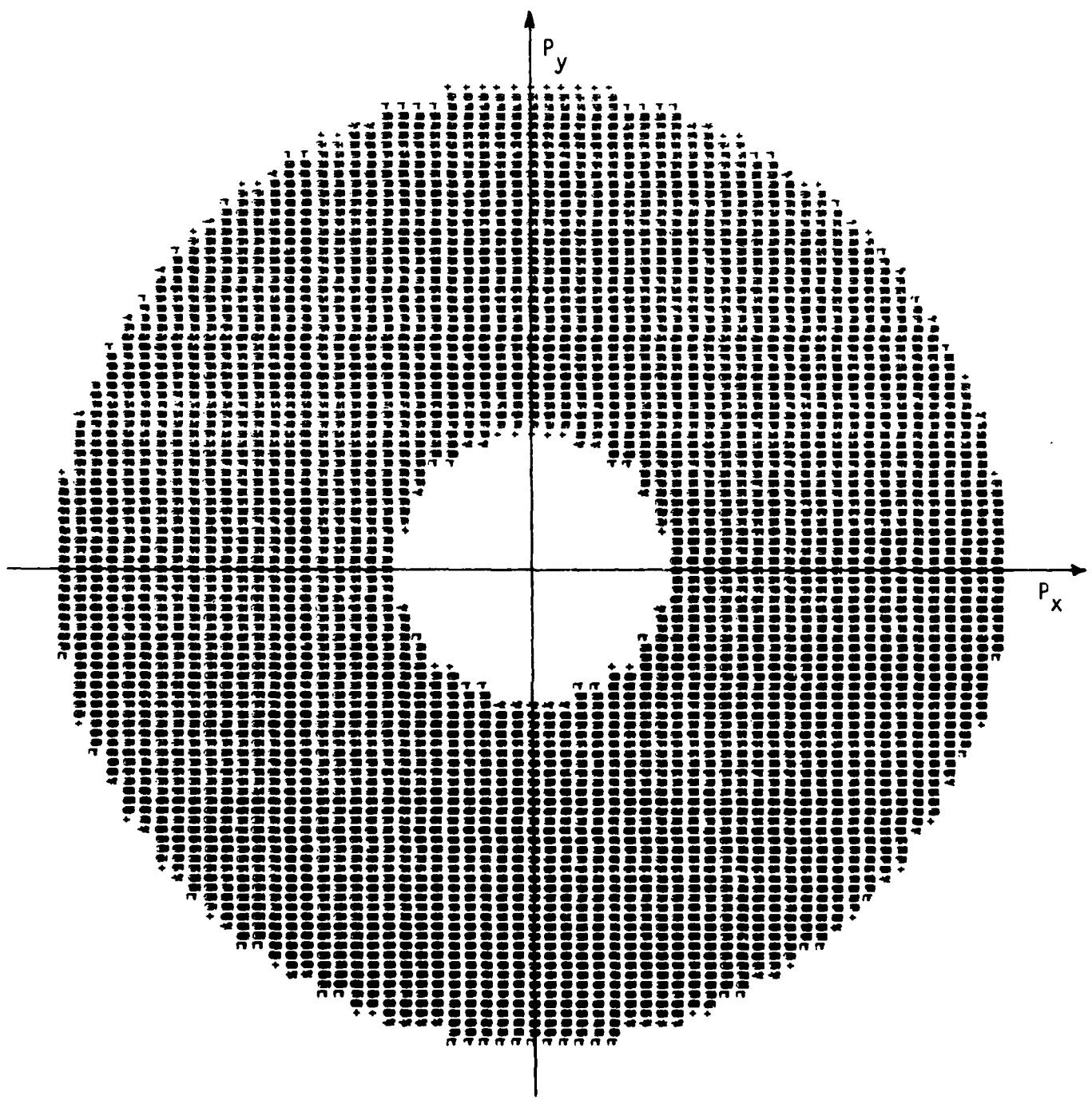


Figure 48. Two dimensional bandpass P-space filter at all aspects.

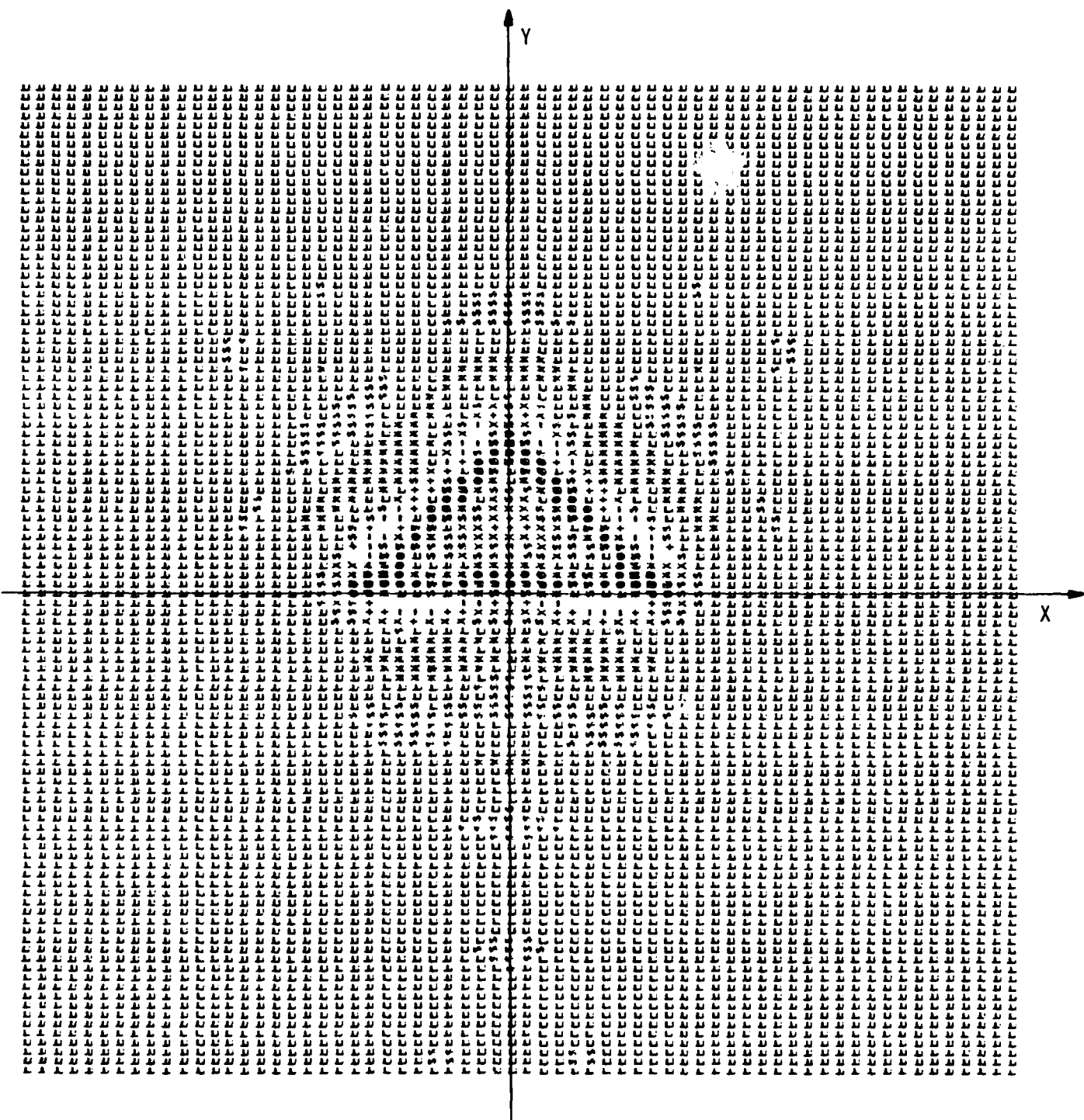


Figure 49. Image of triangular scatterer after bandpass filtering:  
 $\bar{P}_{\text{low}} = 10^{\text{th}}$  sample point -  $\bar{P}_{\text{high}} = 30^{\text{th}}$  sample point

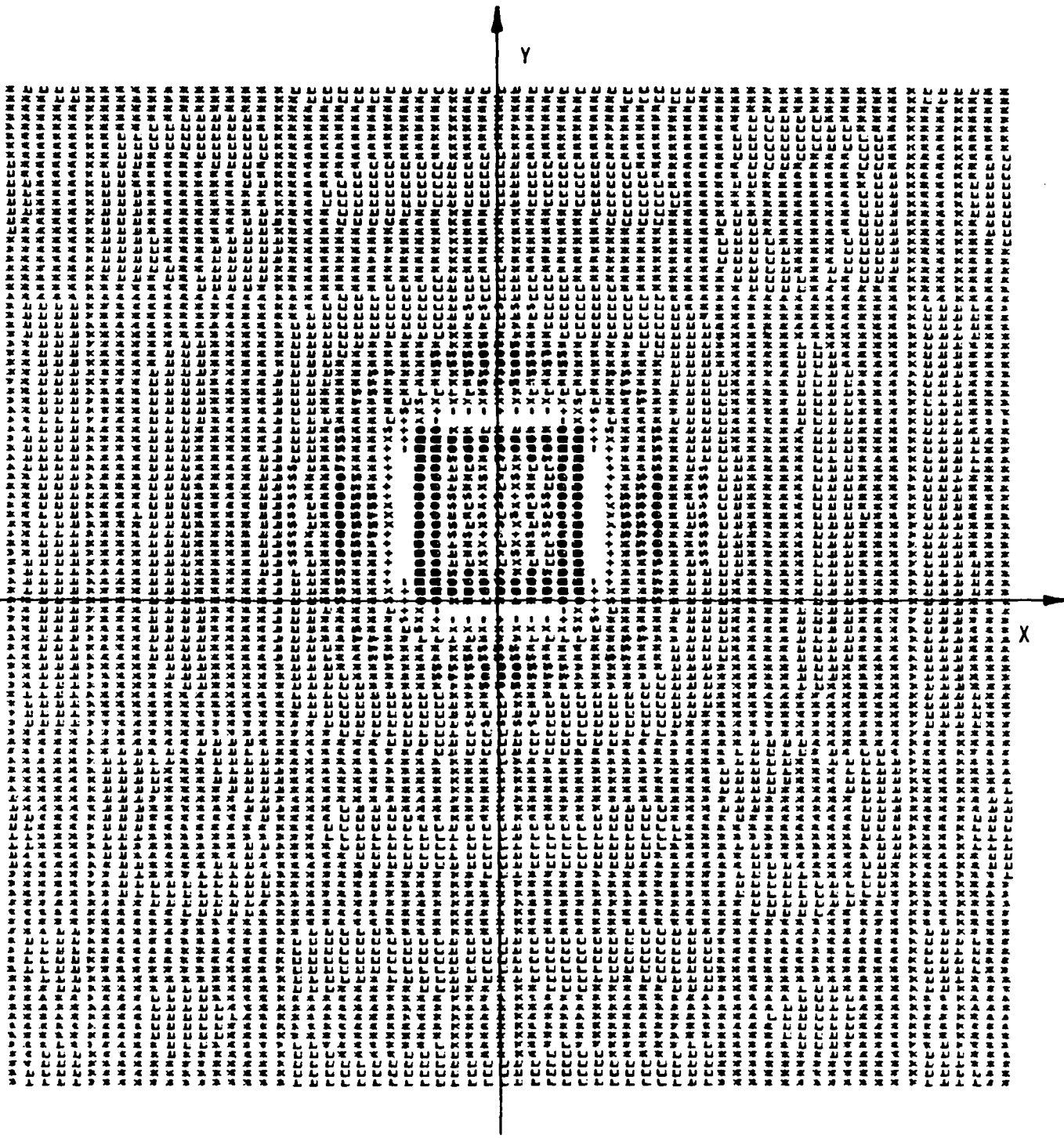


Figure 50. Image of square scatterer after bandpass filtering:  
 $\bar{P}_{\text{low}} = 10^{\text{th}}$  sample point -  $\bar{P}_{\text{high}} = 30^{\text{th}}$  sample point

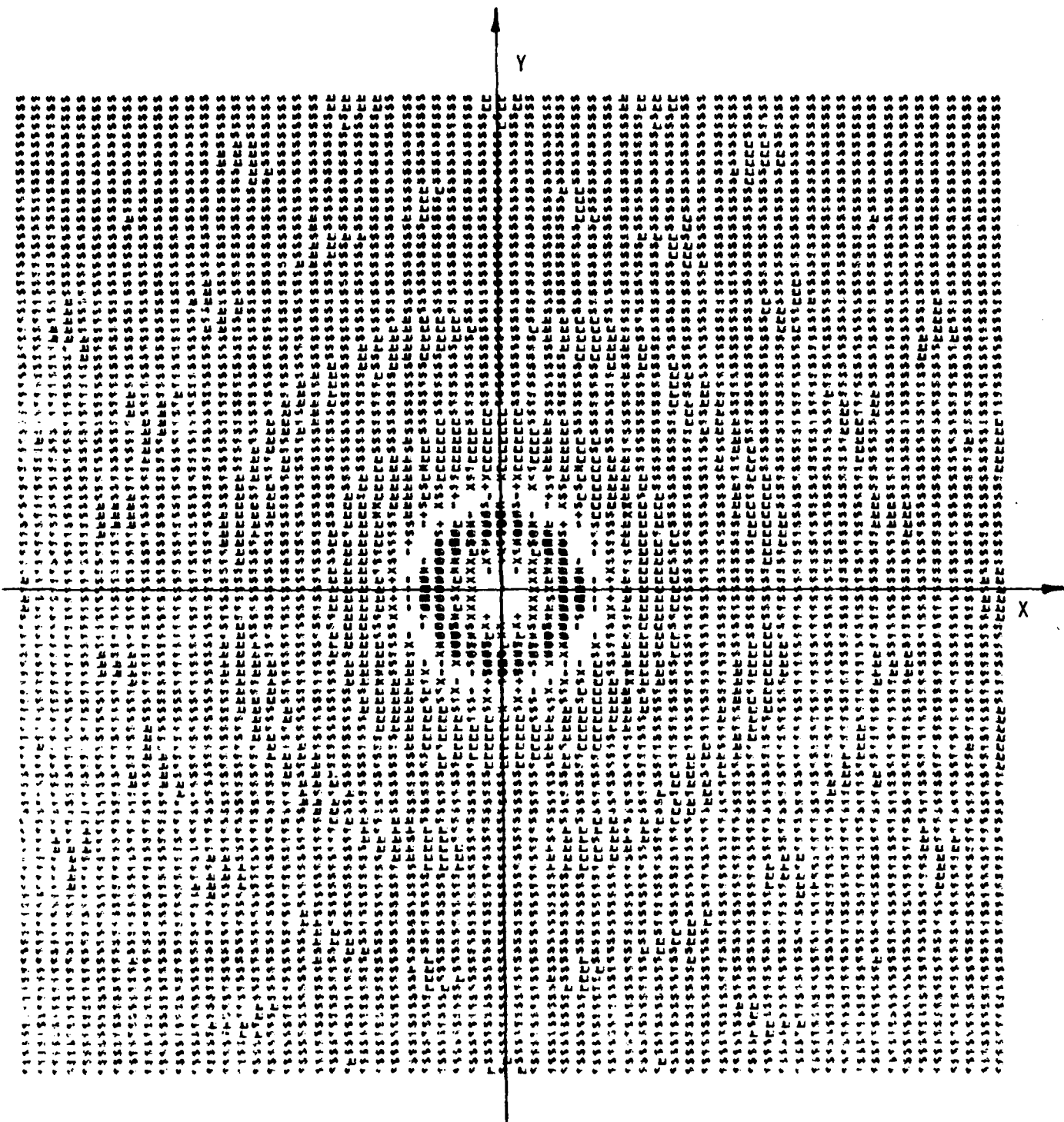


Figure 51. Image of circular scatterer after bandpass filtering:  
 $P_{\text{low}} = 10^{\text{th}}$  sample point -  $P_{\text{high}} = 30^{\text{th}}$  sample point

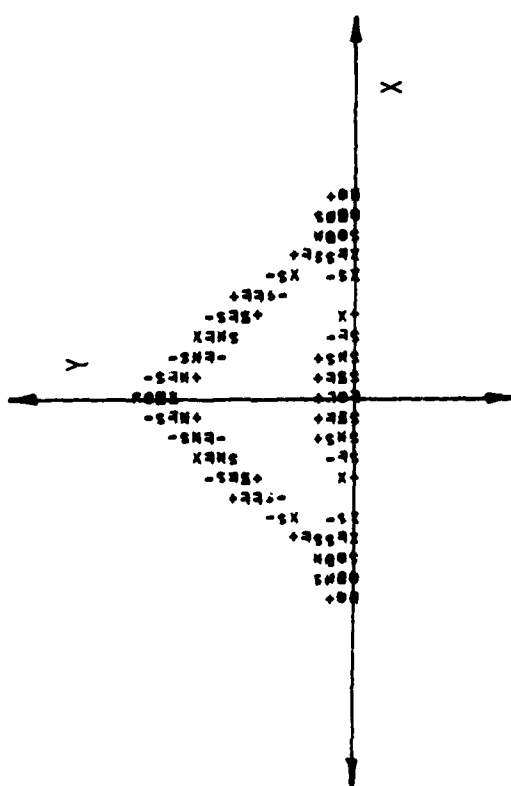


Figure 52a. Image of triangular scatterer  
after bandpass filtering and  
threshold filtering:  
 $\bar{P}_{10w} = 10^{\text{th}}$  sample point  
 $\bar{P}_{high} = 30^{\text{th}}$  sample point

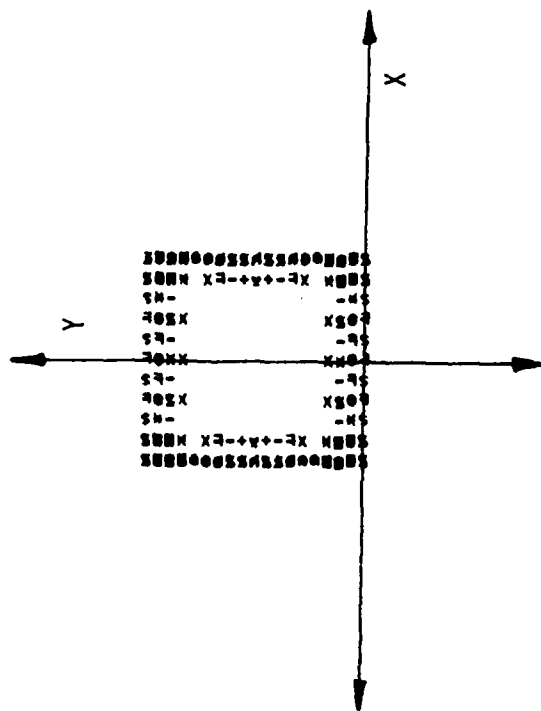


Figure 52b. Image of square scatterer  
after bandpass filtering  
and threshold filtering:  
 $\bar{P}_{10w} = 10^{\text{th}}$  sample point  
 $\bar{P}_{high} = 30^{\text{th}}$  sample point

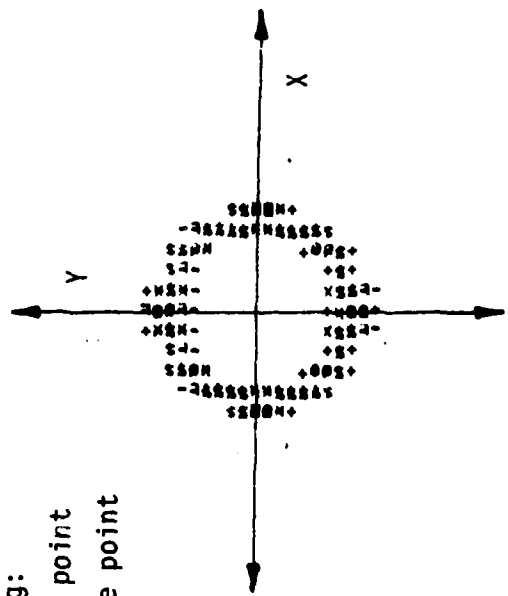


Figure 52c. Image of circular scatterer after bandpass  
filtering and threshold filtering:  
 $\bar{P}_{10w} = 10^{\text{th}}$  sample point -  $\bar{P}_{high} = 30^{\text{th}}$  sample point

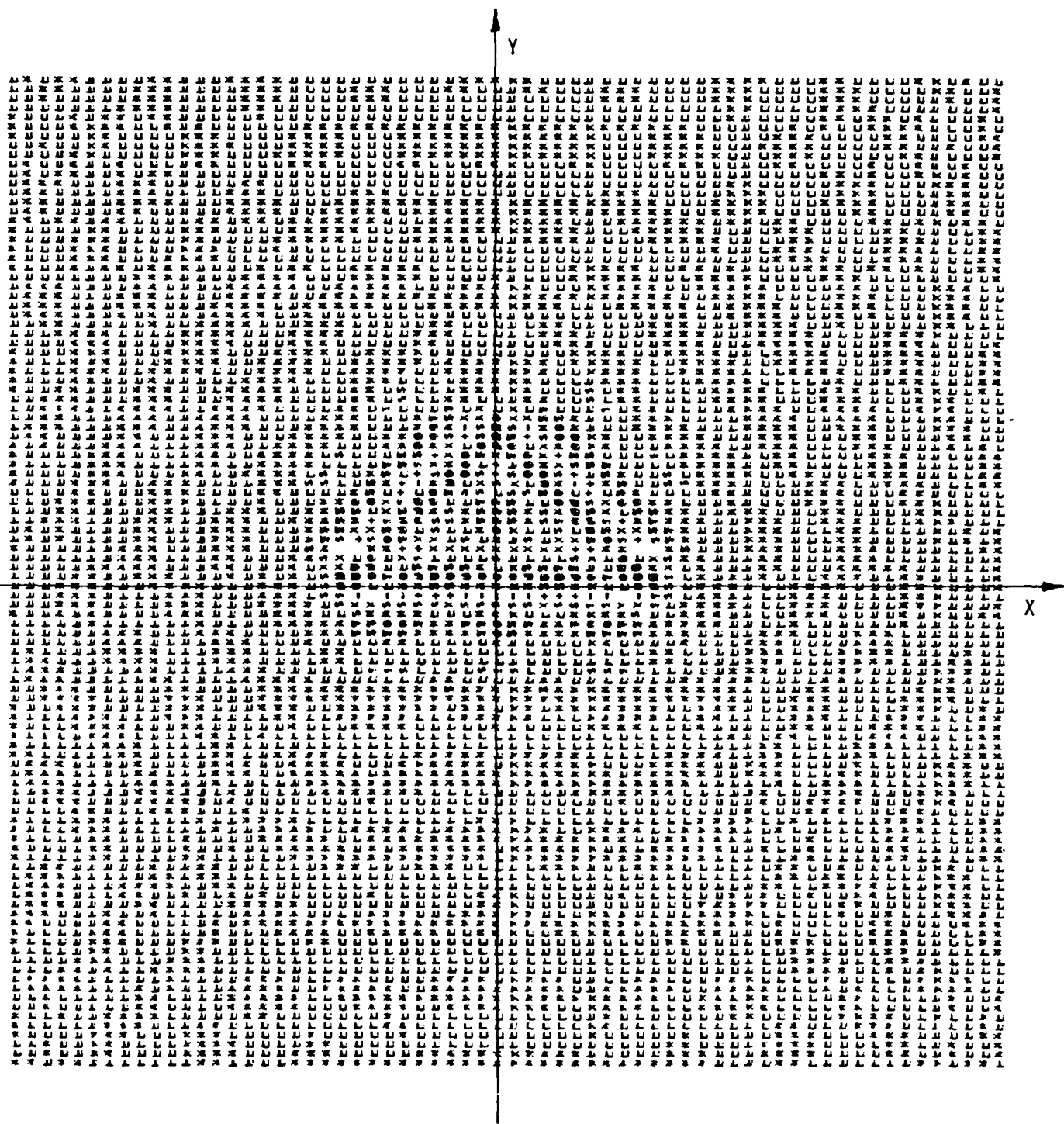


Figure 53. Image of triangular scatterer after bandpass filtering:  
 $P_{\text{low}} = 15^{\text{th}}$  sample point -  $P_{\text{high}} = 30^{\text{th}}$  sample point

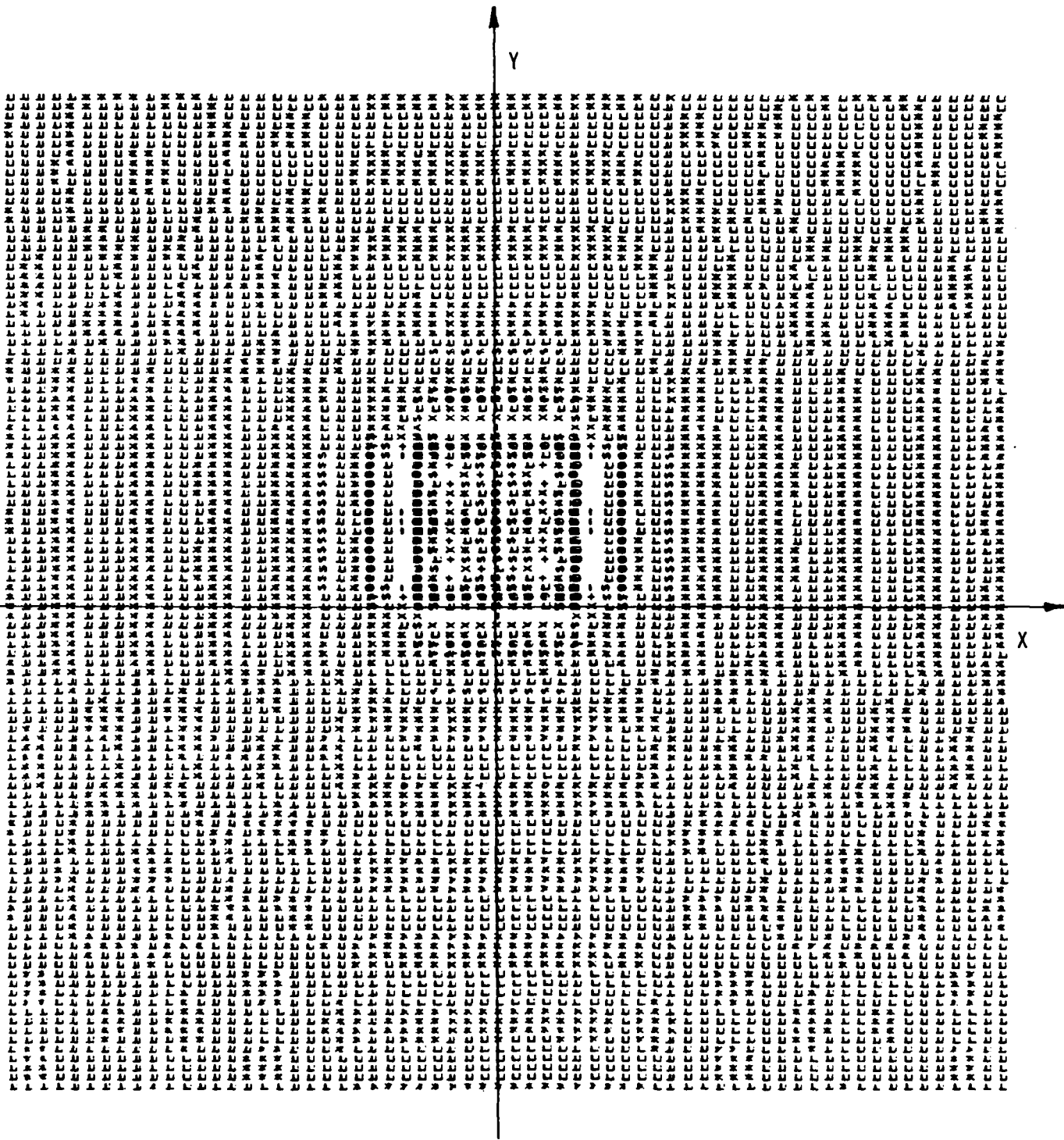


Figure 54. Image of square scatterer after bandpass filtering:  
 $\bar{P}_{\text{low}} = 15^{\text{th}}$  sample point -  $\bar{P}_{\text{high}} = 30^{\text{th}}$  sample point

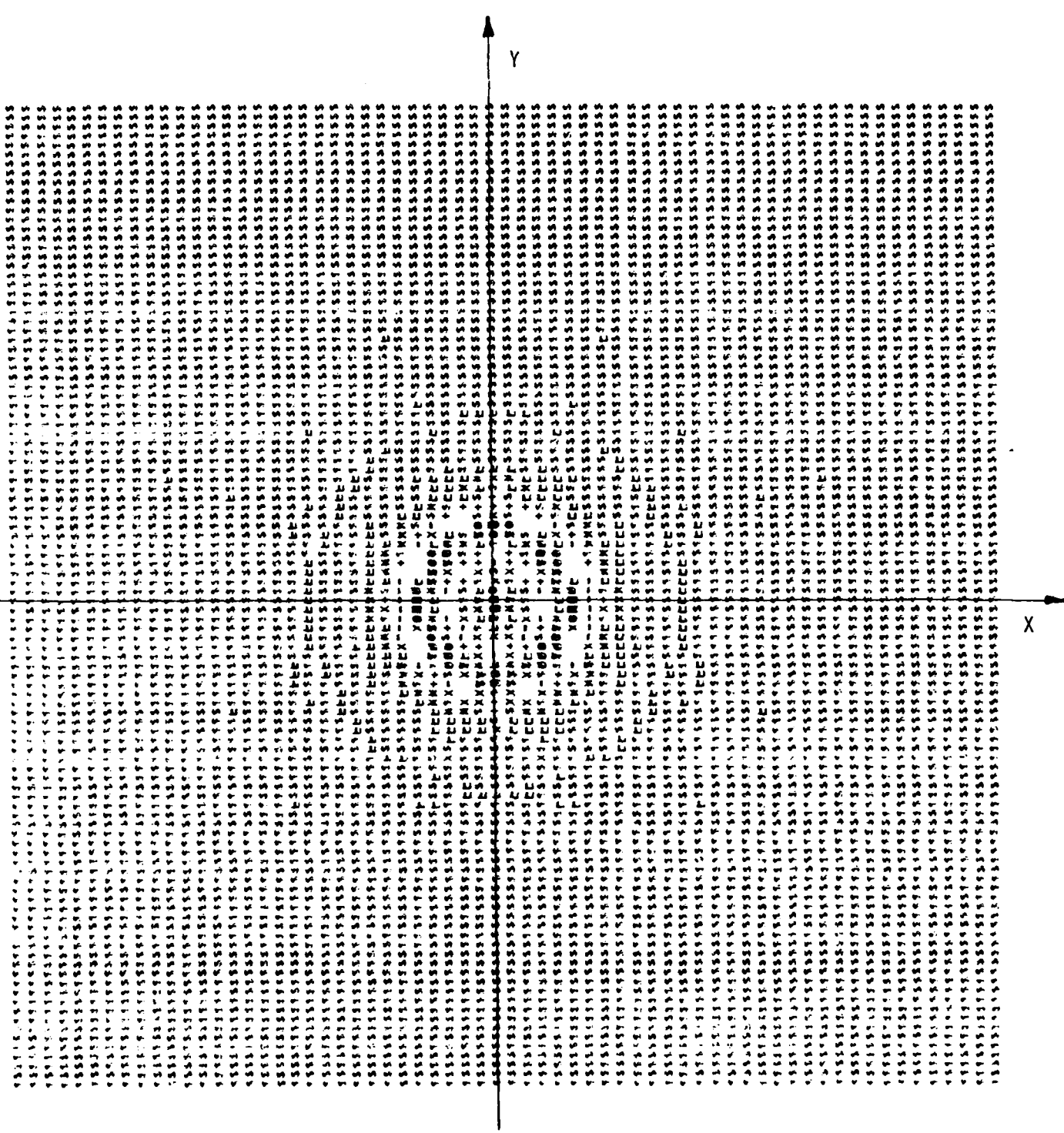


Figure 55. Image of circular scatterer after bandpass filtering:  
 $P_{\text{low}} = 15^{\text{th}}$  sample point -  $P_{\text{high}} = 30^{\text{th}}$  sample point

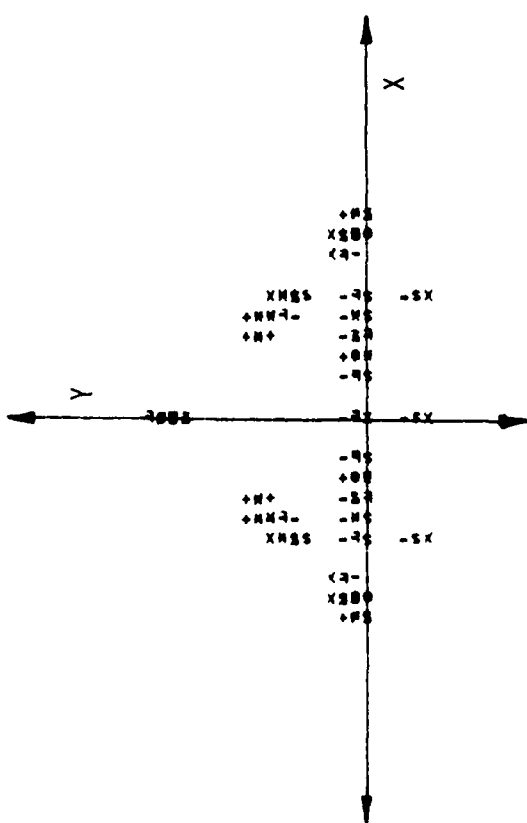


Figure 56a. Image of triangular scatterer after bandpass filtering and threshold filtering:  
 $\bar{P}_{\text{low}} = 15^{\text{th}}$  sample point  
 $\bar{P}_{\text{high}} = 30^{\text{th}}$  sample point

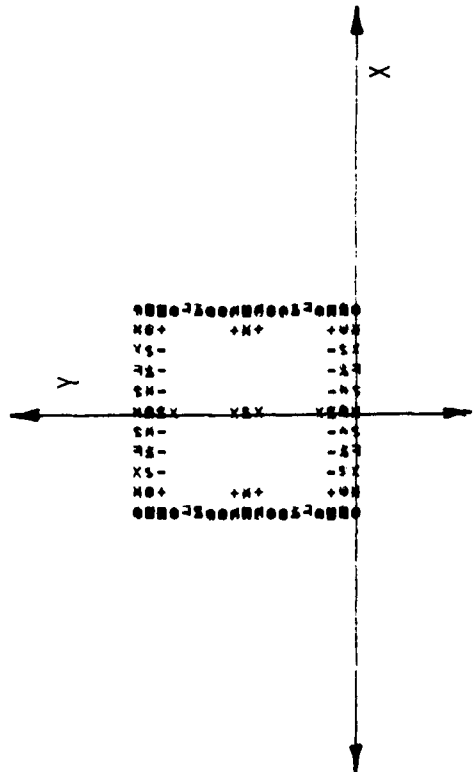


Figure 56b. Image of square scatterer after bandpass filtering and threshold filtering:  
 $\bar{P}_{\text{low}} = 15^{\text{th}}$  sample point  
 $\bar{P}_{\text{high}} = 30^{\text{th}}$  sample point

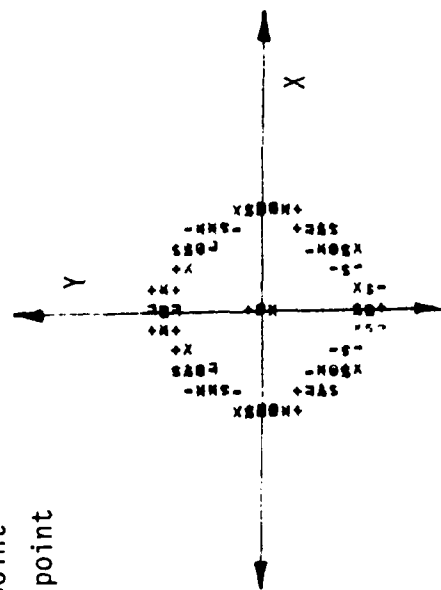


Figure 56c. Image of circular scatterer after bandpass filtering and threshold filtering:  
 $\bar{P}_{\text{low}} = 15^{\text{th}}$  sample point -  $\bar{P}_{\text{high}} = 30^{\text{th}}$  sample point

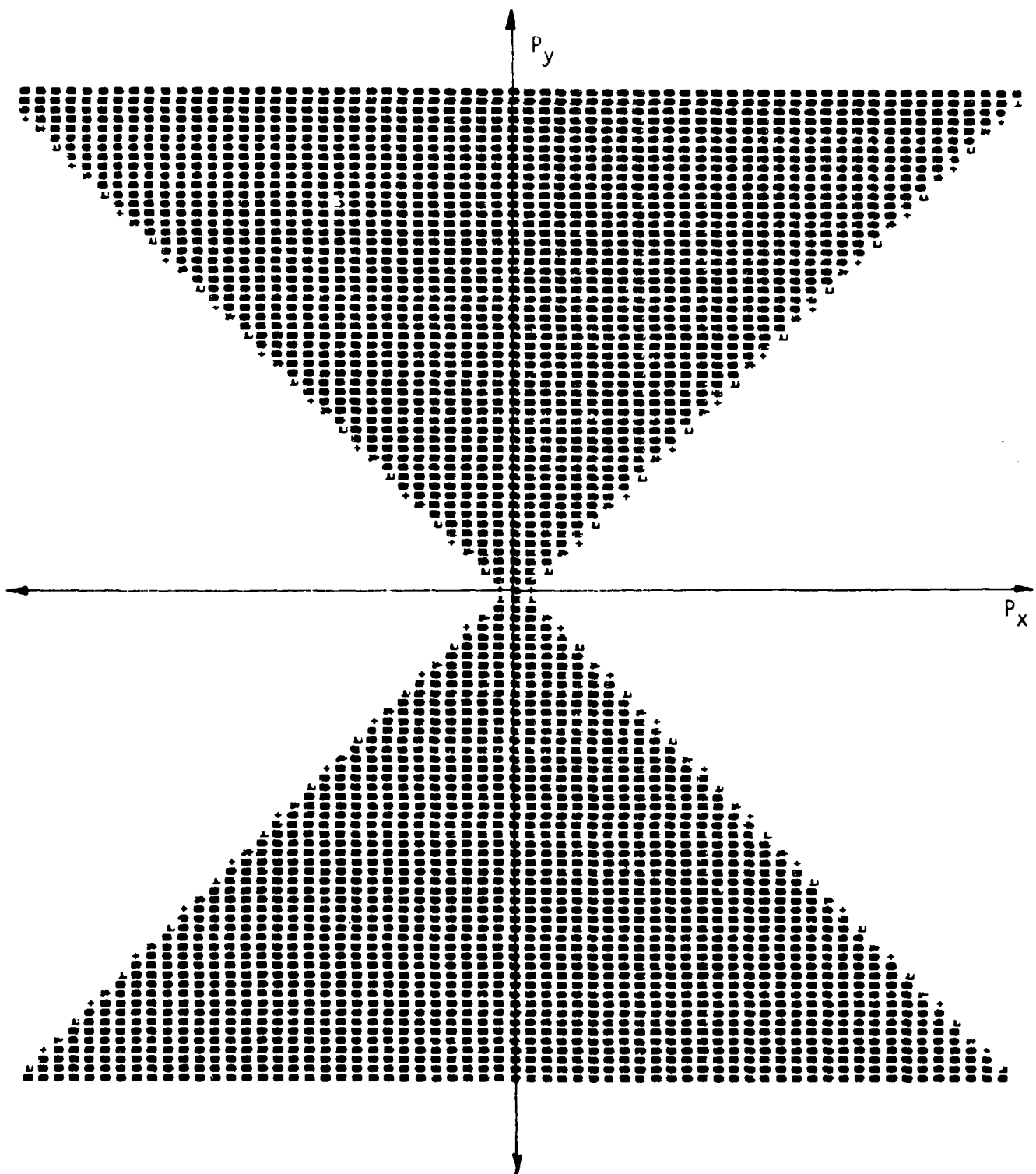


Figure 57. Two dimensional aspect angle P-space filter at all frequencies.

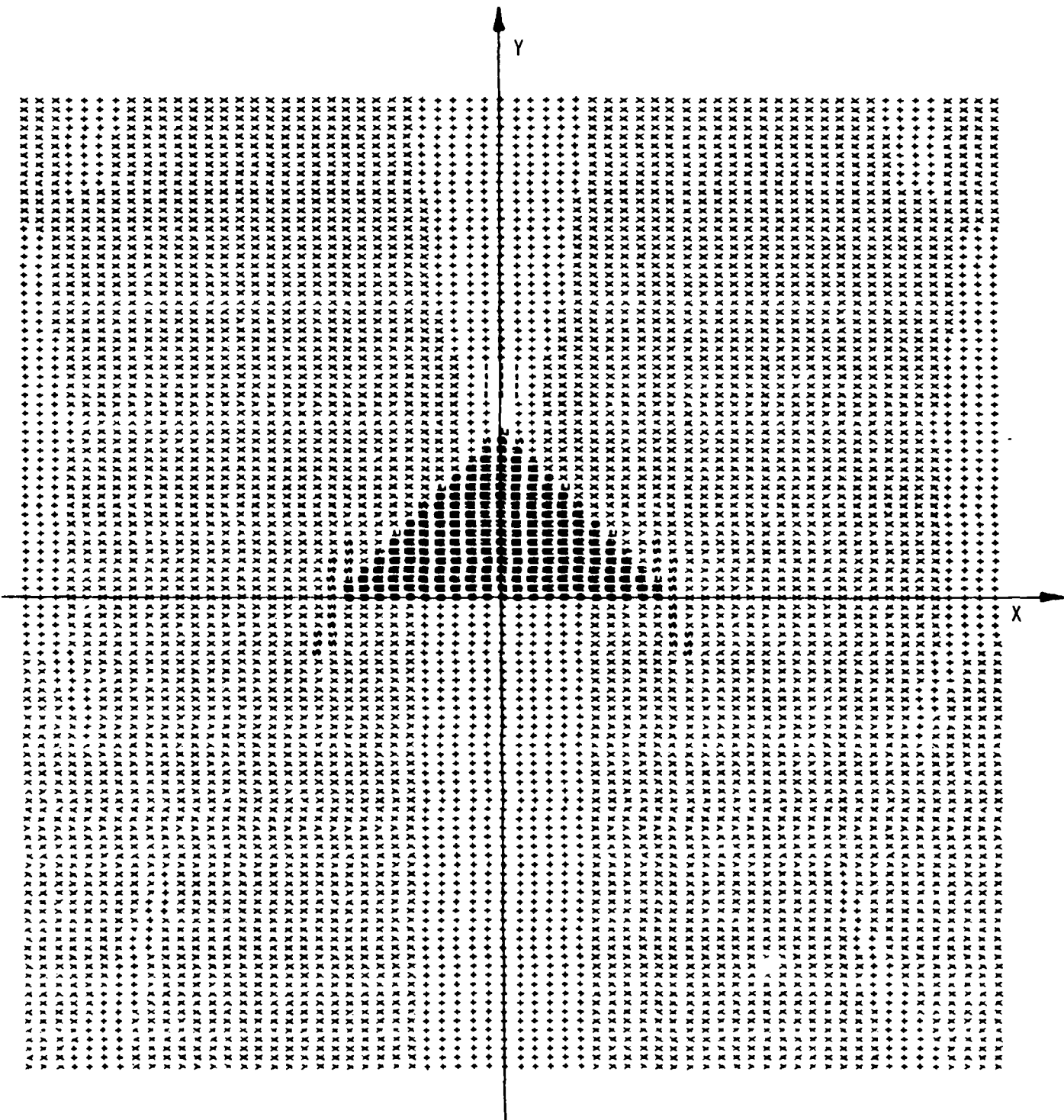


Figure 58. Image of triangular scatterer after aspect angle filtering:  
angle =  $60^\circ$ .

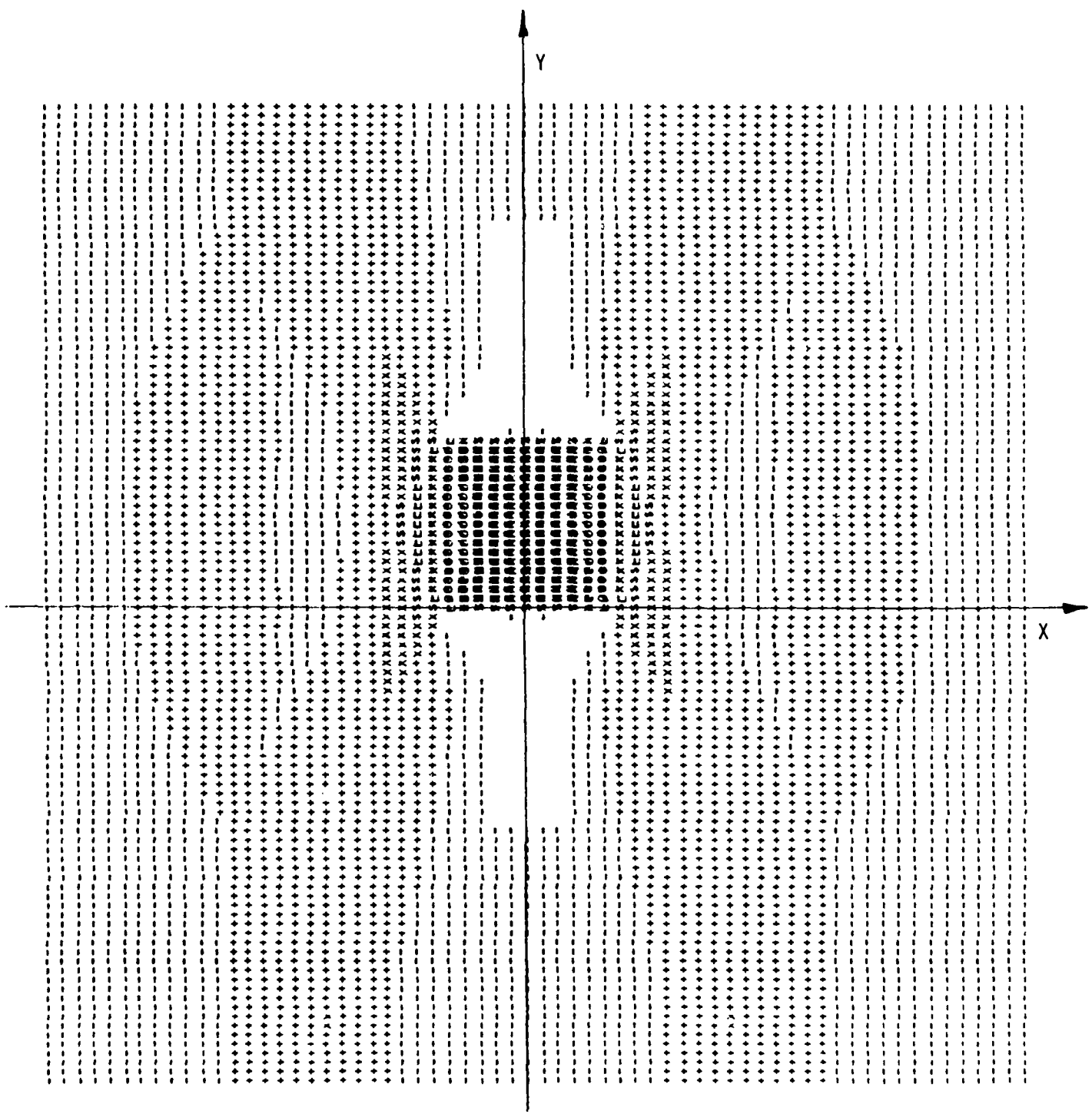


Figure 59. Image of square scatterer after aspect angle filtering:  
angle =  $60^\circ$ .

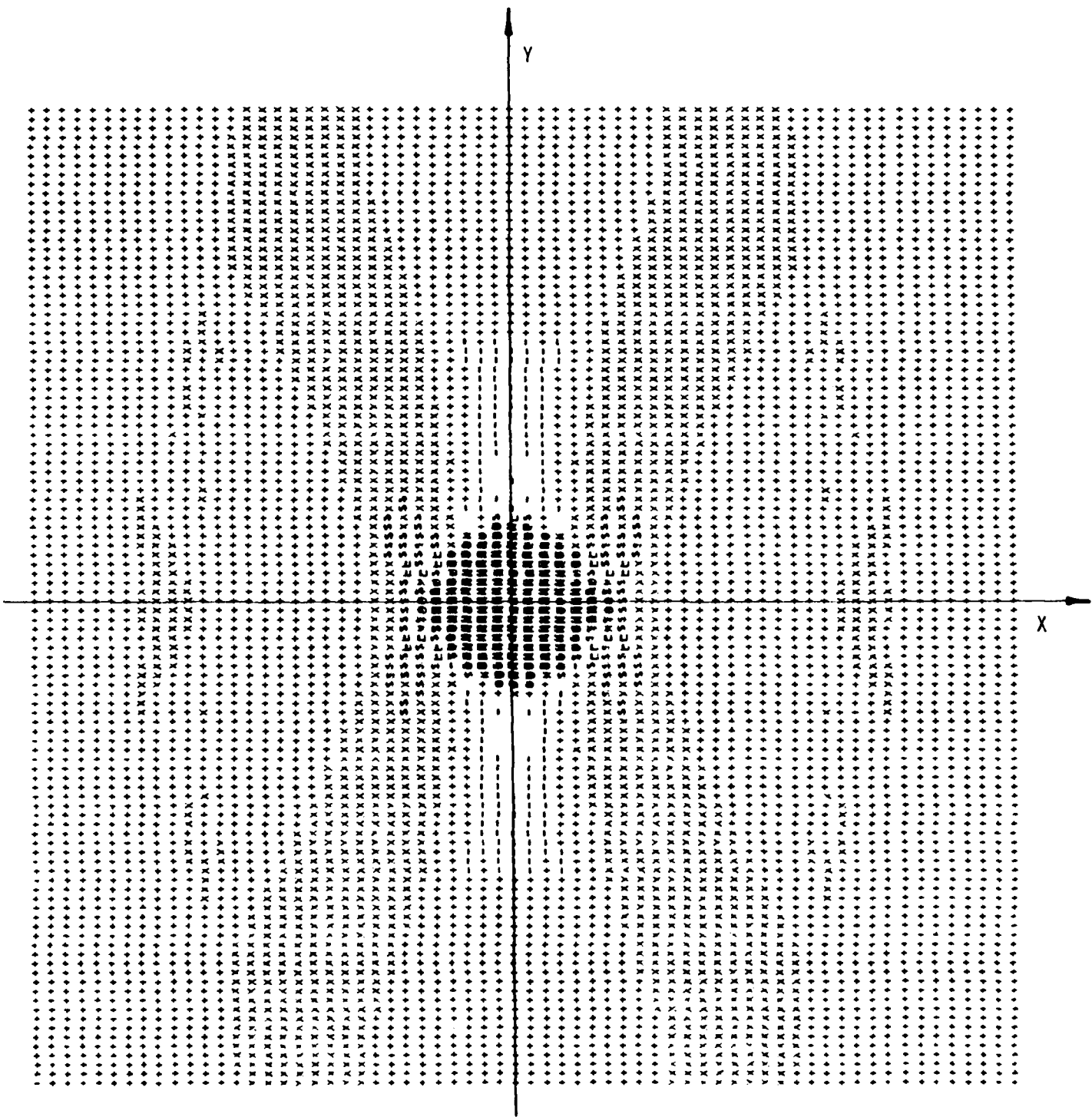


Figure 60. Image of circular scatterer after aspect angle filtering:  
angle =  $60^\circ$ .

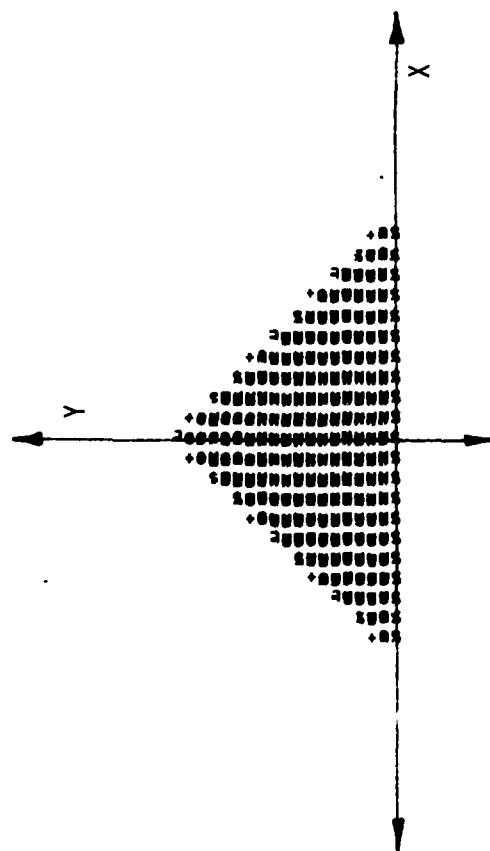


Figure 61a. Image of triangular scatterer after aspect angle filtering and threshold filtering: angle=60°.

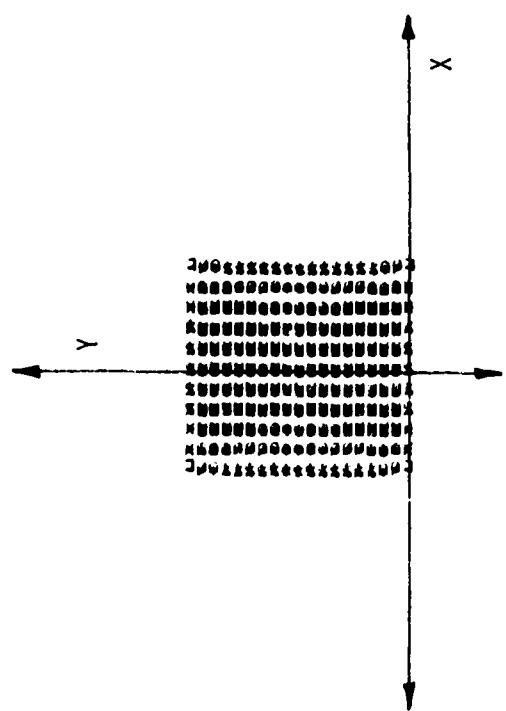


Figure 61b. Image of square scatterer after aspect angle filtering and threshold filtering: angle=60°.

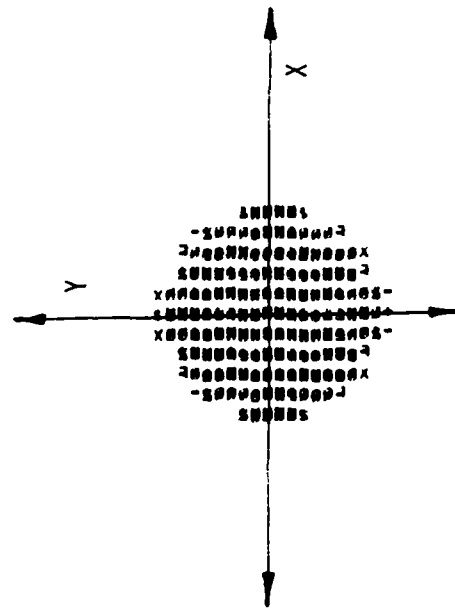


Figure 61c. Image of circular scatterer after aspect angle filtering and threshold filtering: angle=60°.

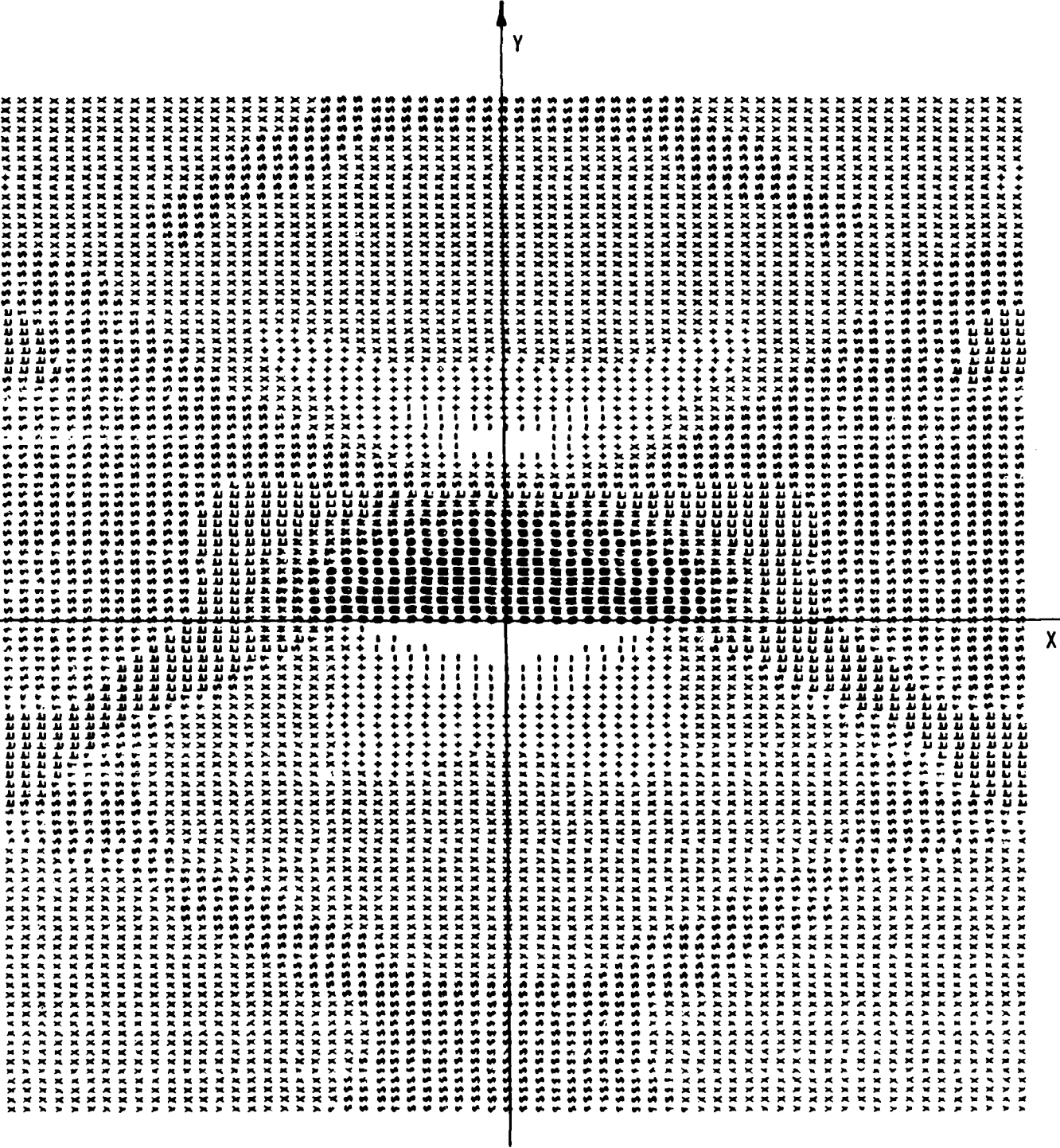


Figure 62. Image of triangular scatterer after aspect angle filtering:  
angle = 30°.

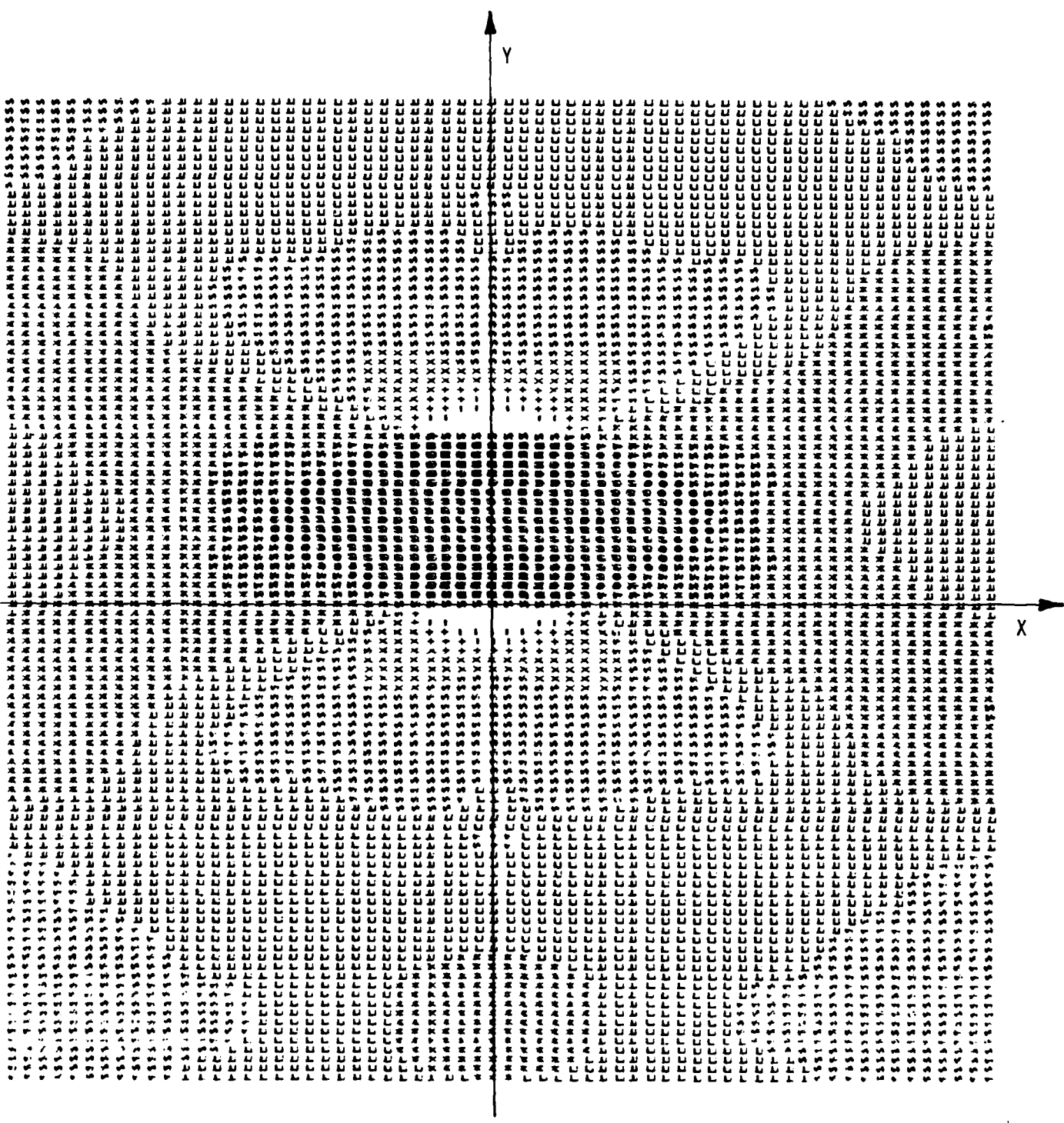


Figure 63. Image of square scatterer after aspect angle filtering:  
angle =  $30^\circ$ .

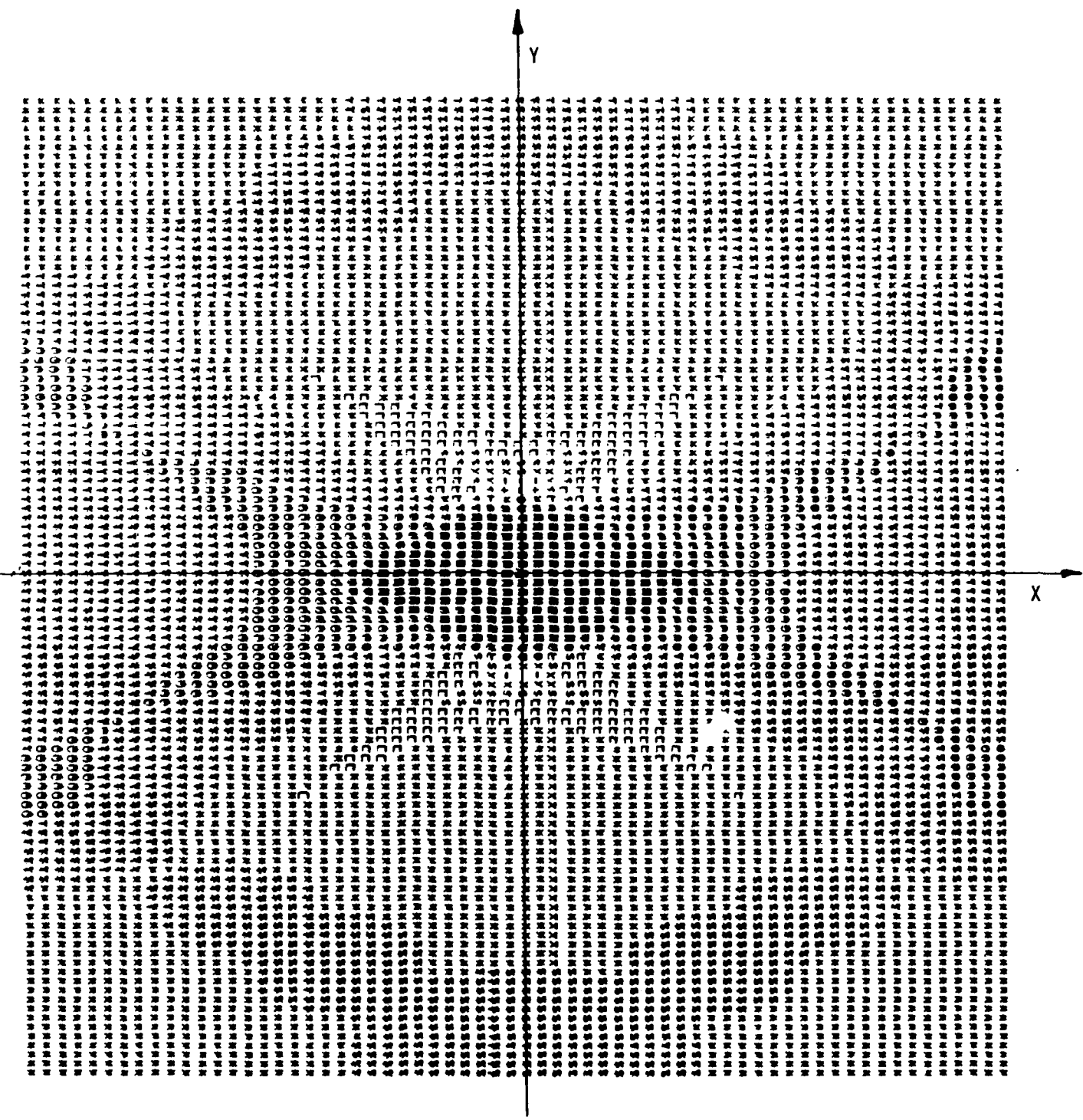


Figure 64. Image of circular scatterer after aspect angle filtering:  
angle =  $30^\circ$ .

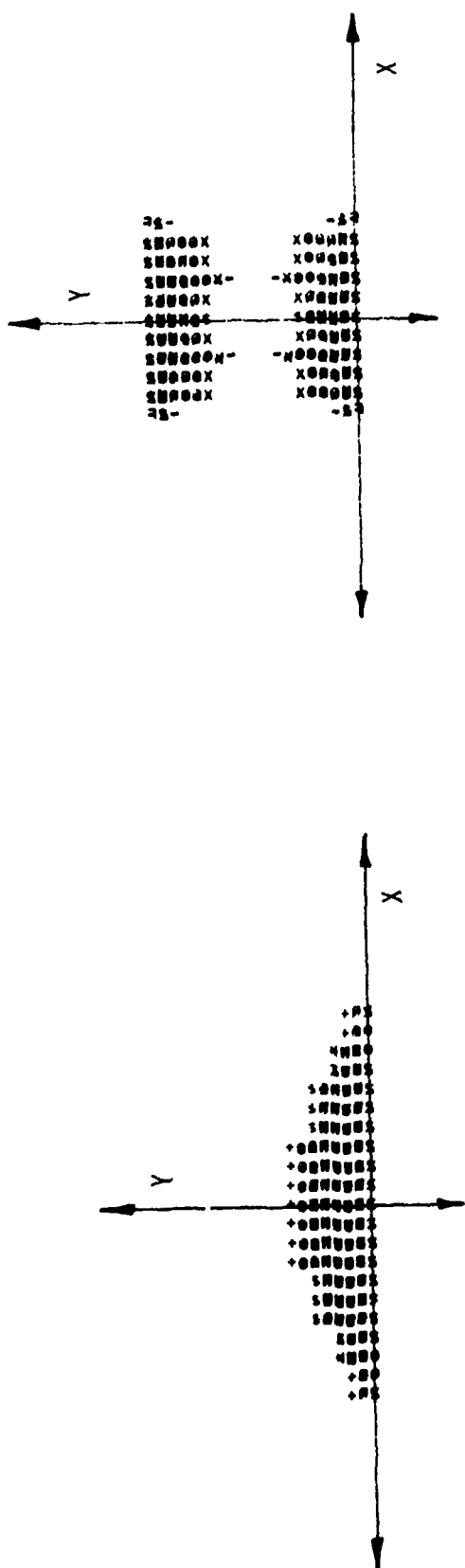


Figure 65a. Image of triangular scatterer after aspect angle filtering and threshold filtering: angle=30°.

Figure 65b. Image of square scatterer after aspect angle filtering and threshold filtering: angle=30°.

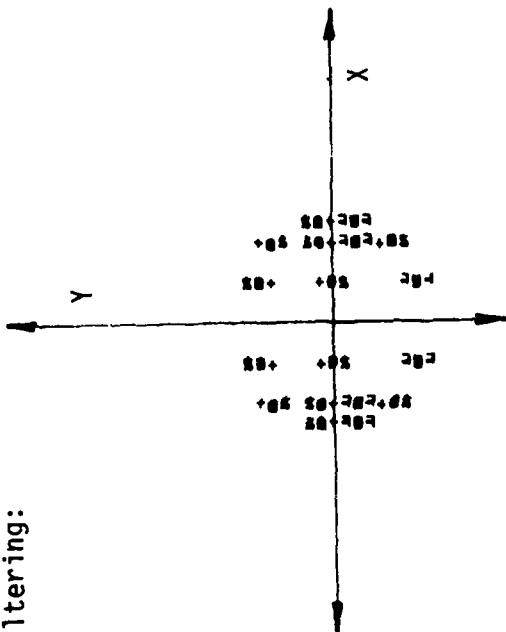


Figure 65c. Image of circular scatterer after aspect angle filtering and threshold filtering: angle=30°.

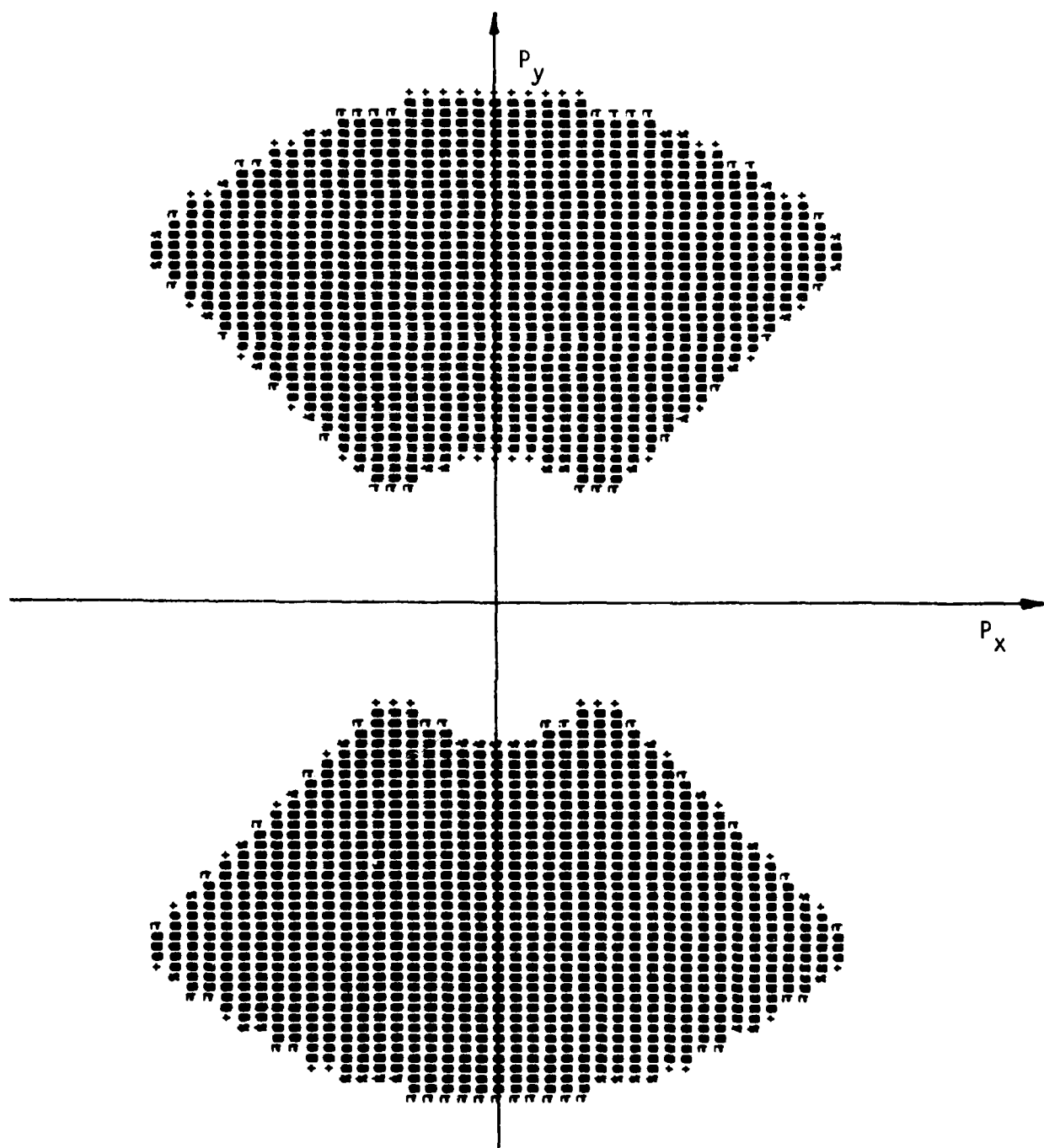


Figure 66. Combination of aspect angle filter and bandpass filter in P-space.

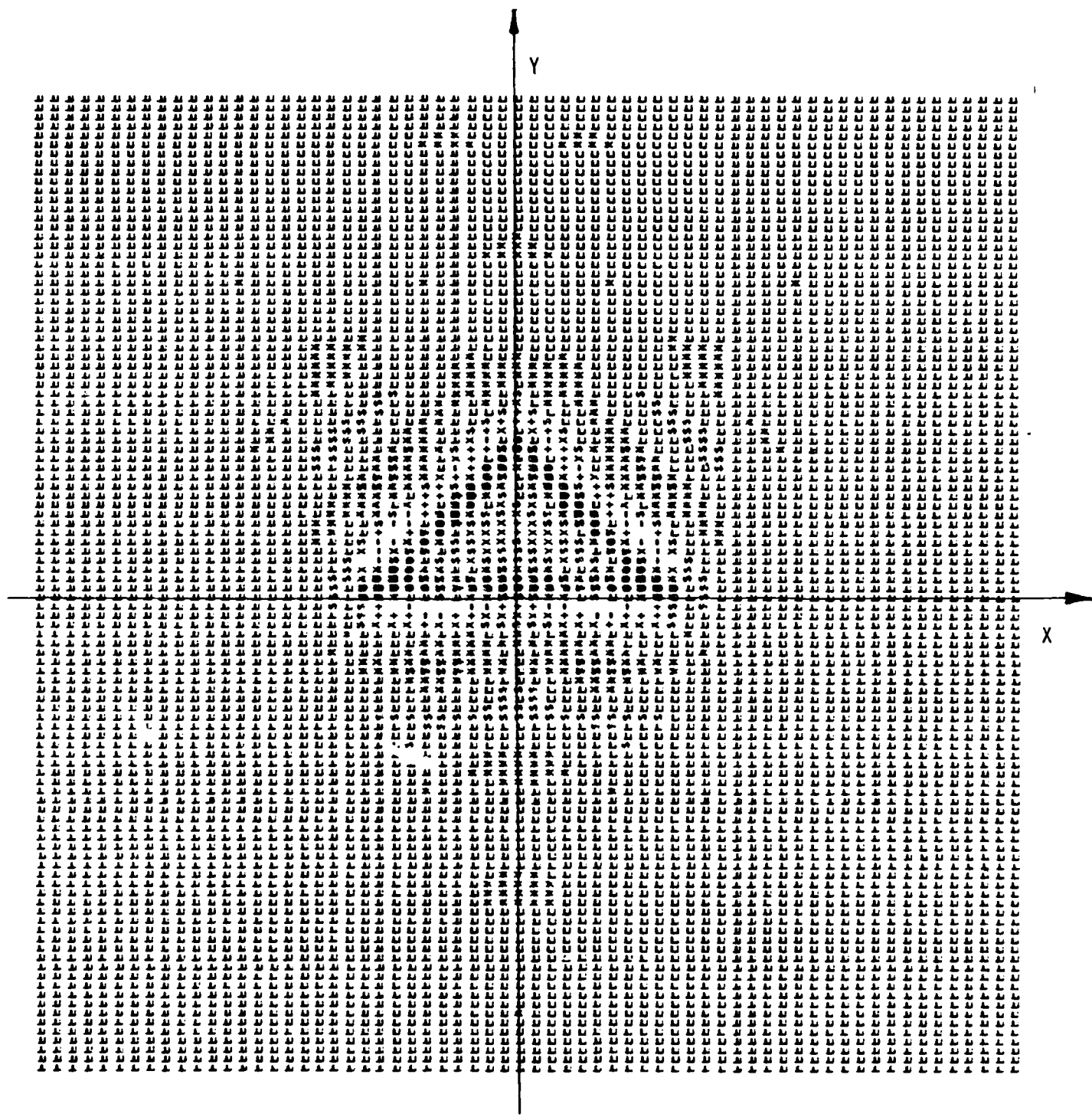


Figure 67. Image of triangular scatterer after bandpass and aspect angle filtering:  $P_{low} = 10^{th}$  sample point,  $P_{high} = 30^{th}$  sample point, angle=60°.

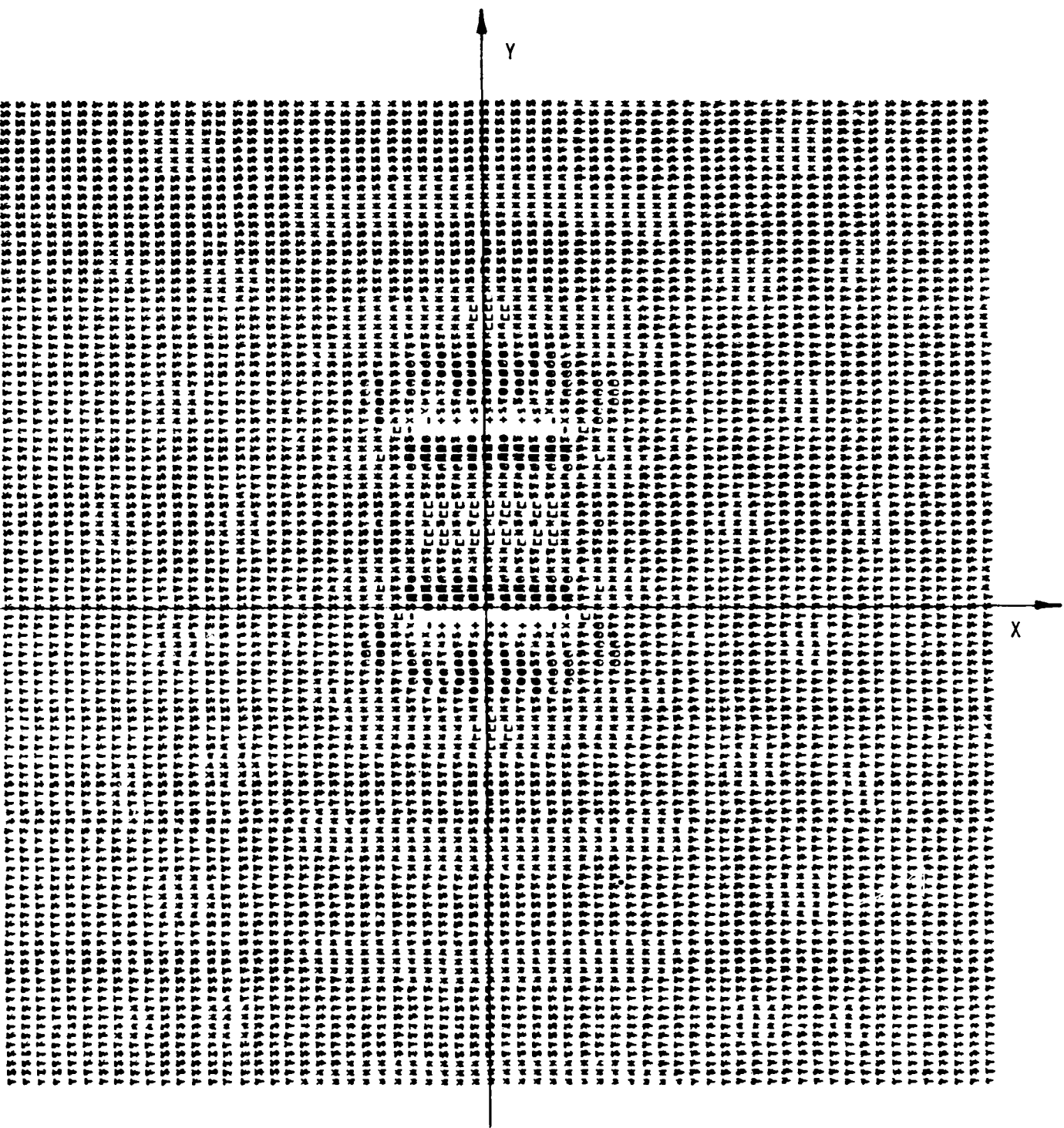


Figure 68. Image of square scatterer after bandpass and aspect angle filtering:  $P_{low} = 10^{\text{th}}$  sample point,  $P_{high} = 30^{\text{th}}$  sample point, angle=60°.

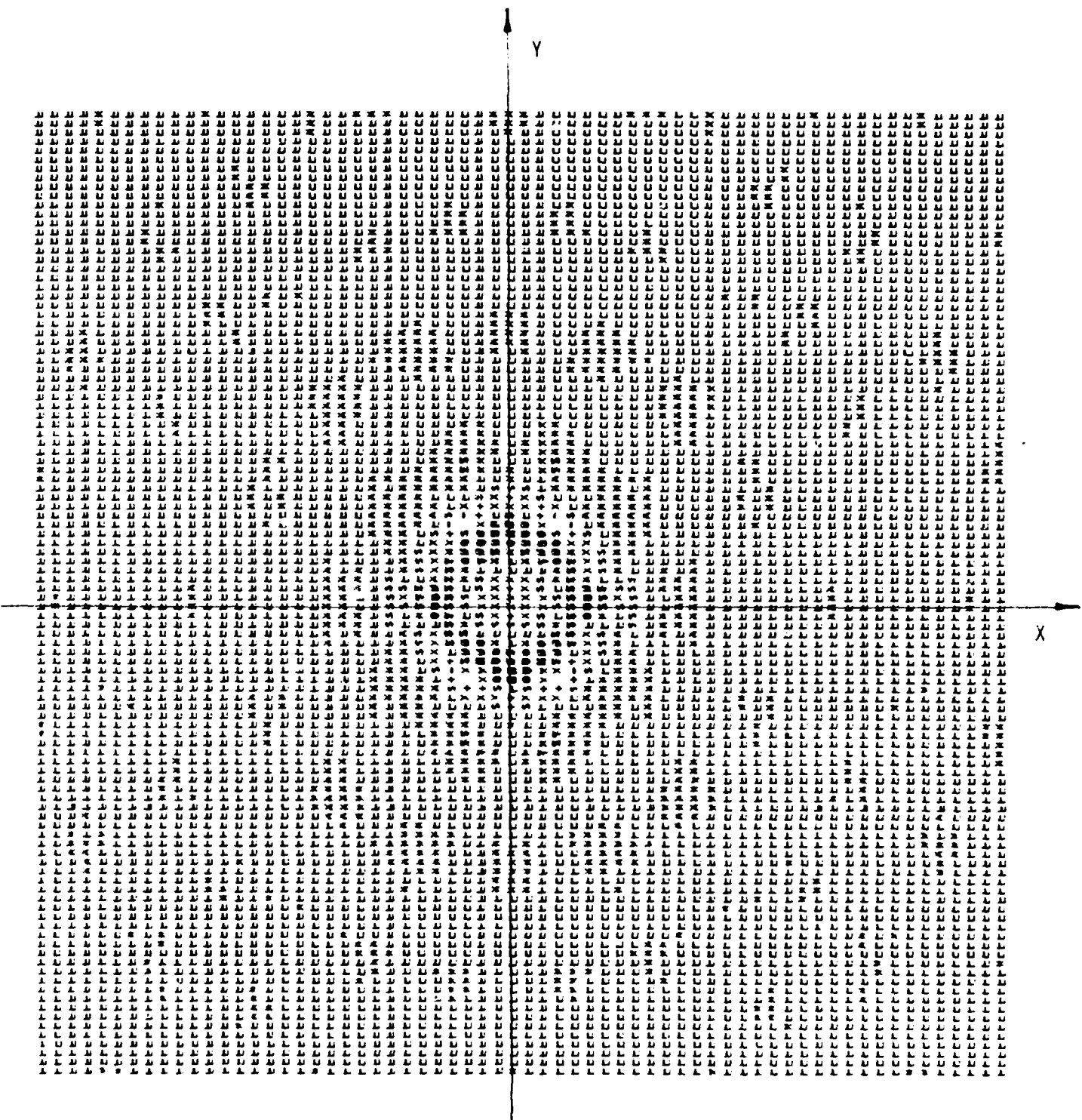


Figure 69. Image of circular scatterer after bandpass and aspect angle filtering:  $\bar{P}_{\text{low}} = 10^{\text{th}}$  sample point,  $\bar{P}_{\text{high}} = 30^{\text{th}}$  sample point, angle=60°.

RD-R121 374

BASIC RESEARCH IN THREE-DIMENSIONAL IMAGING FROM  
TRANSIENT RADAR SCATTERI. (U) OHIO STATE UNIV COLUMBUS  
ELECTROSCIENCE LAB J D YOUNG ET AL JUL 78

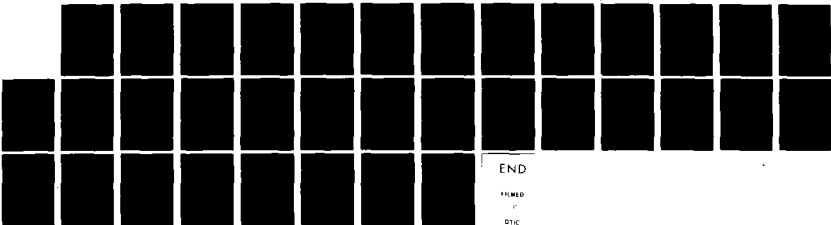
272

UNCLASSIFIED

ESL-784785-1 DASG60-77-C-0133

F/G 17/9

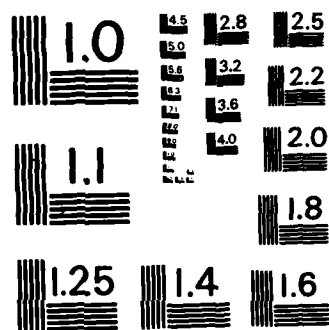
NL



END

ARMED

BTIC



MICROCOPY RESOLUTION TEST CHART  
NATIONAL BUREAU OF STANDARDS-1963-A

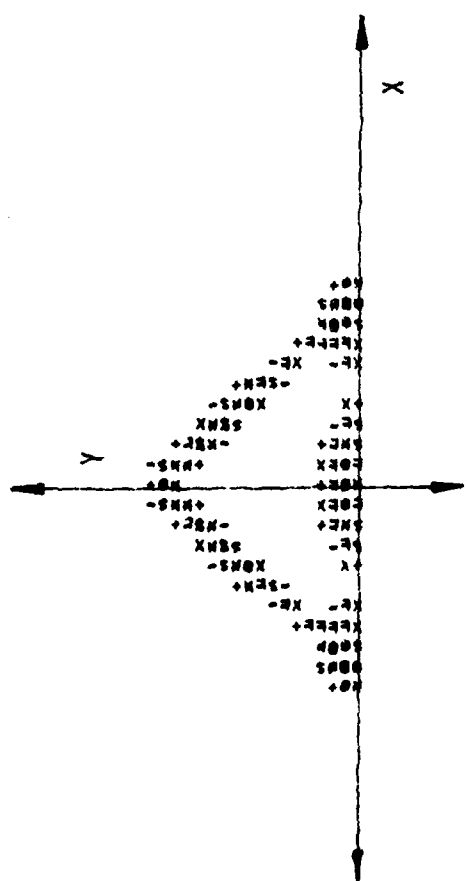


Figure 70a. Image of triangular scatterer after bandpass, aspect angle and threshold filtering:  
 $\bar{P}_{\text{low}} = 10^{\text{th}}$  sample point  
 $\bar{P}_{\text{high}} = 30^{\text{th}}$  sample point  
angle =  $60^\circ$

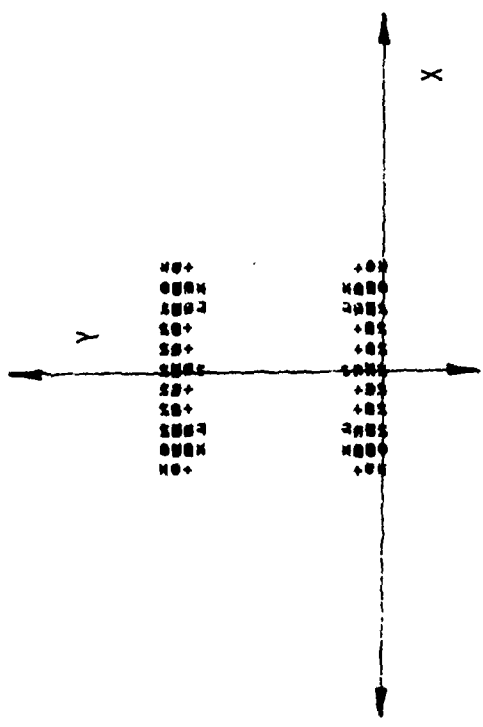


Figure 70b. Image of square scatterer after bandpass, aspect angle and threshold filtering:  
 $\bar{P}_{\text{low}} = 10^{\text{th}}$  sample point  
 $\bar{P}_{\text{high}} = 30^{\text{th}}$  sample point  
angle =  $60^\circ$

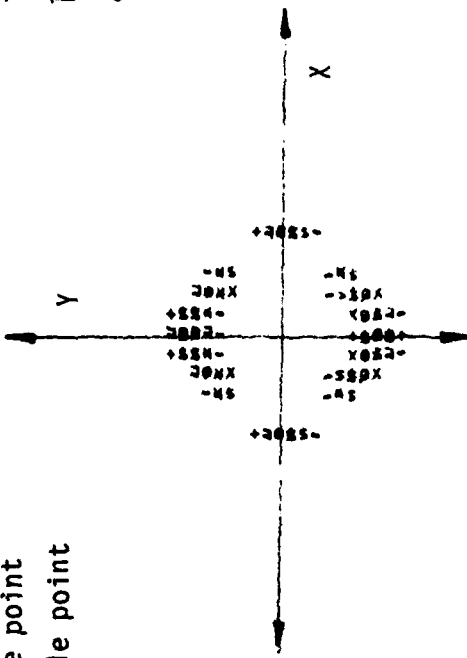


Figure 70c. Image of circular scatterer after bandpass, aspect angle and threshold filtering:  
 $\bar{P}_{\text{low}} = 10^{\text{th}}$  sample point -  $\bar{P}_{\text{high}} = 30^{\text{th}}$  sample point  
angle =  $60^\circ$ .

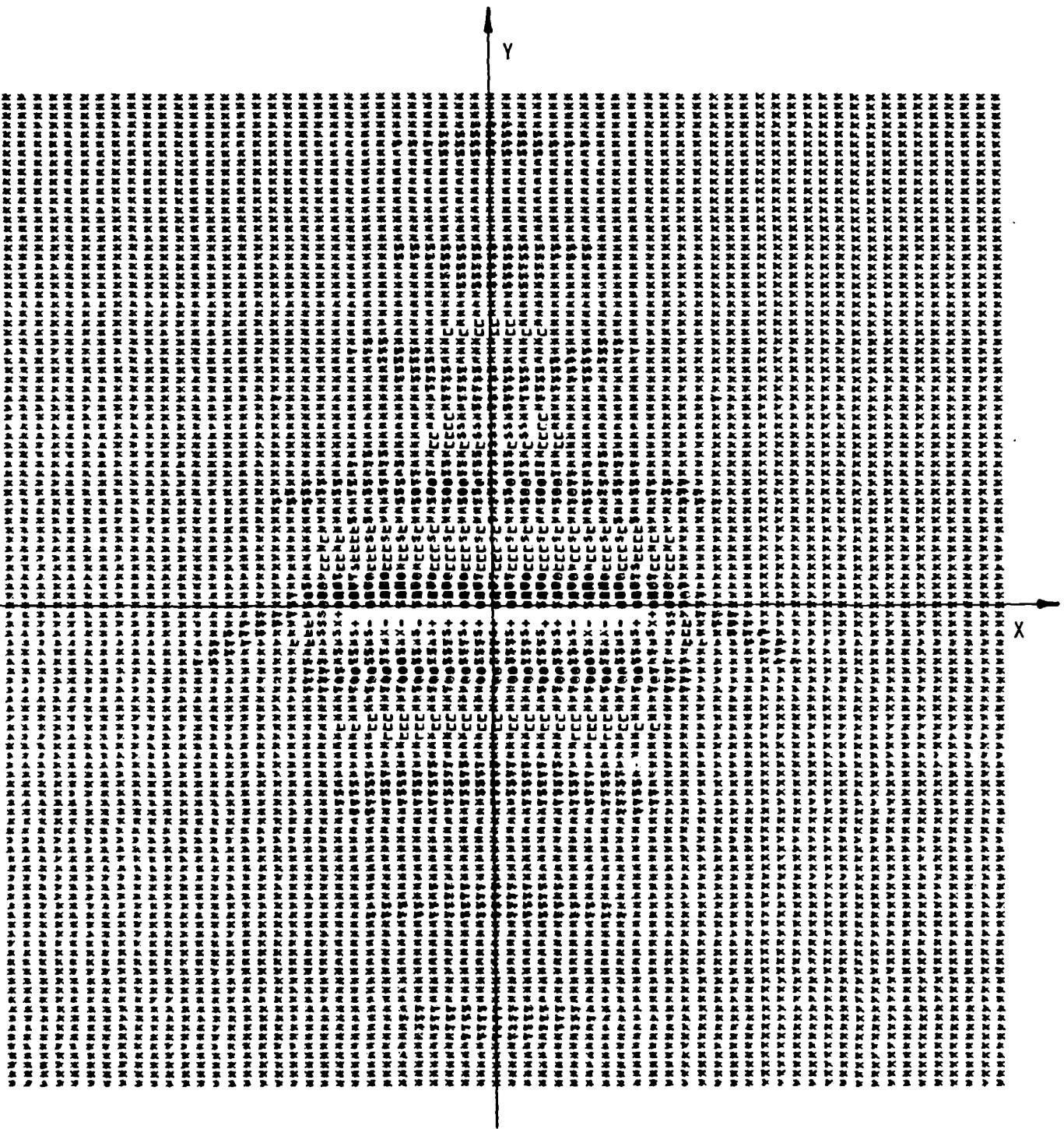


Figure 71. Image of triangular scatterer after bandpass and aspect angle filtering:  $\bar{P}_{\text{low}} = 10^{\text{th}}$  sample point,  $\bar{P}_{\text{high}} = 30^{\text{th}}$  sample point, angle=30°.

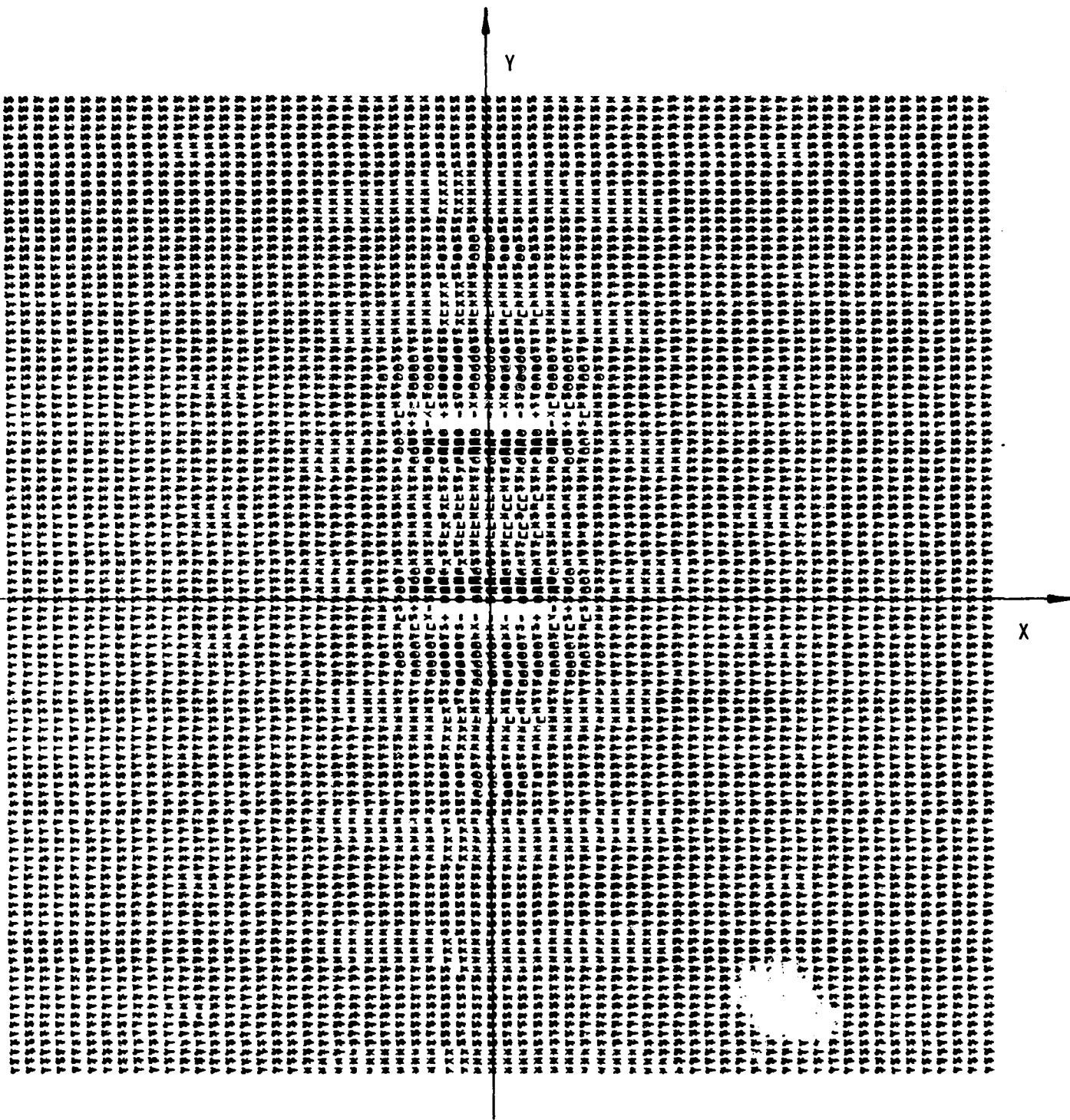


Figure 72. Image of square scatterer after bandpass and aspect angle filtering:  $\bar{P}_{low} = 10^{th}$  sample point,  $\bar{P}_{high} = 30^{th}$  sample point, angle=30°.

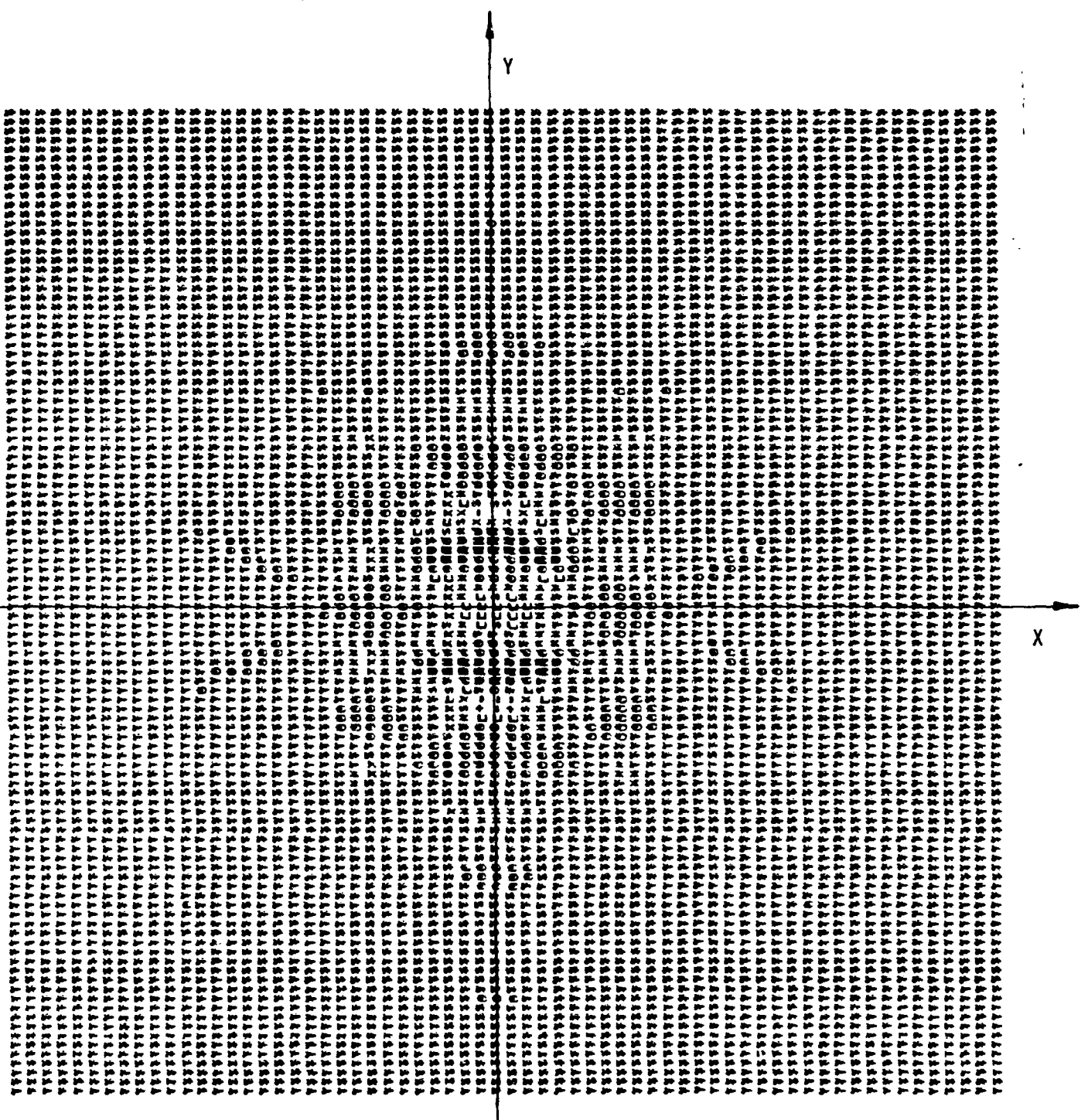


Figure 73. Image of circular scatterer after bandpass and aspect angle filtering:  $\bar{P}_{low} = 10^{th}$  sample point,  $\bar{P}_{high} = 30^{th}$  sample point, angle =  $30^\circ$ .

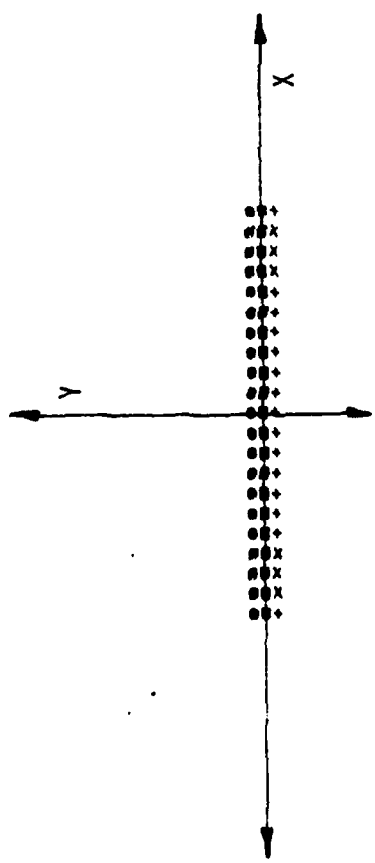


Figure 74a. Image of triangular scatterer after bandpass, aspect angle and threshold filtering:  
 $\bar{P}_{\text{low}} = 10^{\text{th}}$  sample point  
 $\bar{P}_{\text{high}} = 30^{\text{th}}$  sample point  
angle =  $30^\circ$ .

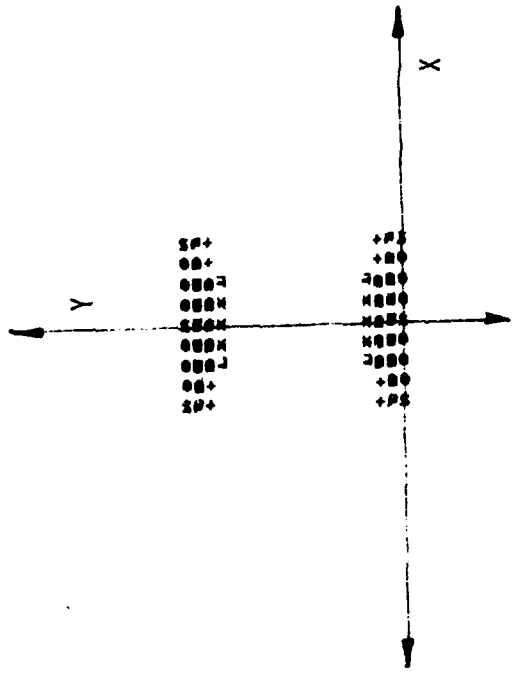


Figure 74b. Image of square scatterer after bandpass, aspect angle and threshold filtering:  
 $\bar{P}_{\text{low}} = 10^{\text{th}}$  sample point  
 $\bar{P}_{\text{high}} = 30^{\text{th}}$  sample point  
angle =  $30^\circ$ .

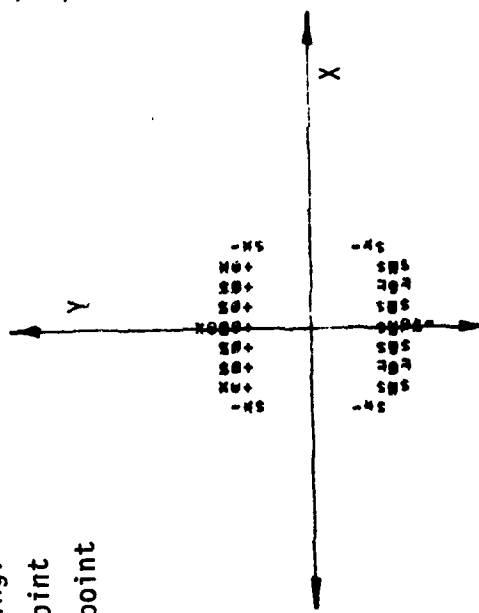


Figure 74c. Image of circular scatterer after bandpass, aspect angle and threshold filtering:  
 $\bar{P}_{\text{low}} = 10^{\text{th}}$  sample point -  $\bar{P}_{\text{high}} = 30^{\text{th}}$  sample point  
angle =  $30^\circ$ .

### F. Extension of the Aspect Window

Since ease of target identification is greatly facilitated by enlarging the viewing angle we would like to find a means for doing so by approximate analysis techniques. There may exist several techniques to arrive at a solution but in this section we have restricted ourselves to a study of the target's angular variations.

Each particular scatterer geometry has its own characteristic spectral angular variations and because the backscatter spectrum can be defined as the inverse Fourier transform of the target characteristic function we can analytically calculate the backscatter spectrum for simple shapes. The utility, of course, is that we can observe the angular scattering variations over a limited range of angles and by comparison with the calculated variations we can select the appropriate analytic function and extend the window.

For the triangular target of height  $a$  and base width of  $2b$  the calculated scattering function in polar coordinates is

$$r(p_r, \theta) = \frac{2ab}{p_r^2} \left[ \frac{\cos(a p_r \sin\theta) - \cos(b p_r \cos\theta) + i a \sin\theta \left( \frac{\sin(b p_r \cos\theta)}{b \cos\theta} - \frac{\sin(a p_r \sin\theta)}{a \sin\theta} \right)}{b^2 \cos^2\theta - a^2 \sin^2\theta} \right] \quad (20)$$

and for the square target of height  $a$  and width  $b$  centered on the origin the calculated scattering function in polar coordinates is

$$r(p_r, \theta) = \frac{\text{absin}\left(\frac{ap_r \cos\theta}{2}\right)}{\frac{ap_r \cos\theta}{2}} \frac{\sin\left(\frac{bp_r \sin\theta}{2}\right)}{\frac{bp_r \sin\theta}{2}} \quad (21)$$

and for the circular target of radius  $a$  centered on the origin the calculated scattering function in polar coordinates is

$$r(p_r, \theta) = \frac{2\pi a J_1(ap_r)}{p_r}. \quad (22)$$

This last one is independent of  $\theta$  which we expect since there are no angular variations in the geometry. Thus continuation of the angular window for a body of revolution would be a matter of continuing the constant value at that frequency. For more complex structures we must either calculate the analytic expression or lump the results of simpler geometries to get an approximate result. This work is yet to be completed but an interesting sidelight has emerged. In Figure 75 we have plotted the angular variations

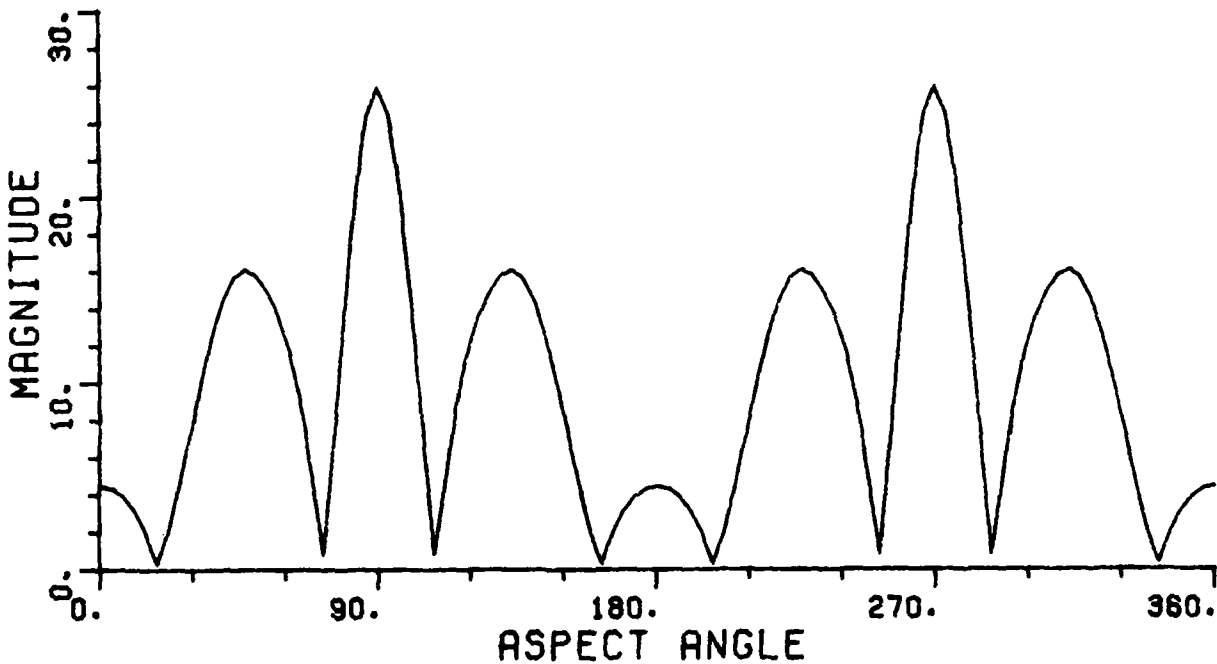


Figure 75a. Angular variation of P-space backscattering cross section corresponding to the triangular scatterer with  $\sqrt{ab}P_r = 10$ .

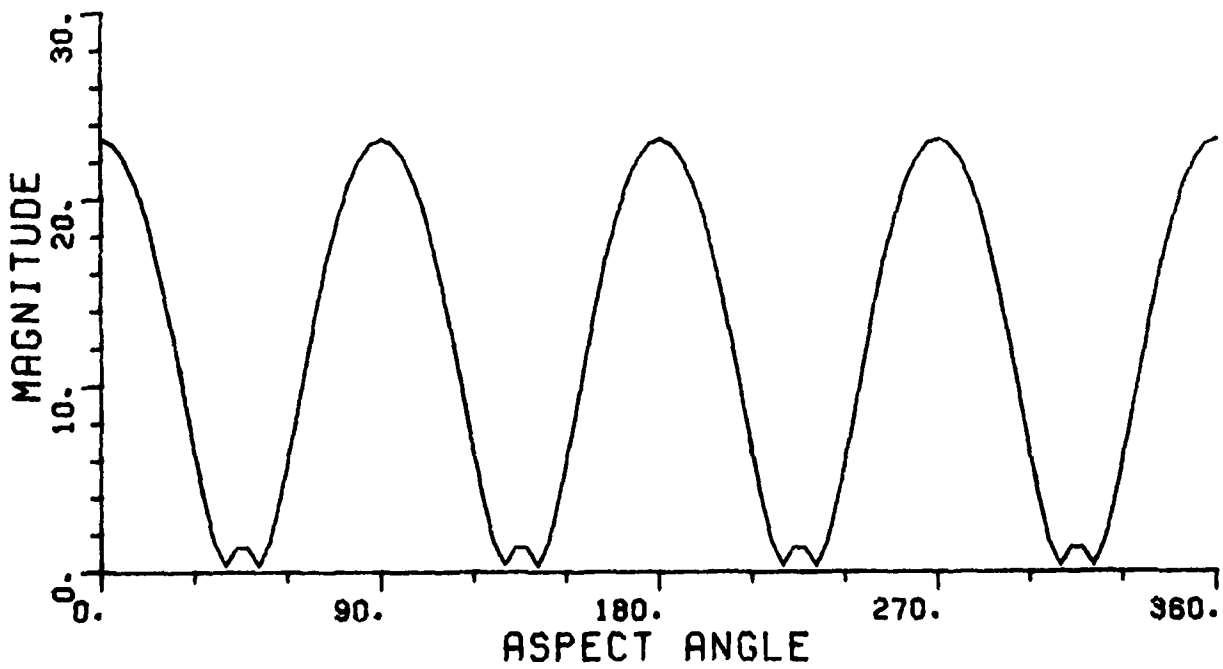


Figure 75b. Angular variation of P-space backscattering cross section corresponding to the square scatterer with  $aP_r = 10$ .

for the triangle and square at a fixed radius in P space. (The circular shape would yield a constant.) The difference in angular variation alone is sufficient to identify these two targets, and to identify the orientation of straight edges. Also the lengths of the edges appear to be proportional to the magnitude of the lobes and inversely proportional to their widths. e.g., for an infinite planar surface the 2-D scattering would be a delta function.

#### F. Conclusion

The studies and examples of this section have served to demonstrate some significant principles in identifying various scatterers. The first principle is that even though an infinite set of frequency and aspect information is required in theory to exactly image a scatterer we can produce satisfactory images with only a finite portion of the spectrum. This is true because in the physical optics approximation the surface of the scatterer gives rise to high frequency fields which are preserved when a bandpass window is applied. Thus we can determine the contour of the object by knowledge of the surface. The most significant degradation occurs in constraining aspect information but we could distinguish the three shapes even for a 30° window.

Also, we demonstrated that the angular variations are periodic functions in 360° and these yield insight into the geometry of the scatterer and suggest the possibility of extending the aspect window which could lead to better imaging.

Another principle is that by knowledge of the effects of windowing we can determine the features which are most significant, viz. the target surface scattering etc. and thereby not try to search for information that may be obscured by our choice of window. We will continue our efforts in the areas of tapering the windows, extending the windows, perfecting the threshold filtering, studying the relation of geometry to the field variations, filling in gaps in images from knowledge of the known data and determining the limits of our approximations for measured data.

#### V. SUMMARY AND CONCLUSIONS

Research has been done in three major areas during the first 12 months of this contract: Transient radar signature determination for cone-like targets, ramp response generation and limiting surface imaging, and physical optics inverse scattering. None of these efforts have been completed, but some preliminary results are available in each area.

Complex radar cross-section data have been obtained for six cone-like target shapes over a 10:1 frequency band, where cone length  $\ell$  lies in the wavelength range,  $\lambda/6 < \ell < 1.66\lambda$ . The accuracy and scope of these data are considered to be an advance in the state-of-the-art, and a paper summarizing the results will be submitted for sponsor approval in the near

future. Cross-section calculations have been made for a subset of the targets, using Rayleigh theory in the range  $\ell \leq \lambda/4$  and geometrical theory of diffraction and/or equivalent current approximation in the range  $\ell \geq \lambda$ . Both measured and calculated cross-section amplitude data have been compared to independently measured results for cone shapes nearly identical to members of our target set. Based on all results and comparisons to date, we have more confidence in the calculated data at  $\ell = \lambda/6$ , where the targets had extremely low cross-section for accurate measurements, but where the Rayleigh theory has been shown in the past to be accurate. Above  $\ell = \lambda/6$ , the measured data appear to be accurate within  $\pm 1$  dB and  $\pm 10^\circ$ . In particular, the analytic technique used here are not appropriate in the range  $\lambda/2 < \ell < \lambda$  although the measured data seem to smoothly join the calculated low-frequency (Rayleigh) and high-frequency (GTD/equivalent current) predictions.

The development and calibration of the swept-frequency system for measurements in the range  $1.33\lambda \leq \ell \leq 13.3\lambda$  has been completed. Its accuracy is consistent with the low-frequency system.

Time domain ramp response signatures have been calculated for all targets using the complex frequency-domain cross-section data. All of the waveforms exhibit approximate agreement with the target profile function (cross-section vs. distance) in their forward portion. The latter part of the time-domain waveforms show some indication of target resonance returns. However, for the approximate nose-on incidence angles of these data, it is obvious that cone resonances are not being strongly excited. The waveforms demonstrate that target detail characteristics (such as edge rounding) are not resolved, and this is consistent considering the frequency range of the current data. However, the length to base diameter ratio of the different cones, and cone size (volume) can be inferred from the waveforms.

Some ramp response waveforms were also obtained using calculated data. Approximate agreement between experimental and calculated waveforms is observed. It appears that the waveforms from GTD calculations more nearly match the measured data waveforms in the region following the base return, while the base return itself is more accurately approximated by the equivalent current calculation.

Images have been generated for the targets using the limiting surface approach with the ramp response signatures as input data. The images obviously portray the gross features of the targets. They also show surface ripples which are related to the sharp cutoff of frequency domain data. A measure of image accuracy is obtained by comparing profile function data for the image to the input profile function data from the ramp response waveforms at each aspect angle used in the image generation process. This indicator is seen to correspond roughly to subjective visual evaluation, although the visual cues used in evaluating the image seem to be related far more closely to silhouette edge and shape details rather than any area or volume parameters.

If the laser down-conversion research confirms the predicted characteristics of its electromagnetic transient response return, then the limiting surface imaging approach would be directly applicable to the return waveforms. Therefore, some research on the basic limiting surface image process has been initiated, concentrating on two areas: 1) automated iterative image improvement algorithms and 2) image confidence estimates. As the preliminary results in this report show, the relationship between image accuracy and the parameter values used in image creation is relatively well-behaved. Thus, automated iteration of these parameters has been shown to be feasible.

It has been shown in this report that for input data at a single look angle, several different images can be generated whose volume accuracy estimates are virtually identical. This is because the whole problem is "underspecified" in this case. The concept of image confidence is introduced to explain this situation. General analysis of image confidence has been initiated, but has not produced quantitative results so far. However, it is concluded that qualitatively, the image confidence is directly related to the number of input waveforms, and their spread of frequencies and aspect angles. It is also seen that the image confidence is related to the shape of the target, in ways not yet well defined.

A physical optics inverse scattering theorem has been described. A target characteristic function in real three-dimensional xyz space has been shown to be related to an electromagnetic scattering characteristic function in three-dimensional p-space (p-space having radial dimensions from an origin proportional to frequency and directional coordinates proportional to interrogating signal direction with respect to the target in xyz space) by a Fourier transform. A two-dimensional implementation of this theorem has been programmed, along with a computer intensity display algorithm. Characteristic functions for some simple ideal two-dimensional shapes have been plotted. Finally, windowing functions have been applied to the p-space data, equivalent to eliminating signature data in certain regions of look angle and frequency. The results demonstrate which features of the target are preserved and which are degraded as a function of the available signature data.

Advances to be made in each of these areas during the final months of the contract should combine to achieve all of the goals of the contract. Approximately 45% of the total funding is available to support the remaining effort.

Concerning signature data, the swept frequency measurements shall be completed giving data over an 80:1 total bandwidth. Analytical results, which become more and more accurate for these simple shapes at higher frequencies, can then be added to the measured data to obtain almost any specific frequency range desired. A technical report summarizing all data will probably be written.

Time domain transient waveforms will be generated using the higher frequency data. Transient signature characteristics relating to target resolution and target shape features will be studied.

Limiting surface images will be generated using the high-frequency signature data. Also, research in quantitative image confidence estimation, and automated iteration of the process to achieve the optimum image will be concluded. A technical report and a paper will be written in this area.

Finally, the inverse scattering research will be pursued, both to gain insight into signature feature selection for target identification and techniques for optimum identification and imaging with limited signature data. Limited three-dimensional images will be produced using this approach and the best available measured signature data. A technical report and a publication are expected to result in this area.

The technical reports and papers to be published, which represent the scientific advances made during this research, have already been discussed. The possible implementation of the results in conjunction with a LASER radar system for target imaging and identification has also been mentioned. In addition, other areas of possible application of the work to real-world radar systems are becoming evident.

The data contained in this report can be applied directly to H.F. radar signature studies for full-size targets. Thus, the research is applicable to target identification using over-the-horizon radar systems. As the results of Sections II and III show, the low frequency regime transient signatures can be used for target volume discrimination with  $\pm 10\%$  accuracy, and also for determination of target gross shape characteristics. Other studies have shown that the same conclusions apply to other shapes such as spheres, cylinders, cone-cylinders, etc. In fact, it should be feasible to characterize the exhaust plume of an ascending missile as well. In an application where actual target images are not necessary but discrimination among known targets is desired, then only a small subset of the return signature data is needed. Other studies concerning aircraft shapes have shown that HF discrimination is dependent on the selection of proper features for each target class [25]. The imaging and inverse scattering analysis of this effort is directly applicable to applied research on optimum feature selection for any set of targets.

A second area of possible application makes use of our experimental capability to obtain signature data at arbitrary bistatic angles and polarization, as well as throughout the radar frequency range. Future measurements could be made which are directly applicable to a target detection system using one or a few high-power transmitters and several dispersed, inexpensive receiver systems. Our scattering signature vs. angle analysis results in Section IV indicates that bistatic return vs. angle information in one or two narrow frequency bands may in fact be appropriate features for rapid target discrimination of cone-like targets.

## REFERENCES

- [1] Radar Target Identification, Short Course Class Notes, Ohio State University, Department of Electrical Engineering, September 1977.
- [2] C. W. Chuang and D. L. Moffatt, "Natural Resonances of Radar Targets via Prony's Method," IEEE Trans. on Aerospace and Electronic Systems, Vol. AES-12, No. 5, pp. 583-589, 1976.
- [3] Y. T. Lin and A. A. Ksieinski, "Identification of Complex Geometrical Shapes by Means of Low Frequency Radar Returns," The Radio and Electronic Engineer, Vol. 46, No. 10, October 1976. Received the Lord Brabazon Award.
- [4] Annual Report, Project 4786, August 1978, in preparation.
- [5] J. D. Young, "Target Imaging from Multiple-Frequency Radar Returns," Report 2768-6, June 1971, The Ohio State University ElectroScience Laboratory, Department of Electrical Engineering; prepared under Grant No. AFOSR-69-1710 for The Department of the Air Force. (AD 728235)
- [6] J. D. Young, "Measurement and Analysis of Spectral Signatures," Report 3387-1, July 1973, The Ohio State University ElectroScience Laboratory, Department of Electrical Engineering; prepared under Contract F04701-72-C-0180 for Space and Missile Systems Organization.
- [7] K. M. Siegel, "Far Field Scattering from Bodies of Revolution," Appl. Sci. Res., Sect. B 7, p. 293, 1958
- [8] J. W. Crispin, Jr. and K. M. Siegel, Methods of Radar Cross-Section Analysis, Academic Press, New York, N.Y., 1968.
- [9] J. B. Keller, "Backscattering from a Finite Cone," IRE Trans. on Antennas and Propagation, 8, p. 175, 1960.
- [10] W. D. Burnside and L. Peters, Jr., "Axial-radar Cross Section of Finite Cones by the Equivalent-Current Concept with Higher-Order Diffraction," Radio Science, 7, No. 10 pp. 943-948, 1972
- [11] J. E. Keys and R. I. Primich, "The Radar Cross Sections of Right Circular Metal Cones - I," Defense Res. and Telecommun. Estab. Repts., p. 1010, 1959.
- [12] E. M. Kennaugh and D. L. Moffatt, "Transient and Impulse Response Approximations," Proc. IEEE, Vol. 53, pp. 898-901, August 1965.
- [13] J. D. Young, "Target Imaging From Multiple-Frequency Radar Returns," Report 2768-6, June 1971, The Ohio State University ElectroScience Laboratory, Department of Electrical Engineering; prepared under Grant No. AFOSR-69-1710 for Air Force Office of Scientific Research.

- [14] G. B. Thomas, "Calculus and Analytic Geometry," Addison-Wesley Publishing Co., pp. 338-356, 1969.
- [15] N. N. Bojarski, "Inverse Scattering," Final Report to Contract N00019-72-6-0462, Department of Navy, Naval Air Systems Command, April 1975.
- [16] N. N. Bojarski, "Signal Processing Studies and Analysis, Vol. IV - Three Dimensional Electromagnetic Short Pulse Inverse Scattering," Contract No. AF30(602)-3961, Syracuse University Research Corporation, November 1968.
- [17] N. N. Bojarski, "Signal Processing Studies and Analysis, Vol. V - Electromagnetic Short Pulse Inverse Scattering for Discontinuities in an Area Distribution (Scattering Centers)," Contract No. AF30(602)-3961, Syracuse University Research Corporation, November 1968.
- [18] N. N. Bojarski, "Signal Processing Studies and Analysis, Vol. VII - Three-Dimensional Electromagnetic Short Pulse Inverse Scattering with Equatorial Derivative Scattering Data," Contract No. AF30(602)-3961, Syracuse University Research Corporation, November 1968.
- [19] N. N. Bojarski, "The Improvement of Electromagnetic Inverse Scattering Approximations," Contract No. AF30(602)-3961, Syracuse University Research Corporation, February 1967.
- [20] R. M. Lewis, "Physical Optics Inverse Diffraction," IEEE Trans. on Antennas and Propagation, Vol. AP-17, No. 3, pp. 308-314, May 1969.
- [21] R. D. Mager and Norman Bleistein, "An Examination of the Limited Aperture Problem of Physical Optics Inverse Scattering," Contract N0014-76-C-0039, University of Denver, Denver Research Institute, August 1977.
- [22] R. D. Mager and Norman Bleistein, "An Approach to the Limited Aperture Problem of Physical Optics Farfield Inverse Scattering," Contract N0014-76-C-0039, University of Denver, Denver Research Institute, August 1976.
- [23] W. L. Perry, "On the Bojarski-Lewis Inverse Scattering Method," IEEE Trans. on Antennas and Propagation.
- [24] J. D. Young, "Measurement and Analysis of Spectral Signatures," Report 3387-1, July 1973, The Ohio State University ElectroScience Laboratory, Department of Electrical Engineering; prepared under Contract F04701-72-C-0180 for Space and Missile Systems Organization.
- [25] A. A. Ksienki, Y. T. Lin and L. J. White, "Low Frequency Approach to Target Identification," Proc. IEEE, Vol. 63, No. 12, pp. 1651-1660, December 1975.

APPENDIX A  
TABULATIONS OF AMPLITUDE AND PHASE DATA

The amplitude (cm) and phase (deg) of each radar backscatter measurement is given in this appendix. Each table that follows gives the data for a single target along with the data from the check sphere associated with the data set. The data on the target is divided into six groups of ten measurements, where the heading of each group of ten gives the polarization (V.P. for vertical polarization and H.P. for horizontal polarization) and the aspect angle (deg) (defined earlier in this report). Each amplitude and phase value is preceded by the harmonic number for that value. The phase convention is such that items closer to the antennas will give larger phase values.

CONE #1 DATA  
INCLUDING CHECK SPHERE DATA  
CAUTION CHECK SPHERE IS FOR V.P.,(H.P., LATER)

V.P., 0 DEG. :CHECK SPHERE (P.5 INCH) (MFAS)

1 :	4.2181465E-02	1.5532619E 02
2 :	3.127420E-01	-1.7319674E 02
3 :	5.4308013E-01	-1.7610345E 02
4 :	1.2762866E 00	-1.7329914E 02
5 :	1.6557410F 00	1.6041720E 02
6 :	2.1429093E 00	1.7109999E 02
7 :	1.8950144E 00	1.4703059E 02
8 :	1.9482096E 00	1.2366621E 02
9 :	1.4677939E 00	1.4140307E 02
10 :	2.9539694E 00	1.5729568E 02

H.P., 0 DEG.

1 :	1.1643053E-01	1.4017143E 02
2 :	5.9126656F-02	-1.4036103E 02
3 :	1.421A1E9F-01	-9.9E97028E 01
4 :	4.5099743F-01	-1.2064742E 02
5 :	1.2872134F-01	-6.7429470E 01
6 :	6.764F53AF-01	-1.5079143E 02
7 :	7.0204388F-01	-1.0713046E 02
8 :	7.9780136F-01	-1.1907503E 02
9 :	6.01EU664E-01	-1.0832469E 02
10 :	8.9696986F-01	-9.9462322E 01

H.P., 10 DEG.

1 :	2.2346470F-01	-1.7322434E 02
2 :	2.1759724F-01	-1.1n28518E 02
3 :	2.4866860F-01	-1.0004952E 02
4 :	1.0214435E 00	-1.1313900E 02
5 :	4.4750490F-01	-1.1553054E 02
6 :	7.4414127F-01	-1.4705401E 02
7 :	3.5761272E-01	-8.3658917E 01
8 :	1.0278703E 00	-9.1A34118E 01
9 :	7.91A7030E-01	-7.3134941E 01
10 :	1.3140766E 00	-6.9942318E 01

H.P., 20 DEG.

1 :	1.5611149F-01	-1.6914916E 02
2 :	6.2429179F-01	-1.3207409E 02
3 :	5.9568911E-01	-1.4062137E 02
4 :	1.9025661F 00	-1.4973512E 02
5 :	9.245575AF-01	-1.5557357E 02
6 :	1.062115AF 00	-1.6859649E 02
7 :	1.3262166F 00	-8.5576217E 01
8 :	1.4176199E 00	-8.4740003E 01
9 :	1.0445059E 00	-6.7089773E 01
10 :	1.6435535F 00	-6.5922804E 01

H.P., 30 DEG.

1 :	2.4798049F-01	-1.3206329E 02
2 :	1.5226462F 00	-1.4003103E 02
3 :	1.1791057F 00	-1.6389144E 02
4 :	3.0264113E 00	-1.7435105E 02
5 :	1.7244334F 00	1.7534639E 02
6 :	1.2533609F 01	1.6340765E 02
7 :	1.70914921F 01	-8.9018378E 01
8 :	1.9107493F 00	-7.8024886E 01
9 :	1.4425042F 00	-4.3345130E 01
10 :	1.4603336AF 00	-3.6769943E 01

V.P., 0 DEG.

1 :	2.0750051F-02	1.3228789E 02
2 :	2.0581446F-01	-1.3125594E 02
3 :	3.3271704E-01	-1.0630066E 02
4 :	5.6447540F-01	-1.0794007E 02
5 :	6.8267255E-01	-1.2E65677E 02
6 :	8.40119290F-01	-1.04646001E 02
7 :	7.664152AE-01	-1.2378109E 02
8 :	9.3177963E-01	-1.467703E 02
9 :	8.9497304E-01	-1.3A937E 02
10 :	1.8092416E 00	-1.3545736E 02

V.P., 10 DEG.

1 :	1.0615599F-01	-1.546137E 02
2 :	2.2537446E-01	-1.4720510E 02
3 :	5.4743707E-01	-9.5726618E 01
4 :	4.1609287E-01	-1.0954074E 02
5 :	5.7970152F-01	-1.1522680E 02
6 :	7.28E7568F-01	-1.0985521E 02
7 :	7.4617817E-01	-1.1726741E 02
8 :	1.0599730E 00	-1.3141435E 02
9 :	8.6U26509F-01	-1.2309476E 02
10 :	1.8733066F 00	-1.1568200E 02

V.P., 20 DEG.

1 :	6.1509690F-02	-1.4A47071E 02
2 :	2.3847490E-01	-1.3636286E 02
3 :	3.2365377E-01	-1.0502346E 02
4 :	5.6286969E-01	-1.2177356E 02
5 :	5.7669798F-01	-1.2562790E 02
6 :	8.4087701E-01	-1.1A73791E 02
7 :	9.7c87782E-01	-1.3A66288E 02
8 :	1.0381121F 00	-1.5345405E 02
9 :	7.5589408E-01	-1.7226900E 02
10 :	1.6615217E 00	-1.3561913E 02

V.P., 30 DEG.

1 :	1.0031602E-01	-1.1513041E 02
2 :	3.2341482E-01	-1.5184864E 02
3 :	4.0628470F-01	-9.0746865E 01
4 :	5.9108497F-01	-1.1512548E 02
5 :	6.1849413E-01	-1.0221480E 02
6 :	8.4464315F-01	-1.2470981E 02
7 :	6.9075032E-01	-1.5225648E 02
8 :	6.9141053F-01	1.7759449E 02
9 :	9.4079433F-01	1.6012614E 02
10 :	1.6647409E 00	1.6984606E 02

CONE F2 (TRANSMITTER 1 FEB 78)  
(4:1 BLUNT CONE)

V.P., N DEG. 0.5 INCH CHECK SPHERE (MEAS)			
1 :	5.377397E-02	1.699027E 02	
2 :	2.6476318E-01	-1.6357914E 02	
3 :	6.0213606E-01	-1.7749896E 02	
4 :	1.2204210E 00	-1.7700137E 02	
5 :	1.6590817E 00	1.6679810E 02	
6 :	2.0925337E 00	1.6219742E 02	
7 :	1.9692944E 00	1.5020578E 02	
8 :	1.9265724E 00	1.4572740E 02	
9 :	2.2147335E 00	1.5891170E 02	
10 :	1.1597276E 00	1.5961635E 02	
V.P., N DEG.			
1 :	1.4567957E-01	-1.699877E 02	
2 :	4.1934945E-01	-1.3060853E 02	
3 :	6.0212048E-01	-1.3069200E 02	
4 :	6.8796963E-01	-1.3487927E 02	
5 :	1.0626778E 00	-1.6361342E 02	
6 :	1.2941164E 00	1.7753486E 02	
7 :	1.2415317E 00	-1.676616E 02	
8 :	1.357750PE 00	-1.658642E 02	
9 :	2.3163F48E 00	1.6645545E 02	
10 :	1.3eA6529F 00	-1.2462048E 02	
H.P., N DEG.			
1 :	1.5839516E-01	-7.7334645E 01	
2 :	2.5756595E-01	-1.1343035E 02	
3 :	3.5392678E-01	-8.4924548E 01	
4 :	6.4643466E-01	-8.6A596E7E 01	
5 :	6.5005961E-01	-9.7537580E 01	
6 :	1.0435944E 00	1.6670498E 02	
7 :	1.3254155E 00	-1.2513075E 02	
8 :	1.1591089F 00	-1.4229013E 02	
9 :	9.7702193E-01	-1.4071462E 02	
10 :	1.1899325E 00	-1.3396925E 02	
V.P., 10 DEG.			
1 :	2.117E764F-01	-1.1e09259E 02	
2 :	3.9494015F-01	-1.3029627E 02	
3 :	5.8115274F-01	-1.2680240E 02	
4 :	8.91209A8E-01	-1.3797545E 02	
5 :	9.5973104F-01	-1.5690475E 02	
6 :	7.9E35510E-01	-1.7796401E 02	
7 :	1.40732299E 00	-1.7424014E 02	
8 :	1.5e77426E 00	-1.7808136E 02	
9 :	2.0258990F 00	1.3918301E 02	
10 :	1.0044860F 00	1.4n87912E 02	
H.P., 10 DEG.			
1 :	3.2761618F-01	-7.1693321E 01	
2 :	3.9915611E-01	-1.1122873E 02	
3 :	5.2082893E-01	-9.5954567E 01	
4 :	7.8602334E-01	-7.5154341E 01	
5 :	9.6160516E-01	-8.7864770E 01	
6 :	1.1156076F 00	-1.6986645E 02	
7 :	1.3979096E 00	-1.0A93402E 02	
8 :	1.3551704E 00	-1.1272149E 02	
9 :	1.1677335E 00	-1.0995035E 02	
10 :	1.4952611E 00	-9.3674371E 01	
V.P., 20 DEG.			
1 :	1.4879239F-01	-1.1755669E 02	
2 :	4.3093663E-01	-1.3256627E 02	
3 :	5.6582949E-01	-1.2654397E 02	
4 :	9.8176447F-01	-1.4P91895E 02	
5 :	1.0456514E 00	-1.5861006E 02	
6 :	1.3553105E 00	1.7919098E 02	
7 :	1.44P4130E 00	1.5980546E 02	
8 :	1.4046965E 00	1.5955552E 02	
9 :	1.9877065E 00	1.221120E 02	
10 :	4.9117521E-01	8.7086529E 01	
H.P., 20 DEG.			
1 :	4.1819194E-01	-8.66573E4E 01	
2 :	9.1368799E-01	-1.2075896E 02	
3 :	8.7031339E-01	-1.0520578E 02	
4 :	1.3439956E 00	-9.1095505E 01	
5 :	1.3223475E 00	-1.0082240E 02	
6 :	1.4254285E 00	-1.7e97739E 02	
7 :	1.7457540E 00	-1.1e61102E 02	
8 :	1.4472079E 00	-1.1116242E 02	
9 :	1.2194321E 00	-1.0733212E 02	
10 :	1.7457142E 00	-9.3620369E 01	
V.P., 30 DEG.			
1 :	1.9552133F-01	-1.1844028E 02	
2 :	4.5275548E-01	-1.4P16278E 02	
3 :	6.3362652F-01	-1.1142429E 02	
4 :	1.1144649E 00	-1.3155432E 02	
5 :	9.7981626E-01	-1.3197023E 02	
6 :	1.32P290F 00	-1.7e22587E 02	
7 :	1.4061161F 00	1.7029627E 02	
8 :	1.3eL7U5E 00	-1.7433446E 02	
9 :	2.89464042F 00	1.9159571E 02	
10 :	2.4216593F 00	1.67624*5E 02	
H.P., 30 DEG.			
1 :	4.9863737F-01	-8.4218225E 01	
2 :	1.6334431E 00	-1.2439048E 02	
3 :	1.6200591E 00	-1.1495847E 02	
4 :	2.2716365E 00	-9.24660E1E 01	
5 :	2.2570742F 00	-1.0615311E 02	
6 :	1.3353400F 00	-1.6277006E 02	
7 :	2.1186228F 00	-1.2e24207E 02	
8 :	1.7d17e70E 00	-1.1044994E 02	
9 :	1.1595145E 00	-9.1250P13E 01	
10 :	1.6643744F 00	-6.4910R73E 01	

TARGET # 3  
ERIC WALTON ENTRY 1-25-78

\* V.P., 0 DEG. 0.5 INCH CHECK SPHERE

1 :	1.0225161E-01	1.7129574E 02
2 :	2.6574430E-01	-1.7479484E 02
3 :	6.7806807E-01	-1.7920235E 02
4 :	1.2667762E 00	-1.7060916E 02
5 :	1.5995999E 00	1.7060093E 02
6 :	1.9415635E 00	1.7420481E 02
7 :	1.857E139F 00	1.5549259E 02
8 :	2.007A196F 00	1.5A90246E 02
9 :	0.0000000E-01	4.4999999E 01
10 :	0.0000000F-01	4.4999999E 01

\* H.P., 0 DEG.

1 :	1.82E9056E-01	-1.4004721F 02
2 :	9.7156555F-02	-1.0648198E 02
3 :	1.7218791E-01	-5.1245037E 01
4 :	2.2736606E-01	-6.9083949E 01
5 :	1.7944439E-01	-7.5044850E 01
6 :	6.50664901F-01	-1.7432577E 02
7 :	3.4553193E-01	-1.0065130E 02
8 :	4.2643E67E-01	-1.2740535E 02
9 :	5.6015714F-01	-1.3186069F 02
10 :	7.7464123E-01	-9.9212E4E 01

\* H.P., 10 PER.

1 :	<5.119887E-01	-1.3433E59F 02
2 :	2.1924304F-01	-1.0485641E 02
3 :	3.0956469F-01	-8.2407727E 01
4 :	3.8671988E-01	-5.8186330E 01
5 :	5.4537E20F-01	-8.1475240E 01
6 :	5.4274674F-01	-1.5962494F 02
7 :	6.6116447E-01	-8.6A35426E 01
8 :	7.2511555E-01	-9.2324445E 01
9 :	6.5076064E-01	-8.8067752E 01
10 :	1.1140502E 00	-5.76751F6E 01

\* H.P., 20 DEG.

1 :	3.5320529F-01	-1.5024529F 02
2 :	9.2877563F-01	-1.4544434F 02
3 :	5.7227940F-01	-8.9765878E 01
4 :	1.1663316E 00	-6.4077491E 01
5 :	9.9774657F-01	-1.02363905E 02
6 :	1.0708236E 00	1.7133229E 02
7 :	1.2655792F 00	-9.7880817E 01
8 :	1.0471214F 00	-9.61904E66E 01
9 :	8.0993958E-01	-9.4066578E 01
10 :	1.5711644F 00	-5.7307568E 01

\* H.P., 30 DEG.

1 :	6.22D0467E-01	-1.4047953F 02
2 :	1.1502202F 00	1.3064626F 02
3 :	1.22300160E 00	-1.3561466F 02
4 :	1.5725004F 00	9.8113747E 01
5 :	1.7145292E 00	-1.1773270F 02
6 :	1.1435375F 00	1.5098741E 02
7 :	1.9038190F 00	1.1435678E 02
8 :	1.49437E3F 00	-1.061F262F 02
9 :	1.0401782F 00	-8.9973E93E 01
10 :	1.7524059F 00	-5.6478108E 01

\* V.P., 0 DEG.

1 :	6.3467265F-02	6.4930649E 01
2 :	1.6259344E-01	-1.4447242E 02
3 :	2.5E50824F-01	-1.1906805E 02
4 :	3.3752317E-01	-1.1637504E 02
5 :	4.7474323E-01	-1.4526344E 02
6 :	5.8551453F-01	-1.2204095E 02
7 :	5.1650567F-01	-1.3406099E 02
8 :	6.4540524E-01	-1.4116526E 02
9 :	1.3296464E 00	-1.6449390E 02
10 :	1.2473069F 00	-1.4359664E 02

\* V.P., 10 DEG.

1 :	5.4706741F-02	1.4084202E 02
2 :	1.9E13662E-01	-1.5592949E 02
3 :	2.7466515E-01	-9.99E1497E 01
4 :	2.6980652E-01	-1.1891535E 02
5 :	3.5515245E-01	-1.2256443E 02
6 :	6.3730936F-01	-1.2369076E 02
7 :	5.5401656E-01	-1.0849282E 02
8 :	8.1365361E-01	-1.0231809E 02
9 :	9.9510186E-01	-1.4632552E 02
10 :	8.7617438E-01	-9.2966846E 01

\* V.P., 20 DEG.

1 :	1.4593891E-02	4.7276877E 01
2 :	1.8426152F-01	-1.5554033E 02
3 :	2.4961421E-01	-1.1C76553E 02
4 :	3.7005528E-01	-1.251157E 02
5 :	3.9264401E-01	-1.3142072E 02
6 :	5.3751272F-01	-1.3E84049E 02
7 :	4.1763663F-01	-1.1510666E 02
8 :	7.8673914E-01	-1.1102219E 02
9 :	1.2086309E 00	-1.5057647E 02
10 :	1.3214983E 00	-1.3341301E 02

\* V.P., 30 DEG.

1 :	5.0447919E-02	-3.6315328E 01
2 :	2.9292543F-01	-1.66774E2E 02
3 :	3.0990477E-01	-8.1676801E 01
4 :	3.9625618E-01	-1.24464A7E 02
5 :	4.1266110E-01	-9.2063125E 01
6 :	5.6231283E-01	-1.2081F70E 02
7 :	3.7767166F-01	-1.1620064E 02
8 :	8.6069511F-01	-7.1133337E 01
9 :	5.1962692E-01	-1.3496143E 02
10 :	1.6561631F 00	-1.2398019E 02

## CONE # 4 (TRANSFERRED 1 FEB. 78)

V.P., 0 DEG. 0.5 INCH CHECK SPHERE (NEAS)

1 :	7.9459446E-02	1.5170222E 02
2 :	2.5792183E-01	-1.7669884E 02
3 :	6.7677428E-01	-1.7960018E 02
4 :	1.1871166E 00	-1.7449459E 02
5 :	1.6385706E 00	1.6269843E 02
6 :	2.2090732E 00	1.7029529E 02
7 :	1.9741401E 00	1.5018832E 02
8 :	1.8864052E 00	1.3629909E 02
9 :	1.4648024E 00	1.5100846E 02
10 :	2.9614980E 00	1.6080625E 02

\* V.P., 0 DEG.

1 :	1.1221427E-01	-1.3561700E 02
2 :	1.7477187E-01	-9.4045646E 01
3 :	3.7477474E-01	-8.7837029E 01
4 :	6.1301428E-01	-3.7743325E 01
5 :	5.1233451E-01	-9.1334256E 01
6 :	6.9664166E-01	-4.7558685E 01
7 :	5.8571366E-01	-6.1064575E 01
8 :	6.6161494E-01	-6.2677343E 01
9 :	5.0781052E-01	-4.2609822E 01
10 :	1.1439686E 00	-3.1666384E 01

\* V.P., 10 DEG.

1 :	1.6437445E-01	-1.1504259E 02
2 :	2.2619320E-01	-1.3229133E 02
3 :	3.4613161E-01	-1.0000321E 02
4 :	4.5567917E-01	-1.2733450E 02
5 :	4.7599110E-01	-1.2360907E 02
6 :	6.0354090E-01	-1.2271294E 02
7 :	4.9645347E-01	-2.2099458E 01
8 :	6.3224051E-01	-3.4586008E 01
9 :	6.8419560E-01	3.8926129E 00
10 :	1.1025213E 00	2.0425369E 01

\* V.P., 20 DEG.

1 :	6.9444089E-02	-6.0167672E 01
2 :	2.232134F-01	-1.4014629E 02
3 :	3.0343801E-01	-1.0320884E 02
4 :	4.8730664E-01	-1.1933898E 02
5 :	5.4290439E-01	-1.2981876E 02
6 :	6.00441779E-01	-1.3627448E 02
7 :	5.348F-191E-01	-1.0947646E 01
8 :	6.7622651E-01	-3.2347444E 01
9 :	6.7620452E-01	9.9568492E 00
10 :	1.2116595E 00	2.1042484E 01

\* V.P., 30 DEG.

1 :	1.2049403E-01	-8.1024346E 01
2 :	3.0391515E-01	-1.5024302E 02
3 :	4.1656730E-01	-8.5954458E 01
4 :	5.6420391E-01	-1.0002244E 02
5 :	6.5129403E-01	-9.6219270E 01
6 :	7.3325506E-01	-1.3682937E 02
7 :	5.3160260E-01	2.2424347E 01
8 :	7.906794F-01	-1.5676518E 01
9 :	3.5515766E-01	3.0694467E 01
10 :	1.1705402E 00	3.9860242E 01

H.P., 0 DEG.

1 :	7.9216295E-02	-1.2000222E 02
2 :	1.0566308E-01	-8.5043026E 01
3 :	2.2536337E-01	-4.2277443E 01
4 :	3.8200761E-01	-2.3563249E 01
5 :	4.0679608E-01	-1.8076107E 01
6 :	4.9302051E-01	-1.1567641E 02
7 :	7.9360906E-01	-3.4090925E 01
8 :	8.2436279E-01	-3.9857713E 01
9 :	7.3119119E-01	-1.9221430E 01
10 :	9.5703450E-01	-1.40355967E-01

\* H.P., 10 DEG.

1 :	7.6623652E-02	-1.2976446E 02
2 :	2.5072486E-01	-9.4369829E 01
3 :	3.8181322E-01	-6.3369411E 01
4 :	5.4107732E-01	-3.2169895E 01
5 :	5.6641362E-01	-3.9894107E 01
6 :	4.8367799E-01	-9.5138158E 01
7 :	7.1954367E-01	-1.1111677E 01
8 :	8.3721029E-01	-2.3365326E 01
9 :	7.5332107E-01	4.5215394E 00
10 :	8.9102713E-01	2.8081721E 01

\* H.P., 20 DEG.

1 :	2.0360113F-01	-1.0410847E 02
2 :	7.2598621E-01	-1.1100707E 02
3 :	7.0439607E-01	-9.3442581E 01
4 :	1.0297832E 00	-6.4528479E 01
5 :	8.4707639F-01	-7.2886344E 01
6 :	6.3466564E-01	-1.4221700E 02
7 :	6.2405190F-01	-6.0104984E 01
8 :	7.5558903E-01	-3.8014248E 01
9 :	2.9665326E-01	1.6003688E 01
10 :	3.2641914E-01	5.2976749E 01

\* H.P., 30 DEG.

1 :	3.2569347E-02	-1.1164249E 02
2 :	1.3566823E 00	-1.1431422E 02
3 :	1.4c77461E 00	-1.0810788E 02
4 :	1.9771973E 00	-8.1421639E 01
5 :	1.8021695F 00	-9.6377606E 01
6 :	5.3297414F-01	-1.4966447E 02
7 :	1.0551327E 00	-1.2202776E 02
8 :	6.9630586F-01	-8.00666709E 01
9 :	1.6942454F-01	5.6047215E 01
10 :	5.2101115F-01	1.7526474E 02

## ITEM 5 V.P. ERIC WALTON 1:2:7d

V.P., 0 DEG. CHECK SPHFR ( 0.5 INCH-MEAS)

1 :	5.8945687F-02	1.5319616E 02
2 :	2.7295963E-01	-1.794983E 02
3 :	6.0587509E-01	-1.7790144E 02
4 :	1.3050779F 00	-1.7A55863E 02
5 :	1.6687496F 00	1.6601107E 02
6 :	2.3571938F 00	1.7089002E 02
7 :	1.80566470E 00	1.447733E 02
8 :	1.8459124E 00	1.3048938E 02
9 :	1.5707035E 00	1.4368735E 02
10 :	3.9324622E 00	1.4169572E 02

\* V.P., 0 DEG.

1 :	9.7910120E-02	-1.2203566E 02
2 :	6.8257229E-02	-7.9n59324E 01
3 :	5.1746407E-02	-1.350467E 02
4 :	3.008F0169F-01	-1.4129n67E 02
5 :	2.65502223F-01	-1.1599930E 02
6 :	2.6910377E-01	-1.3000867E 02
7 :	3.4321250F-01	-1.6814777E 02
8 :	4.7660058F-01	-1.6311521E 02
9 :	5.2591620E-01	1.6274405E 02
10 :	2.1031132E 00	-1.64t2938E 02

H.P., 0 DEG.

1 :	5.7146321F-02	-1.0103601E 02
2 :	1.3494556F-01	1.2466888E 02
3 :	5.49444693F-02	4.1712823E 01
4 :	9.3407e42F-02	4.4046929E 01
5 :	2.1571713E-01	-6.6452308E 01
6 :	9.7932501F-02	-1.767841E 02
7 :	4.4029732E-01	-8.6451410E 01
8 :	1.5363764E-01	-6.1663820E 01
9 :	2.6524292F-01	1.6511994E 02
10 :	5.6218286E-01	-1.2e09071E 02

\* V.P., 10 DEG.

1 :	5.423E529F-02	-1.5634847E 02
2 :	2.05E6143F-02	-1.4219578E 02
3 :	4.8962E27F-02	-2.1960564E 01
4 :	1.24003756F-01	-1.66250n05E 02
5 :	2.594E533E-01	-7.8631992E 01
6 :	2.6245855E-01	-1.31E3271E 02
7 :	5.2386548F-01	-1.7259679E 02
8 :	6.6791534F-01	-1.4660036E 02
9 :	5.0613272E-01	-1.7A11E85E 02
10 :	2.2209292E 00	-1.5742664E 02

\* H.P., 10 DEG.

1 :	4.7295157E-02	-7.4582744E 01
2 :	2.8102974F-01	-1.1320105E 02
3 :	1.9036857F-01	-1.3x64822E 02
4 :	4.2329550E-01	-1.026U949E 02
5 :	6.5163140F-01	-1.4476177E 02
6 :	5.2843587F-01	-1.6262915E 02
7 :	4.7021459F-01	-7.6916193E 01
8 :	3.4263116E-01	-5.8868303E 01
9 :	2.7758799F-01	-1.2692029E 02
10 :	6.4435338E-01	-7.4824550E 01

\* V.P., 20 DEG.

1 :	6.2505907E-02	-1.0525757E 02
2 :	1.4343360E-01	1.1617306E 02
3 :	5.9412419F-02	-1.0536492E 01
4 :	3.4962699E-01	-1.5264767E 02
5 :	2.6420044F-01	-7.8A09206E 01
6 :	2.4761649E-01	-1.5077294E 02
7 :	5.2675250F-01	1.4941685E 02
8 :	7.3297395E-01	-1.5228207E 02
9 :	3.7416110E-01	1.7106624E 02
10 :	2.4469499E 00	-1.749620E 02

\* H.P., 20 DEG.

1 :	2.6E93012E-01	-1.0284143E 02
2 :	1.0615711F 00	-1.1640310E 02
3 :	7.3176940E-01	-1.5627430E 02
4 :	1.3423344F 00	-1.2361723E 02
5 :	1.6124422F 00	-1.7396822E 02
6 :	1.1367594E 00	1.5656227E 02
7 :	1.1963192E 00	-1.0377805E 02
8 :	9.1E73090E-01	-9.2333968E 01
9 :	6.4421536F-01	-9.9406843E 01
10 :	1.4737639E 00	-7.7971535E 01

\* V.P., 30 DEG.

1 :	1.035E157F-01	-9.5767719E 01
2 :	7.5637937F-02	-1.7A12024E 02
3 :	1.7531430F-01	-3.9887207E 01
4 :	2.6401526E-01	-1.3739942E 02
5 :	5.5366577F-01	-6.5039580E 01
6 :	1.4553771F-01	-1.7113417E 02
7 :	6.997E74PF-01	1.3663900E 02
8 :	6.77372e4F-01	-1.5354577E 02
9 :	4.2u974e1F-01	-1.6e85003E 02
10 :	2.0044156E 00	-1.6703143E 02

\* H.P., 30 DEG.

1 :	4.48C2705F-01	-1.1854896E 02
2 :	2.45542P4F 00	-1.311340E 02
3 :	1.5318982E 00	-1.6482977E 02
4 :	2.5936985E 00	-1.3536610E 02
5 :	3.1401647E 00	1.6933646E 02
6 :	1.8126149E 00	1.1805614E 02
7 :	2.3402097F 00	-1.2325240E 02
8 :	2.0017A75E 01	-1.1306279E 02
9 :	1.5546484F 00	-6.9937225E 01
10 :	2.4142900E 00	-6.2553108E 01

CONE NUMBER 6  
DATA FOR RAMP RESPONSE CALCULATIONS

AMPLITUDE (CM) AND PHASE (DEG)

V.P., 0 DEG. 0.5 INCH CHECK SPHERE (MEASURED)

1 :	1.0568722F-01	-1.7019977E 02
2 :	2.2742802F-01	-1.7340045E 02
3 :	6.4224841F-01	-1.7540123E 02
4 :	1.2170458E 00	-1.7019475E 02
5 :	1.7470788E 00	1.7080093E 02
6 :	2.0467486E 00	1.7369906E 02
7 :	1.9672041F 00	1.5269716E 02
8 :	1.8943631F 00	1.5119722E 02
9 :	1.7608822F 00	1.6308041E 02
10 :	0.3000000F-01	4.4999999E 01

V.P., 0 DEG.

1 :	2.6444258F-01	-1.5136042E 02
2 :	5.3769736F-01	-1.3639566E 02
3 :	1.0903910E 00	-1.3452829E 02
4 :	1.6103028F 00	-1.3060121E 02
5 :	2.0764446E 00	-1.7169841E 02
6 :	2.1518609E 00	-1.7540200E 02
7 :	2.00112142E 00	-1.700399E 02
8 :	1.9487085F 00	1.7609188E 02
9 :	3.0176186E 00	-1.6095645E 02
10 :	2.2129270F-01	5.7198508E 01

H.P., 0 DEG.

1 :	2.3279253E-01	-1.7070541E 02
2 :	5.9377972E-01	-1.3759953E 02
3 :	6.0958206F-01	-1.1628115E 02
4 :	1.4497563E 00	-1.0528066E 02
5 :	1.4455500F 00	-1.2253066E 02
6 :	2.0035797E 00	1.4010146E 02
7 :	2.1591788E 00	-1.6869263E 02
8 :	2.0263107E 00	1.7009279E 02
9 :	1.2787604E 00	-1.6550008E 02
10 :	2.0495159F 00	-1.4991649E 02

V.P., 10 DEG.

1 :	2.6419140F-01	-1.4154019E 02
2 :	5.0593620F-01	-1.4060443E 02
3 :	1.0511538F 00	-1.2792436E 02
4 :	1.6065424F 00	-1.3479442E 02
5 :	1.6452916F 00	-1.6360276E 02
6 :	2.2573246E 00	-1.6939292E 02
7 :	2.0013792F 00	-1.6832289E 02
8 :	2.0513047F 00	-1.6869006E 02
9 :	2.9532F32F 00	-1.5390043E 02
10 :	2.7066735F-01	1.3049960E 02

H.P., 10 DEG.

1 :	1.8276262F-01	-1.6990223E 02
2 :	7.6212994F-01	-1.2726640E 02
3 :	1.0382336F 00	-1.0366322E 02
4 :	1.6484479E 00	-9.0204187E 01
5 :	1.7657573E 00	-1.0209918E 02
6 :	2.0161094F 00	1.6564066E 02
7 :	2.0317977F 00	-1.4534544E 02
8 :	1.9542360F 00	-1.6116666E 02
9 :	1.2942769E 00	-1.4442714E 02
10 :	1.3994549E 00	-1.1488404E 02

V.P., 20 DEG.

1 :	2.7518114F-01	-1.3704925E 02
2 :	6.1315760E-01	-1.4400617E 02
3 :	1.1063932F 00	-1.3589149E 02
4 :	1.6722446F 00	-1.4192546E 02
5 :	1.9632824E 00	-1.6566872E 02
6 :	2.2455213F 00	-1.7539776E 02
7 :	1.9559989F 00	1.6928194E 02
8 :	1.8556017F 00	1.6656219E 02
9 :	2.7415946F 00	1.6019816E 02
10 :	5.0152213F-01	1.2444819E 02

H.P., 20 DEG.

1 :	2.4015498E-01	-1.0918364E 02
2 :	1.2651505F 00	-1.2763061E 02
3 :	1.48464500E 00	-1.0870310E 02
4 :	2.1222532E 00	-9.1918375E 01
5 :	2.1516735E 00	-1.0025184E 02
6 :	2.3469752E 00	1.7553135E 02
7 :	2.2643222F 00	-1.2392208E 02
8 :	1.7058688E 00	-1.3249472E 02
9 :	1.3644922E 00	-1.1560812E 02
10 :	1.4539196F 00	-7.3031447E 01

V.P., 30 DEG.

1 :	2.8913641F-01	-1.2762483E 02
2 :	7.0960998F-01	-1.4647388E 02
3 :	1.1776489E 00	-1.1847774E 02
4 :	1.7377863F 00	-1.3240344E 02
5 :	1.0435536F 00	-1.40446641E 02
6 :	2.2915841F 00	-1.5481523E 02
7 :	2.1501426F 00	1.6472642E 02
8 :	1.4616506F 00	1.6255020E 02
9 :	5.01213126F 00	1.5468078E 02
10 :	5.0766870F-01	3.9968879E 01

H.P., 30 DEG.

1 :	4.7700880F-01	-1.4707448E 02
2 :	1.9168664F 00	-1.2479115E 02
3 :	2.3464634E 00	-1.1238906E 02
4 :	2.4992627E 00	-9.5576132E 01
5 :	2.3547644F 00	-8.2381506E 01
6 :	1.8791036F 00	-1.7416129E 02
7 :	2.4631402F 00	-9.6499610E 01
8 :	1.0155815F 00	-1.1458119E 01
9 :	1.2003287E 00	-5.9220119E 01
10 :	1.5514271F 00	-1.9450037E 01

APPENDIX B  
RAMP RESPONSE WAVEFORMS FOR TARGET SET

The following waveforms are ramp response signatures for each of the targets used in this study. Each graph contains ramp responses for four look angles:  $\phi=0, 10, 20$  and  $30^\circ$ . The dashed curves are the ramp responses as measured. The solid curves have been altered by setting the first harmonic phase terms to  $180^\circ$ . Graphs are included for vertical and horizontal polarization.

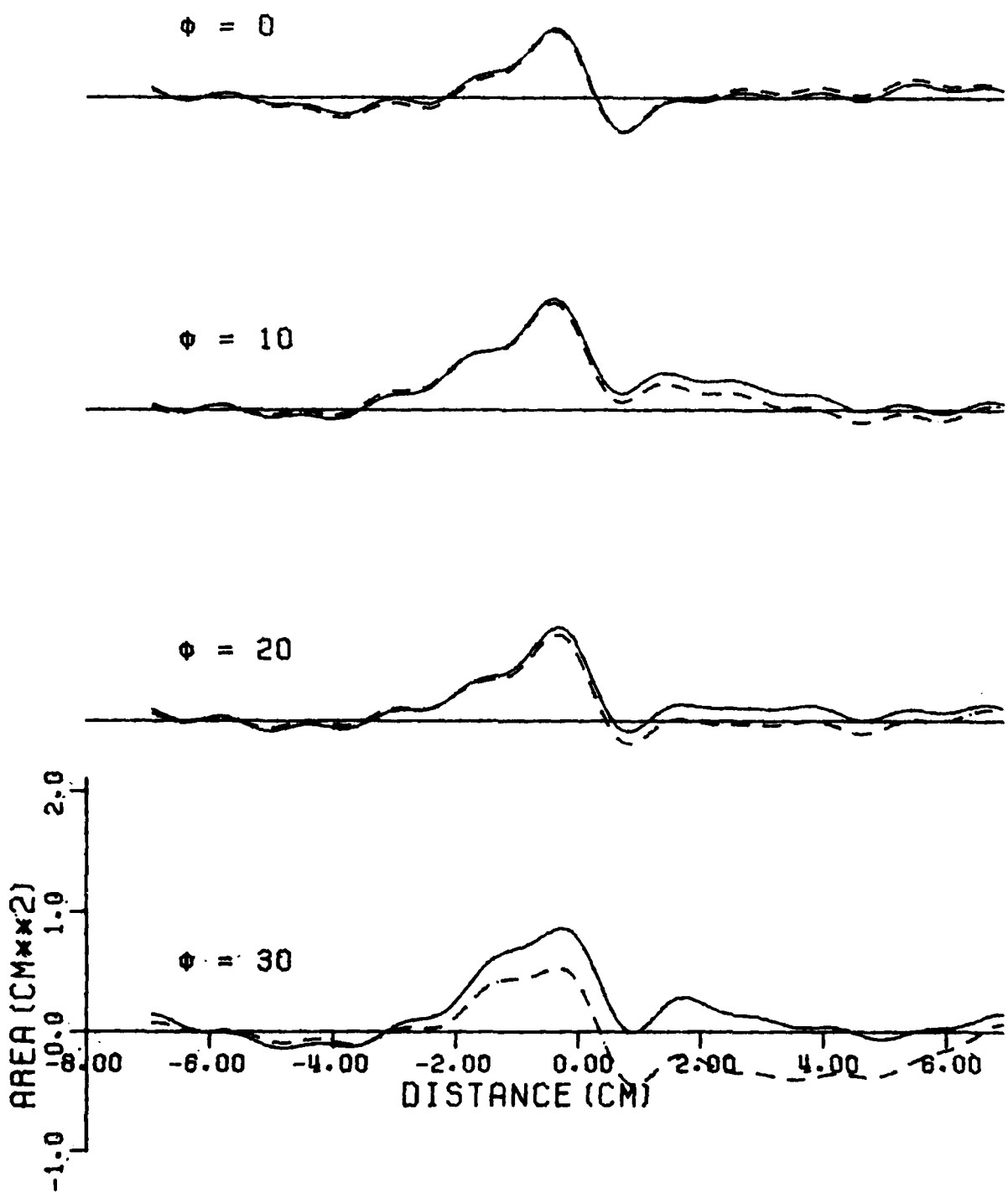


Figure B-1. Target 1 vertical polarization ramp responses.

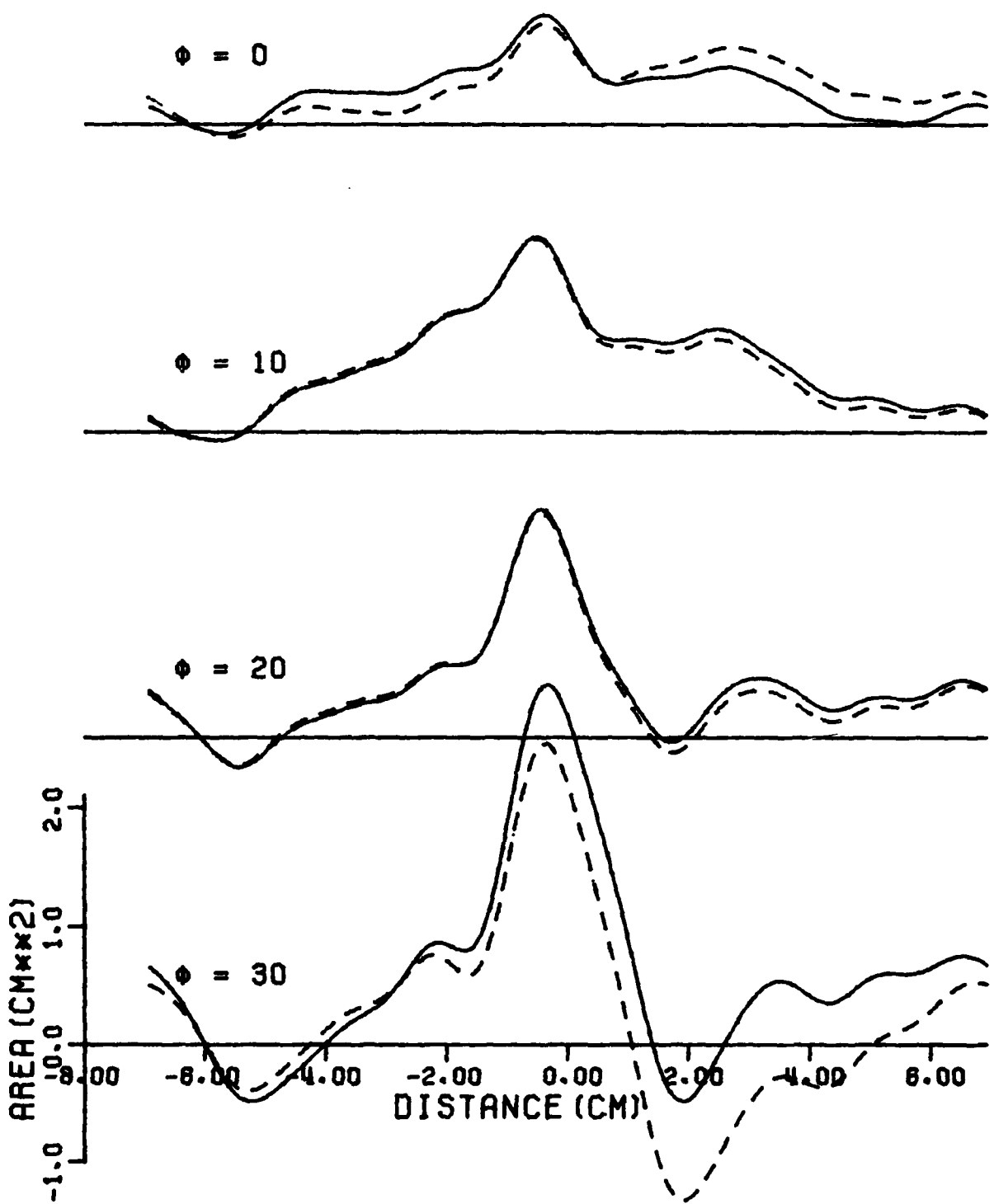


Figure B-2. Target 1 horizontal polarization ramp responses.

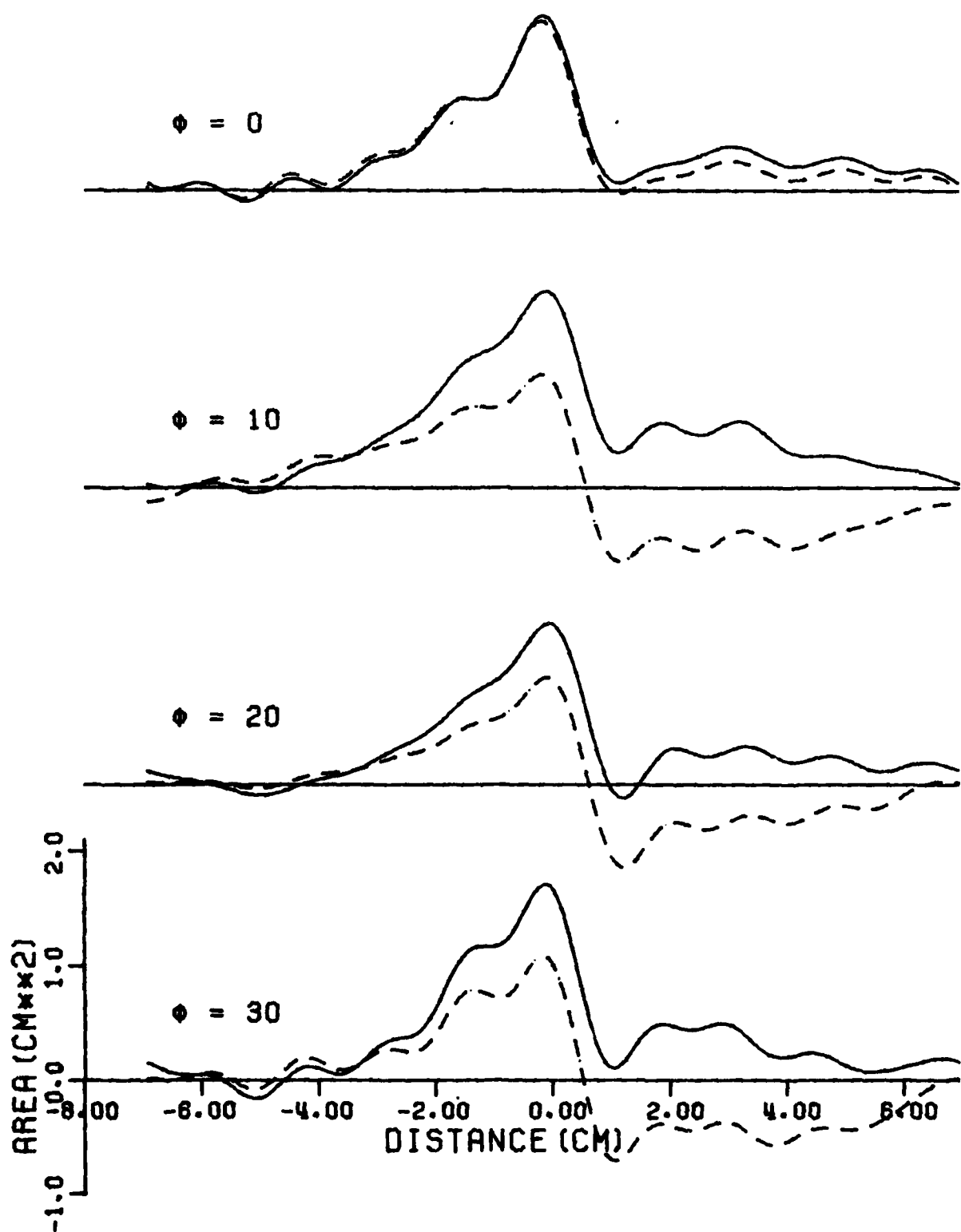


Figure B-3. Target 2 vertical polarization ramp responses.

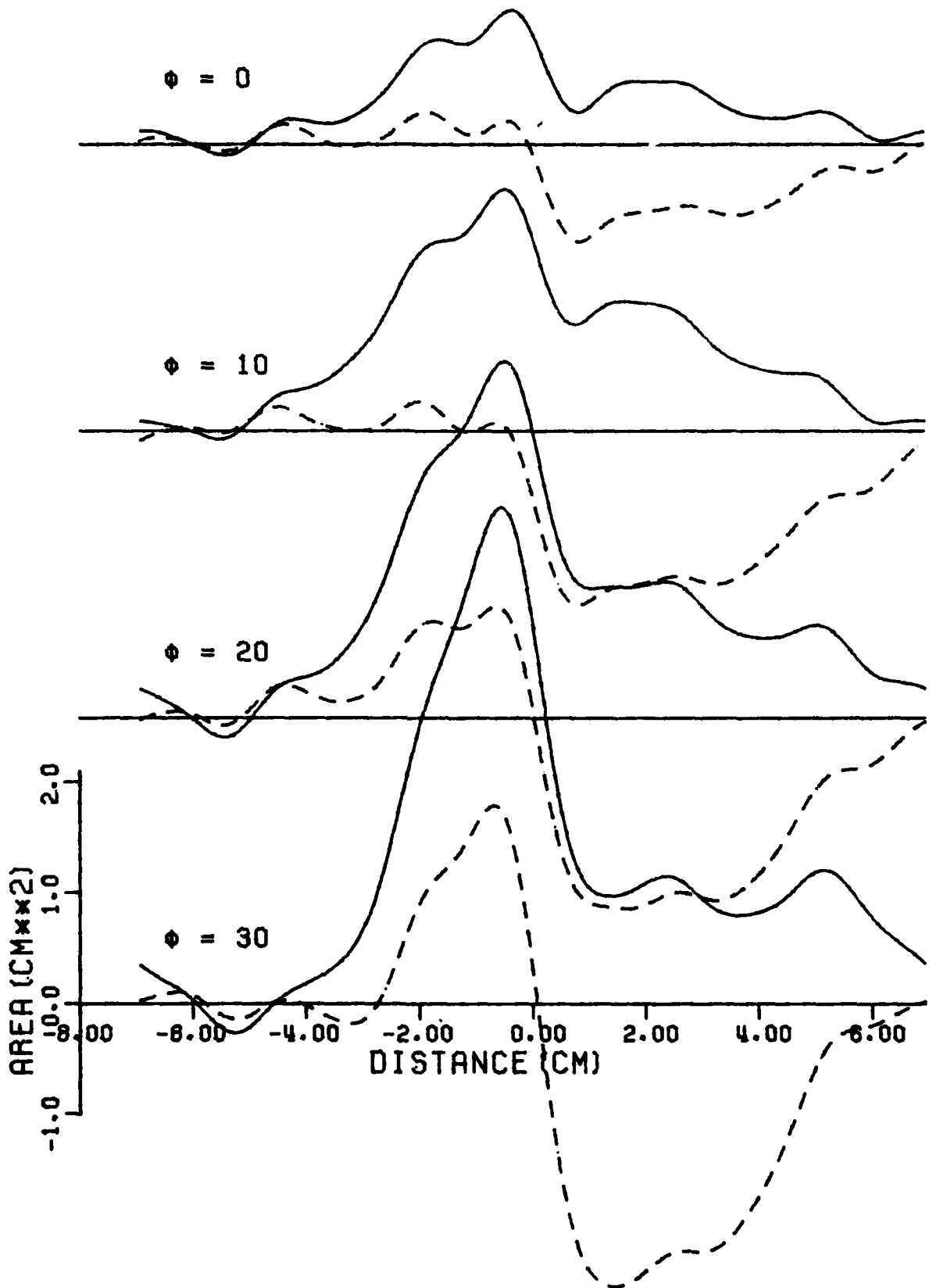


Figure B-4. Target 2 horizontal polarization ramp responses.

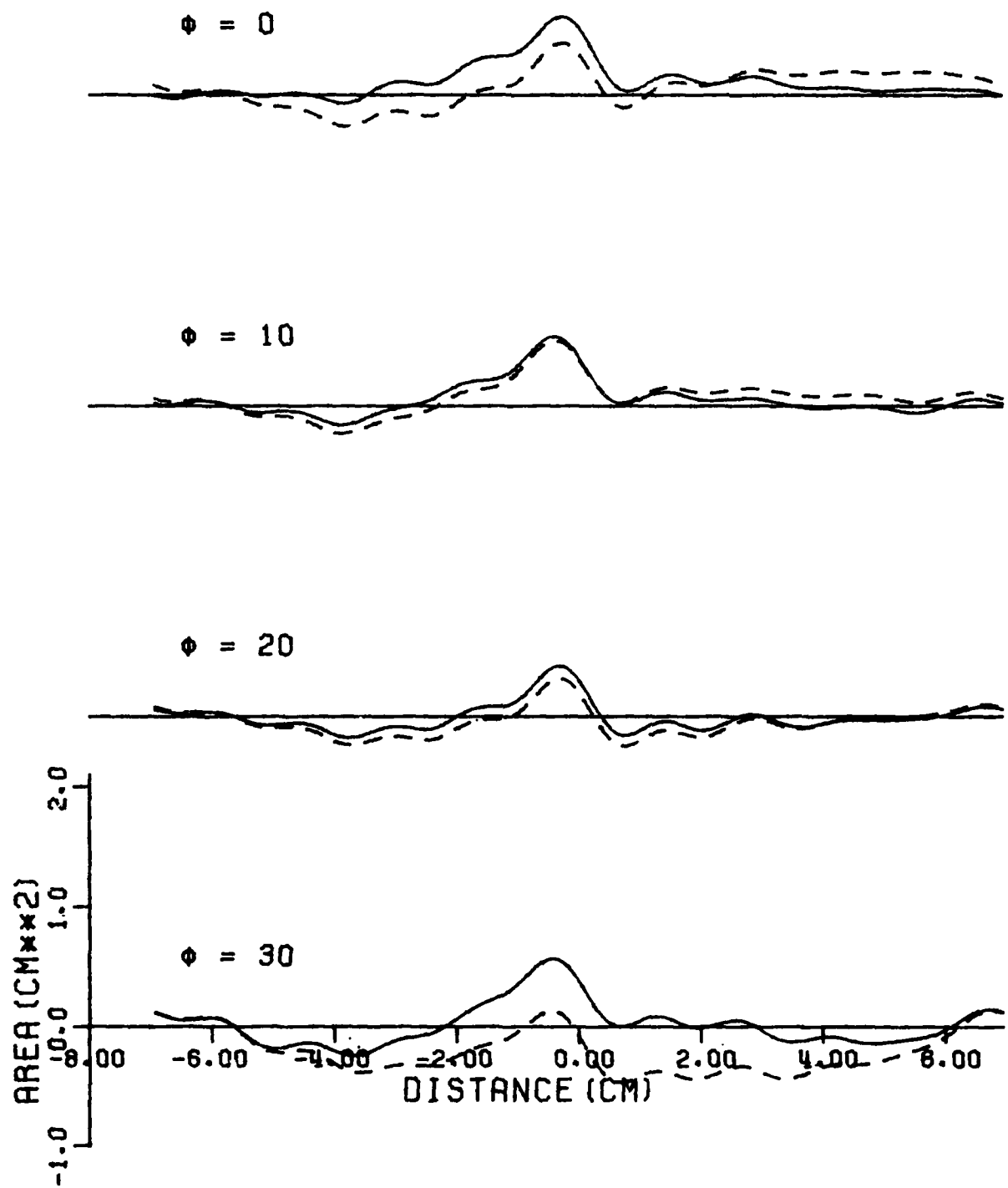


Figure B-5. Target 3 vertical polarization ramp responses.

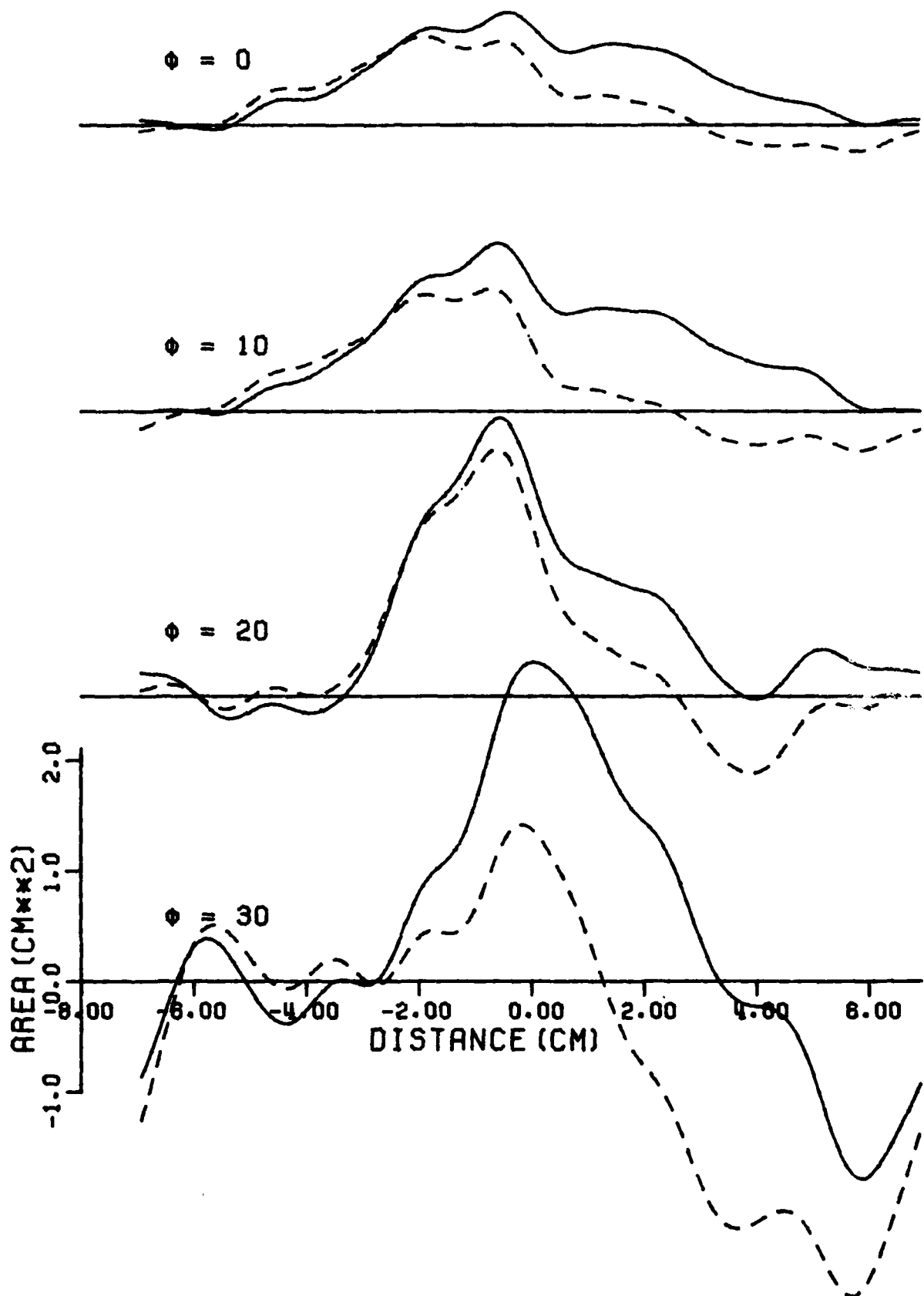


Figure B-6. Target 3 horizontal polarization ramp responses.  
117

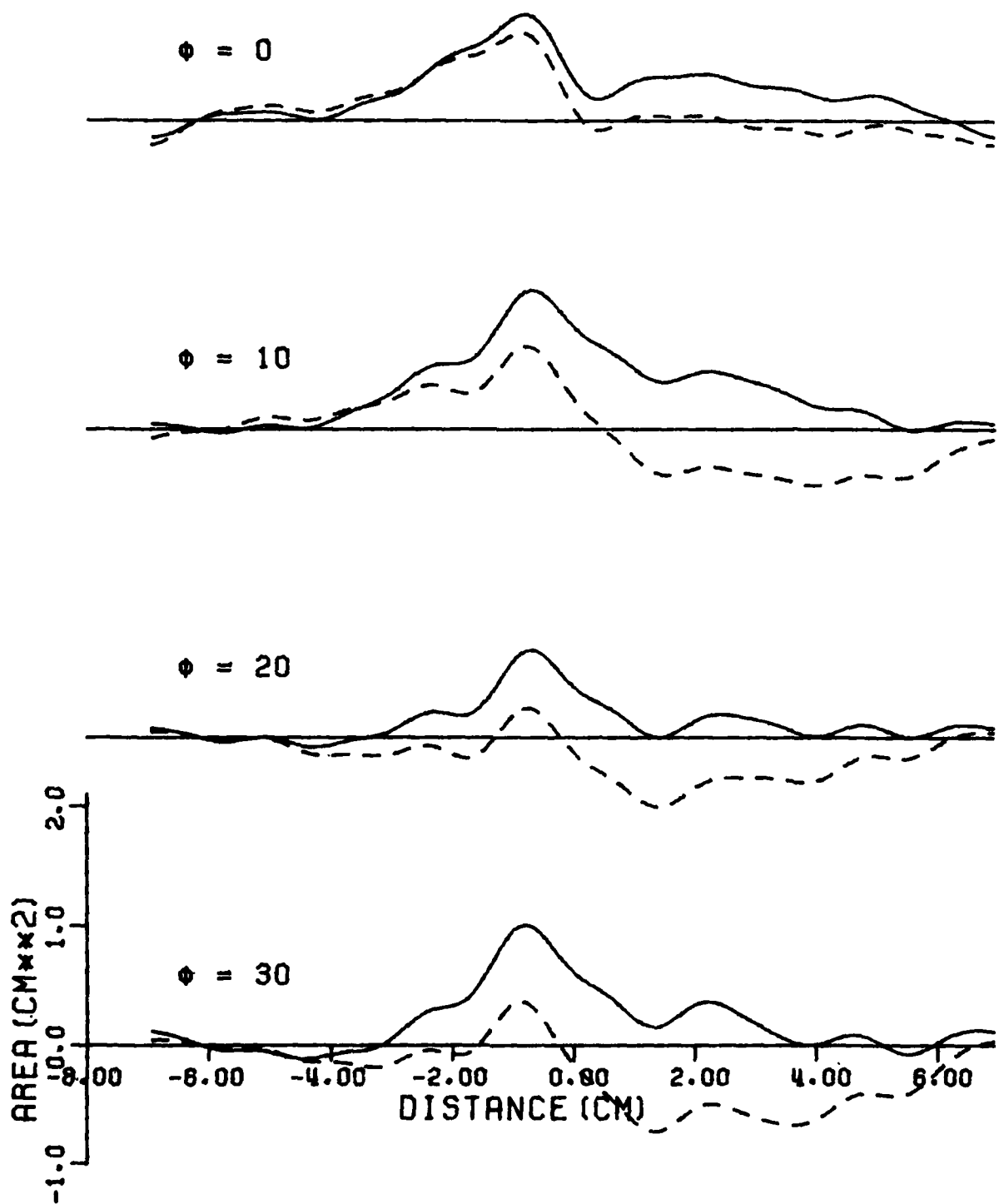


Figure B-7. Target 4 vertical polarization ramp responses.

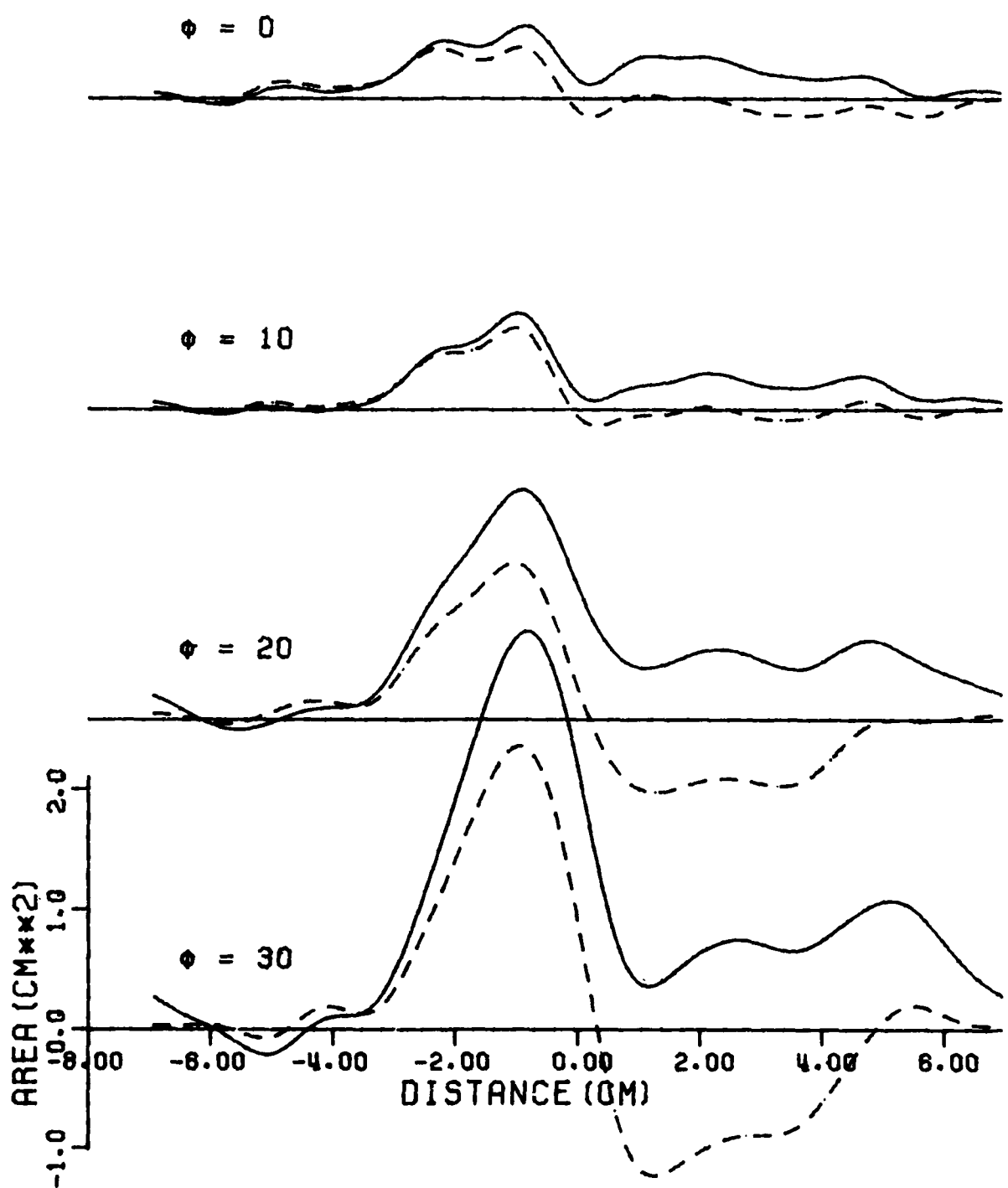


Figure B-8. Target 4 horizontal polarization ramp responses.

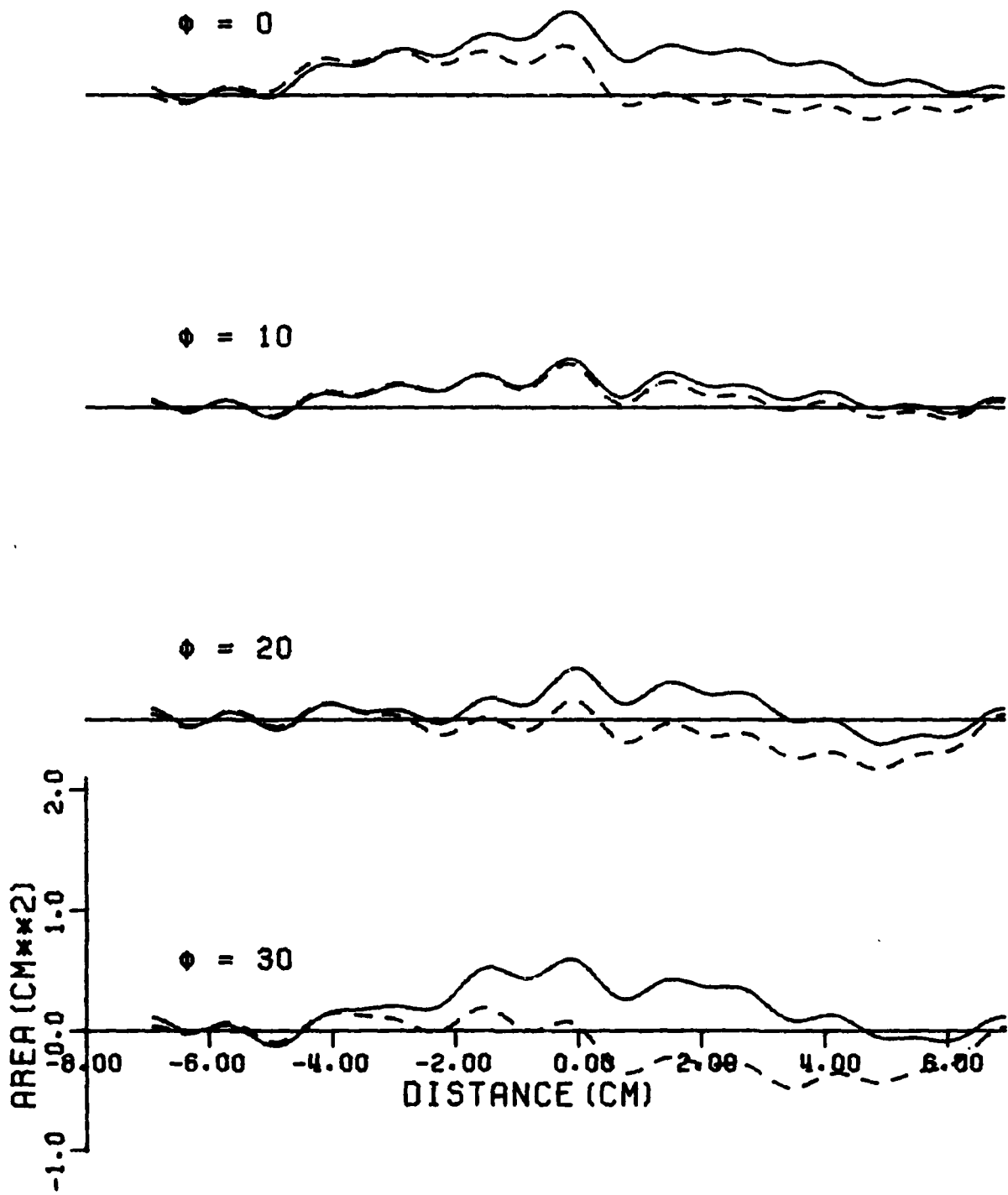


Figure B-9. Target 5 vertical polarization ramp responses.

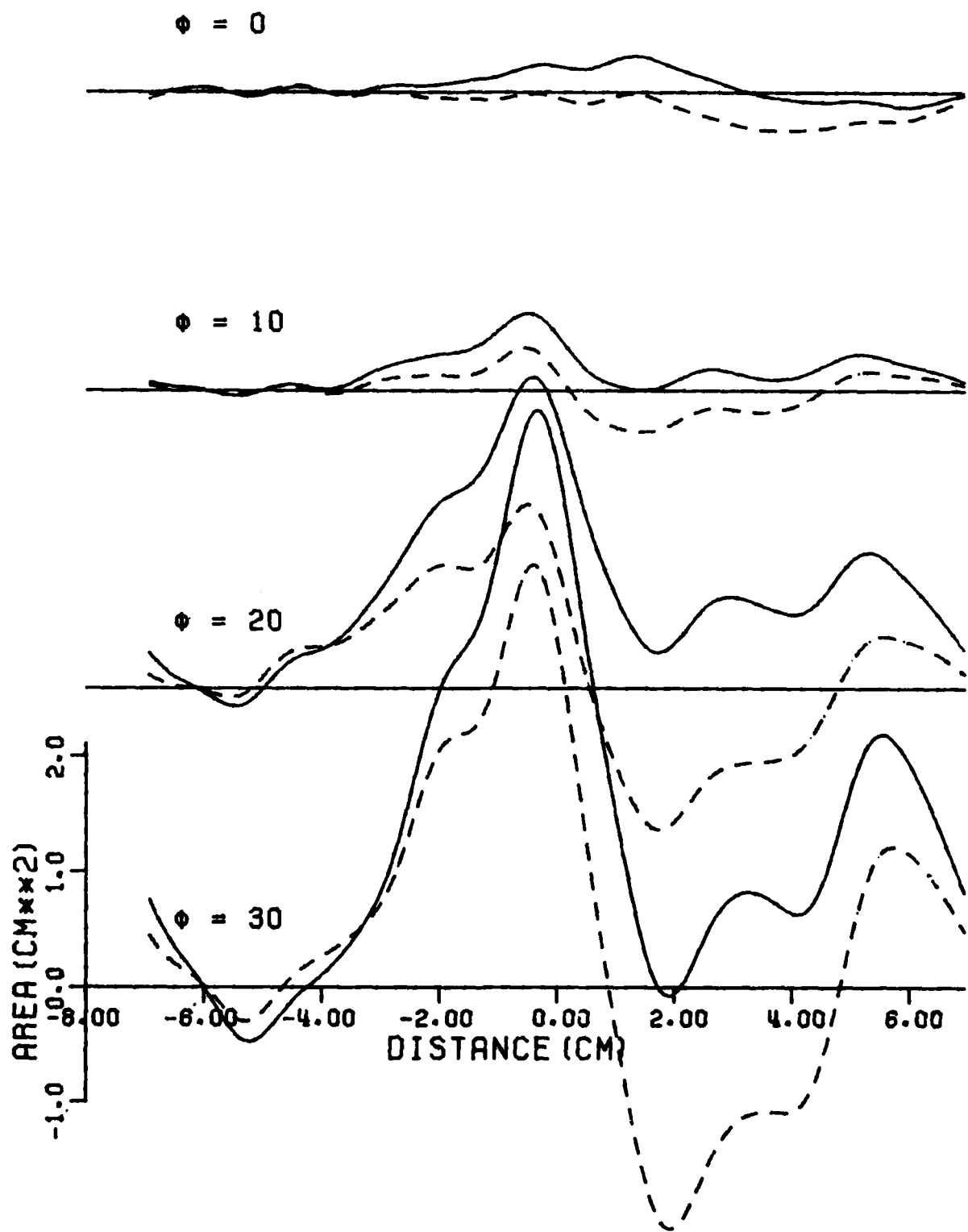


Figure B-10. Target 5 horizontal polarization ramp responses.

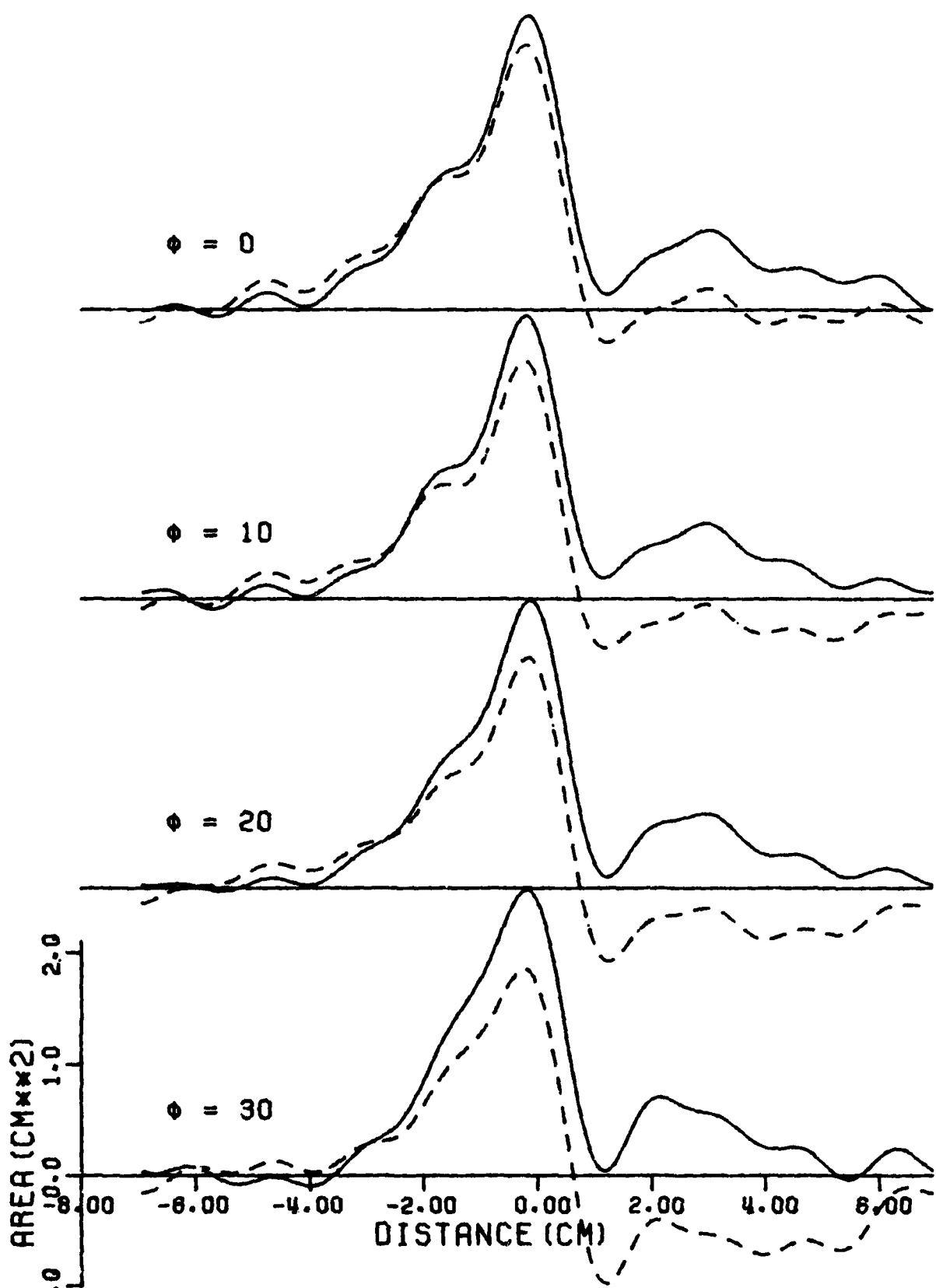


Figure B-11. Target 6 vertical polarization ramp responses.

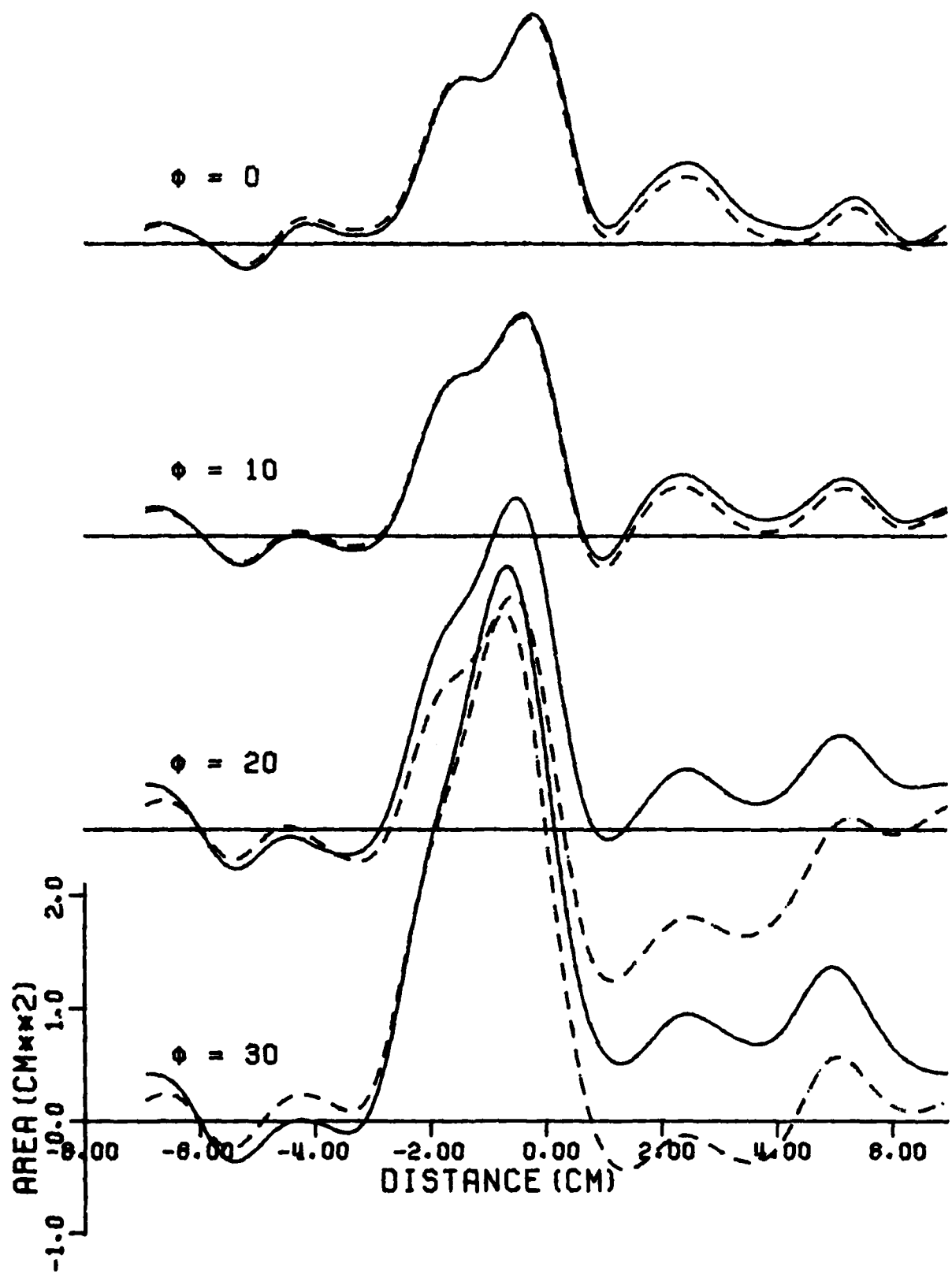


Figure B-12. Target 6 horizontal polarization ramp responses.  
123

